








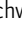


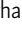
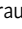





ARTICLE

# Regulation of adaptive growth decisions via phosphorylation of the TRAPP II complex in *Arabidopsis*

Christian Wiese<sup>1,2</sup> , Miriam Abele<sup>2,3</sup> , Benjamin Al<sup>2</sup> , Melina Altmann<sup>4</sup> , Alexander Steiner<sup>2</sup> , Nils Kalbfuß<sup>2</sup> , Alexander Strohmayer<sup>1,2</sup> , Raksha Ravikumar<sup>2</sup> , Chan Ho Park<sup>5</sup> , Barbara Brunschweiler<sup>2</sup> , Chen Meng<sup>3</sup> , Eva Facher<sup>6</sup> , David W. Ehrhardt<sup>5</sup> , Pascal Falter-Braun<sup>4</sup> , Zhi-Yong Wang<sup>5</sup> , Christina Ludwig<sup>3</sup> , and Farhah F. Assaad<sup>1,2</sup> 

Plants often adapt to adverse or stress conditions via differential growth. The trans-Golgi network (TGN) has been implicated in stress responses, but it is not clear in what capacity it mediates adaptive growth decisions. In this study, we assess the role of the TGN in stress responses by exploring the previously identified interactome of the Transport Protein Particle II (TRAPP II) complex required for TGN structure and function. We identified physical and genetic interactions between AtTRAPP II and shaggy-like kinases (GSK3/AtSKs) and provided *in vitro* and *in vivo* evidence that the TRAPP II phosphostatus mediates adaptive responses to abiotic cues. AtSKs are multifunctional kinases that integrate a broad range of signals. Similarly, the AtTRAPP II interactome is vast and considerably enriched in signaling components. An AtSK-TRAPP II interaction would integrate all levels of cellular organization and instruct the TGN, a central and highly discriminate cellular hub, as to how to mobilize and allocate resources to optimize growth and survival under limiting or adverse conditions.

## Introduction

Plant responses to environmental stimuli involve diverse forms of growth or movement. The slow, cyclic movement of shoots and stems helps climbing plants such as vines find supportive structures, and stem growth or tendrils are then used to wrap around and cling to such structures (Darwin, 1880). Leaf movements linked to the circadian rhythm enable plants to maximize their exposure to sunlight (McClung, 2006). Tropisms are additional examples of movement in plants: the shoot bends toward directional light, whereas the root bends away from the light. In addition to phototropism, plants have tropic responses to a range of stimuli including moisture, fluctuations in temperature, gravity, touch, and other mechanical cues (Garzón and Keijzer, 2011). Darwin argues that the movements of plants are driven by growth and the need to access resources, such as sunlight and water (Darwin, 1880). Gyration, revolution, and tropisms require some form of differential growth or bending at the organ level. Bending is achieved when one side of an organ grows more rapidly than the opposing side. This differential

growth is a result, at least in part, of the differential sorting of PIN-FORMED (PIN) auxin transporters, resulting in the unequal distribution of auxin, a morphogen, at opposing sides of a cell (Friml et al., 2002; Ding et al., 2011). It follows that differential growth responses such as bending require differential sorting decisions. How environmental stimuli are translated into sorting decisions remains largely unclear.

The sorting of PIN transporters has been shown to require trans-Golgi network (TGN) function. Indeed, disruption of TGN function by mutation results in the ectopic distribution of PIN or AUX proteins (Naramoto et al., 2014; Qi et al., 2011; Rybak et al., 2014; Ravikumar et al., 2018). The TGN plays a key role not only in the sorting of macromolecules but also in exocytosis and endocytosis. In addition, the TGN performs specialized functions such as cytokinesis, cell differentiation, the establishment of cell polarity, and anisotropic growth (Gendre et al., 2015; Ravikumar et al., 2017). As an early endosome, the plant TGN is a central hub in the flow of information to and from the plant cell surface

<sup>1</sup>Biotechnology of Natural Products, TUM School of Life Sciences, Technical University of Munich, Freising, Germany; <sup>2</sup>Botany, TUM School of Life Sciences, Technical University of Munich, Freising, Germany; <sup>3</sup>Bavarian Center for Biomolecular Mass Spectrometry (BayBioMS), TUM School of Life Sciences, Technical University of Munich, Freising, Germany; <sup>4</sup>Institute of Network Biology (INET), Molecular Targets and Therapeutics Center (MTTC), Helmholtz Center Munich, German Research Center for Environmental Health, Munich-Neuherberg, Germany; <sup>5</sup>Department of Plant Biology, Carnegie Institution for Science, Stanford, CA, USA; <sup>6</sup>Systematic Botany and Mycology, Faculty of Biology, Ludwig-Maximilians-Universität (LMU) München, Planegg-Martinsried, Germany.

Correspondence to Farhah F. Assaad: [farhah.assaad@tum.de](mailto:farhah.assaad@tum.de); Christian Wiese: [christian.wiese@tum.de](mailto:christian.wiese@tum.de).

© 2024 Wiese et al. This article is distributed under the terms of an Attribution-Noncommercial-Share Alike-No Mirror Sites license for the first six months after the publication date (see <http://www.rupress.org/terms/>). After six months it is available under a Creative Commons License (Attribution-Noncommercial-Share Alike 4.0 International license, as described at <https://creativecommons.org/licenses/by-nc-sa/4.0/>).

(Uemura, 2016). The plant TGN has been implicated in responses to abiotic stimuli such as drought, heat, salt stress and osmotic stress, and to biotic stimuli such as fungal attack (Rosquete and Drakakaki, 2018). Studies on the role of the TGN in stress responses have been carried out predominantly with core trafficking components required for membrane tethering, docking, and fusion (Rosquete and Drakakaki, 2018; Ravikumar et al., 2017). Trafficking mutants typically exhibit root growth defects and/or hypersensitivity to abiotic cues such as salt stress, osmotic stress, drought, or heat (Asaoka et al., 2013; Kim and Bassham, 2011; Lee et al., 2006; Rosquete et al., 2019; Uemura et al., 2012; Wang et al., 2011; Zhu et al., 2002). However, whether trafficking mutants have primary defects in growth with secondary consequences in stress responses or whether the primary defects lie in an impaired response to stress factors remains unclear. More broadly, in the context of stress responses, the question pertains as to whether the TGN is involved in decision-making processes per se or merely in the execution of adaptive growth decisions.

As regards decision-making processes, there is a growing body of evidence to suggest that plants have the ability to learn, process information, communicate, reach decisions, and in general exhibit behavior that could be considered cognitive (reviewed in Severino, 2021). Severino (2021) makes the case for experimental approaches to study the decisions plants make in complex environments. A recent experimental approach for the study of decision-making processes in germinating seedlings has incorporated two tools used in decision theory: the use of a limited budget and conflict-of-interest scenarios (Kalbfuß et al., 2022). A limited budget was achieved by germination in the dark in the absence of a carbon source, such that the only available energy source is that available in the seed (Kalbfuß et al., 2022). A conflict-of-interest scenario comprises the simultaneous withdrawal of light, which promotes hypocotyl elongation, and water, which promotes root elongation (Kalbfuß et al., 2022). As the severity of water stress increased, root length increased while hypocotyl length decreased; importantly, the total seedling length remained constant (Kalbfuß et al., 2022). Thus, trade-offs in hypocotyl versus root growth were observed and these comprise a binary readout for responses to these additive stress conditions. Decision mutants were defined as mutants that were either incapable of adjusting their hypocotyl/root ratios in response to additive stress, or that consistently reached the wrong growth decisions as compared to the wild type (Kalbfuß et al., 2022). By emphasizing growth trade-offs, the experimental approach developed by Kalbfuß et al. (2022) is aligned with the definition of decision-making as entailing an appraisal of the advantages and disadvantages of various courses of action (Karban and Orrock, 2018). While Kalbfuß et al. (2022) address decision-making at a cellular level, the literature on plant decision-making has, to our knowledge, not included considerations about the possible role of the TGN.

To understand the role of the TGN in adaptive or stress responses, it would be important to deploy a battery of gene products not only broadly associated with or localized to the TGN but also intrinsic to TGN structure and function. Two such proteins or complexes are ECHIDNA and the Transport Protein

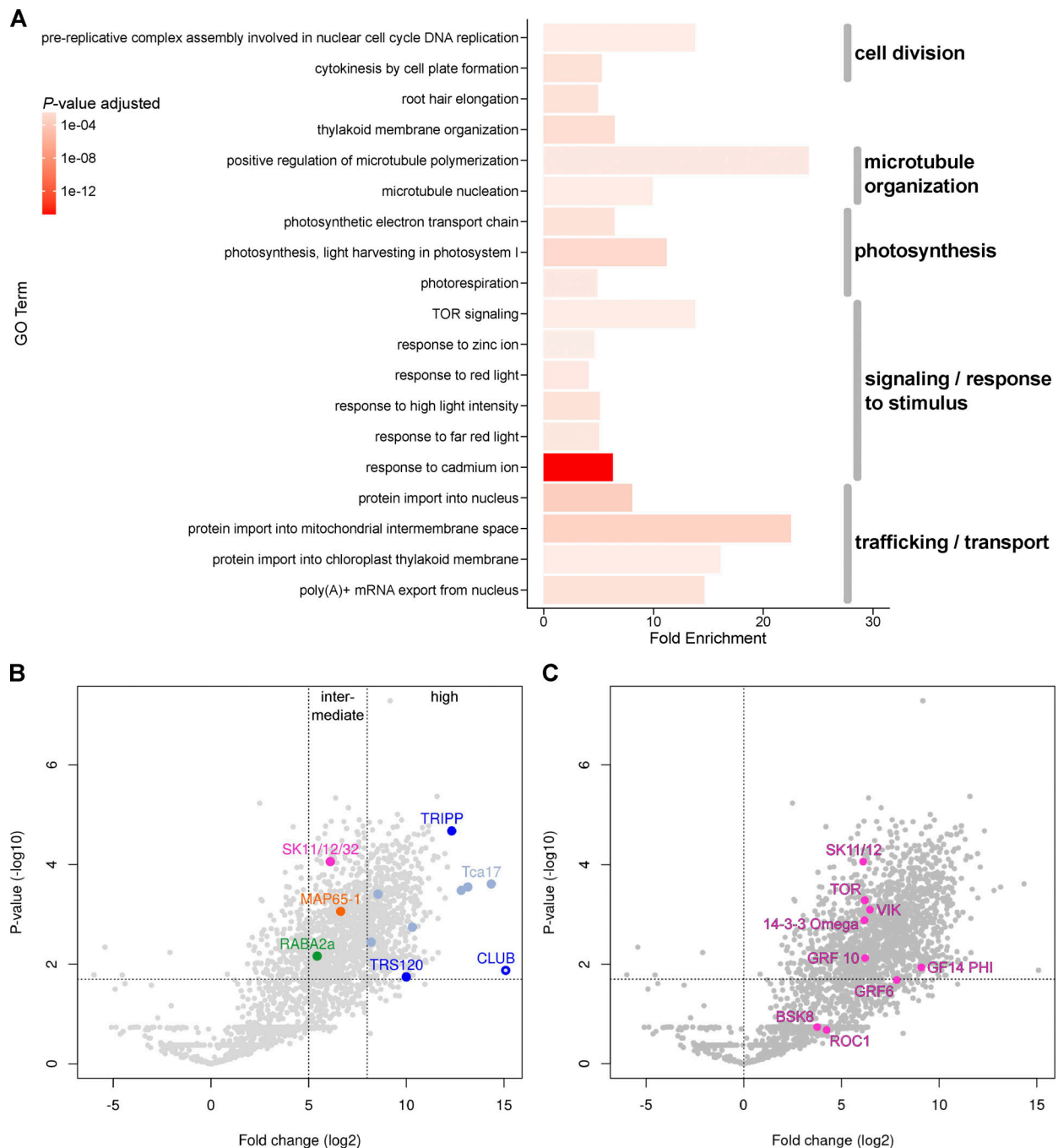
Particle II (TRAPP II) complex. ECHIDNA was identified as an upregulated transcript in elongating cells (Gendre et al., 2011). Yeast and metazoan TRAPP II is a hetero-oligomeric complex that acts as a guanine nucleotide exchange factor (GEF) for Rab GTPases, converting GDP-bound inactive Rab GTPases to active GTP-bound forms (Cai et al., 2005; Morozova et al., 2006; Pinar et al., 2015; Thomas and Fromme, 2016; Riedel et al., 2018). TRAPP II has been shown to play a key role in the regulation of the TGN in all eukaryotes, but our understanding of its potential physiological roles is incomplete (Pinar and Peñalva, 2020). The *Arabidopsis* TRAPP II (AtTRAPP II) complex was identified by mutation in screens for seedlings with aberrant morphogenesis or cytokinesis defects (Söllner et al., 2002; Thellmann et al., 2010; Jaber et al., 2010). AtTRAPP II consists of seven shared core subunits and three TRAPP II-specific subunits (AtTRS120/TRAPPC9, CLUB/AtTRS130/TRAPPC10, and the plant-specific TRIPP) and most resembles fungal and metazoan TRAPP II complexes (Garcia et al., 2020; Kalde et al., 2019; Pinar et al., 2019). We have previously shown that ECHIDNA and TRAPP II have overlapping yet distinct functions at the TGN in *Arabidopsis* (Ravikumar et al., 2018). ECHIDNA is primarily required for the genesis of secretory vesicles and, as a consequence, for cell expansion (Boutté et al., 2013; Gendre et al., 2013; McFarlane et al., 2013). AtTRAPP II plays a role not only in basal TGN functions—exocytosis, endocytosis, and protein sorting—but also in more specialized TGN functions such as cytokinesis and the establishment of cell polarity (Ravikumar et al., 2018). Whether or not AtTRAPP II plays a role in responses to abiotic cues such as osmotic or drought stress remains to be determined.

In this study, we focus on the TRAPP II complex as a starting point as it is required for all aspects of TGN function, including the sorting of proteins such as PINs to distinct membrane domains (Qi et al., 2011; Rybak et al., 2014; Ravikumar et al., 2018). We first explored the *Arabidopsis* TRAPP II interactome and also surveyed dynamic or conditional interactions. Together with yeast two-hybrid screens, this identified shaggy-like kinases such as AtSK21/BIN2 as TRAPP II interactors. We corroborated this finding with in vitro kinase assays and pharmacological inhibition in vivo. Shaggy-like kinases are multitaskers that integrate a vast number of biotic and abiotic cues (Lv and Li, 2020; Planas-Riverola et al., 2019; Youn and Kim, 2015; Li et al., 2021; Song et al., 2023). AtSK21/BIN2 has recently been implicated in decision-making in *Arabidopsis* seedlings (Kalbfuß et al., 2022). We explore the meaning of the AtSK-TRAPP II interaction using a variety of assays to monitor stress responses and differential growth decisions.

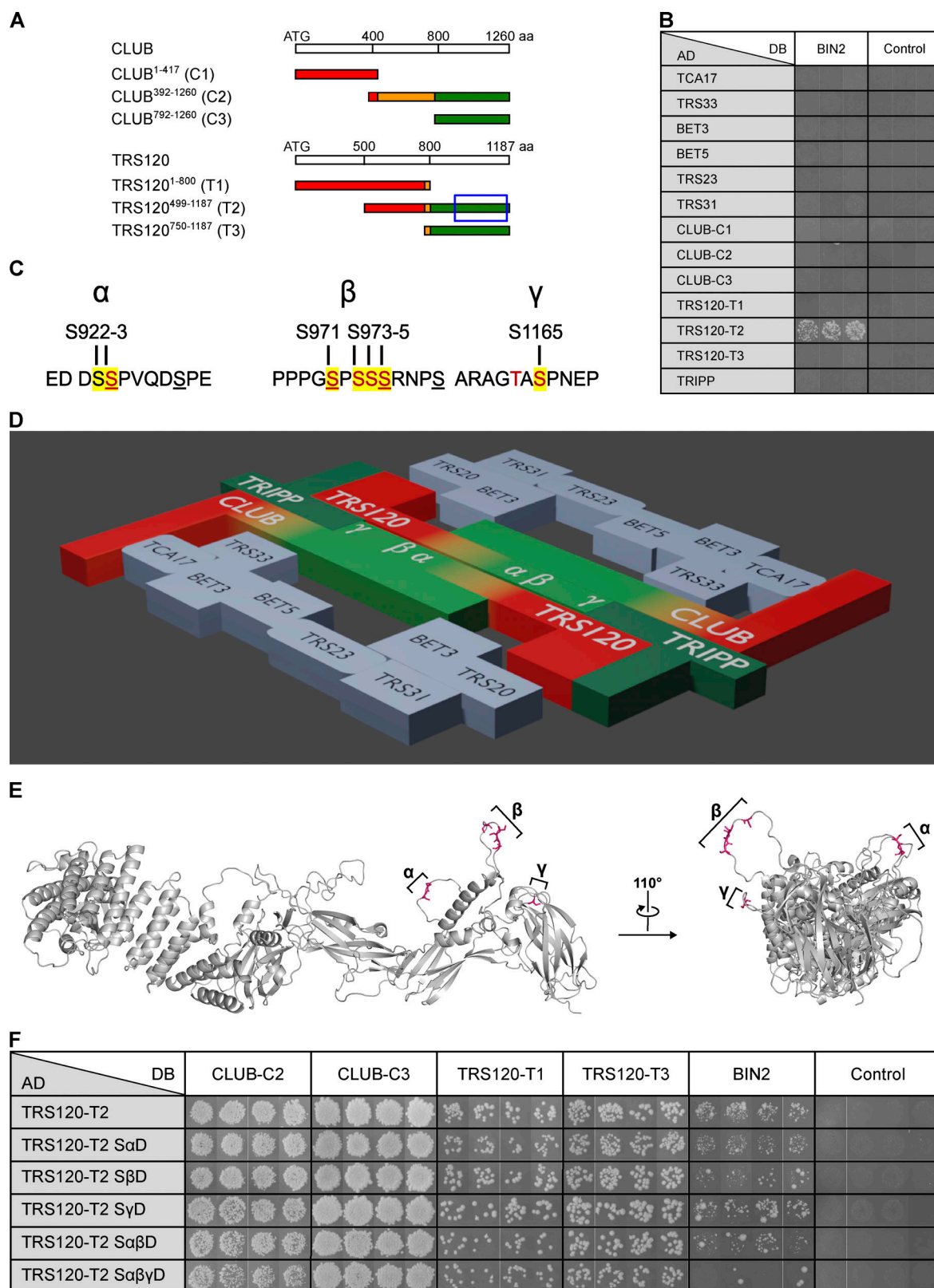
## Results

### The TRAPP II interactome contains a large number of signaling components

To gain insight into TGN function, we used the TRAPP II interactome as a starting point. We have previously identified TRAPP and EXOCYST subunits, cytoskeletal proteins, and Rab GTPases in the TRAPP II interactome (Rybak et al., 2014; Steiner et al., 2016; Kalde et al., 2019; Garcia et al., 2020). However, no global



**Figure 1. The TRAPP II interactome.** The data are derived from an analysis of IP-MS from inflorescences with the TRAPP II-specific subunit CLUB:GFP as bait (see Fig. 1 B; Kalde et al., 2019). Each protein was present in all three biological replicates. The soluble GFP empty vector was used as a negative control. **(A)** Gene ontology (GO) term enrichment analysis of the TRAPP II interactome. Depicted are highly enriched (fold enrichment  $\geq 4$ ) and significant (FDR-adjusted P value  $\leq 0.003$ ) GO term associations of biological processes of level 0 as bar plots. The length of each bar depicts the fold enrichment of GO terms associated with detected proteins, while the color intensity indicates the significance given as the P value adjusted for the false discovery rate (FDR). Interactors of intermediate intensity ( $>5$  and  $<8$ ) were used (see Fig. S1 A for an analysis of high-confidence interactors). In addition to the expected ontologies describing traffic, transport, cell division, and microtubule organization, significantly enriched GO categories describe responses to stimuli such as light and metal ions. **(B and C)** Volcano plots are presented. On the X axis: The ratio (or fold change) was calculated for each protein as the average intensity of the signal in the experiment divided by its average intensity in the control. On the Y axis the P values of the signal in the experiment versus the control, depicted along a negative log10 scale, are shown. Dotted gray lines represent cutoffs: P value  $\leq 0.02$  in B and C and ratio  $>8$  for high fold change or  $>5$  for intermediate fold change in B. **(B)** Note that TRAPP II subunits (light blue for core TRAPP; dark blue for TRAPP II-specific subunits; the CLUB/AtTRS130:GFP TRAPP II-specific bait is depicted as an open circle) are in the upper right field, indicating high abundance and good reproducibility. AtSKs (magenta), MAP65-1 (orange) and RAB-A2a GTPase (green) are all in the upper middle field; these may be transient interactors of TRAPP II. Note that AtSKs (AtSK11/12/32) are more significant than validated interactors such as MAP65 and RAB-A2a (Kalde et al., 2019; Steiner et al., 2016). **(C)** Highlighted in magenta are members of the brassinosteroid signaling pathway that were differentially enriched over light- versus dark-grown seedlings in a different IP-MS experiment. Note that BSK8, and ROC1 did not meet the significance cutoffs. The most significant interactors were GSK3/AtSK shaggy-like kinases and TOR. Related to Fig. S1 and Table S1.



**Figure 2. GSK3/AtSK sites in TRAPPII and binary interactions.** Yeast two-hybrid assays were carried out by pairwise one-on-one mating in four independent replicate experiments, of which three (B) or four (F) are shown. As a negative control, the respective AD constructs were tested with the empty DB vector. The panels are from different plates (in B, F). (A) TRAPPII-specific truncations for yeast two-hybrid were based on phylogenetic analysis (Steiner et al., 2016). Conserved sequences are depicted in red, intermediate degrees of conservation in orange, and plant-specific sequences are in green. All three GSK3 sites found to be phosphorylated in vivo reside in the plant-specific moiety of TRS120-T2 (green; a blue rectangle delineates the region of interest). (B) Yeast two-hybrid assays of interactions between BIN2 and TRAPPII subunits. BIN2 was fused to the GAL4 DNA-binding domain (DB) and TRAPPII subunits and truncations



thereof (CLUB-C1, -C2, -C3 and TRS120-T1, -T2, -T3) to the GAL4 activation domain (AD). The results show interactions between BIN2 and AtTRS120-T2 wild type. BIN2 bound specifically to the TRAPP11 subunit TRS120 and not with other TRAPP11 subunits or truncations. In a total of >2,400 pairwise tests, BIN2 was the only kinase we found that interacted with a TRAPP subunit. The Y2H did not detect CLUB/AtTRS130-AtSK interaction shown in Fig. 1 B, which shows copurified proteins that can include indirect—as opposed to binary—interactors. (C) GSK3 sites in AtTRS120-T2. The  $\alpha$ -phosphosite of AtTRS120 spans amino acid positions S922 and S923, the  $\beta$ -phosphosite amino acids S971-S975 and the  $\gamma$ -phosphosite amino acid residue S1165. The canonical GSK3 consensus sequence is: (pS/pT)XXX(S/T), and the  $\beta$ -phosphosite fits this definition (see underlined SXXXS). Even though they are annotated as GSK3 sites in the PPSP (<https://www.phosphosite.org>) database, the  $\alpha$ -phosphosite deviates somewhat with SXXXS, and the  $\gamma$ -phosphosite deviates completely. Amino acids in red were mutated to A or D via site-directed mutagenesis. Amino acids highlighted in yellow were found to be phosphorylated in vivo (see Fig. S2) and these were all serines. (D) The *Arabidopsis* TRAPP11 complex consists of seven shared core subunits (TCA17, TRS33, BET3, BET5, TRS23, TRS31, TRS20; light blue) and three TRAPP11-specific subunits (CLUB/AtTRS130, AtTRS120, and the plant-specific subunit TRIPP), and forms a dimer with plant-specific domains (green) at the predicted dimer interface (Kalde et al., 2019; Garcia et al., 2020). This model is based on extensive pair-wise yeast two-hybrid analysis between TRAPP11 subunits in *Arabidopsis* (Kalde et al., 2019; Garcia et al., 2020). (E) Mapping of GSK3/AtSK sites on an AlphaFold structural prediction (Jumper et al., 2021; Varadi et al., 2022) of AtTRS120. A lateral view and a frontal perspective are shown. Note that all three GSK3/AtSK sites (magenta sticks) reside in unstructured, flexible, and accessible regions of the protein. (F) Interactions between BIN2 and TRAPP11 complex subunits (CLUB-C2, CLUB-C3, TRS120-T1, TRS120-T3 truncations), as positive controls, fused to the GAL4 DNA-binding domain (DB) and TRS120-T2 truncation and its phosphomutants TRS120-T2 S $\alpha$ D, S $\beta$ D, S $\gamma$ D, S $\alpha$  $\beta$ D, and S $\alpha$  $\beta$  $\gamma$ D fused to the GAL4 activation domain (AD). Note the positive interactions between BIN2 and AtTRS120-T2 wild type and phosphovariants; there was, however, no reproducible interaction if all three target sites were phosphomimetic (TRS120-T2 S $\alpha$  $\beta$  $\gamma$ D). Related to Figs. S2, S3, and S4.

meta-analysis of the vast *Arabidopsis* TRAPP11 interactome has been carried out to date. We, therefore, performed a gene ontology (GO) term enrichment analysis. We focused on the TRAPP11-specific CLUB:GFP interactome. This interactome was significantly enriched in proteins involved in cell division, trafficking or transport, root hair elongation, and microtubule organization, which is consistent with known *trapp11* phenotypes (Fig. 1 A and Fig. S1 A; Jaber et al., 2010; Qi et al., 2011; Rybak et al., 2014; Ravikumar et al., 2018; Söllner et al., 2002; Thellmann et al., 2010; Steiner et al., 2016). Interestingly, a large number of enriched GO terms were implicated in signaling (Fig. 1 A and Fig. S1 A), suggesting that AtTRAPP11 may act as a cellular hub.

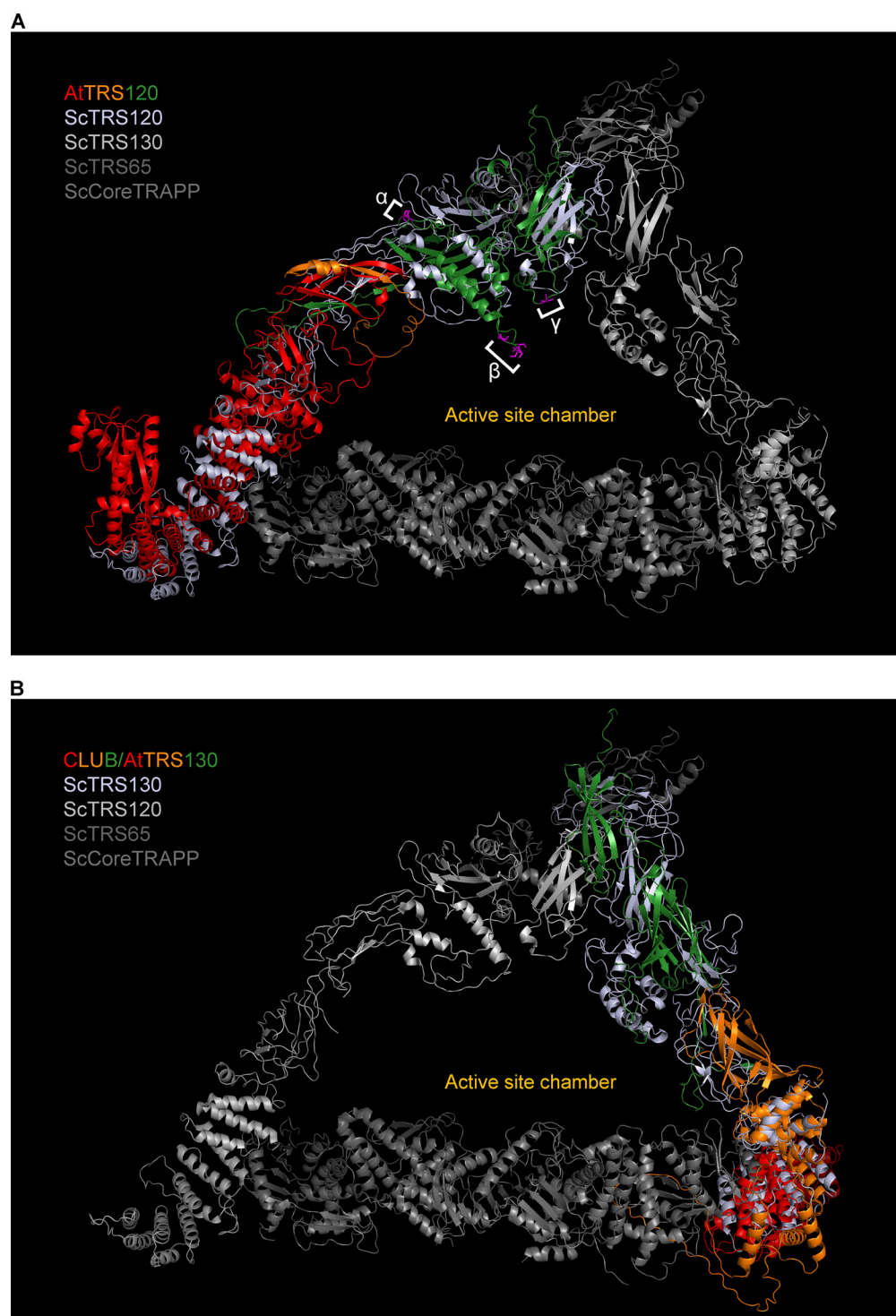
To further explore a possible implication of the TRAPP11 complex in signaling, we surveyed the dynamic interactome, by which we refer to interactors perceived under one environmental condition (for example in the light) but not in another (for example in the dark). By these criteria, brassinosteroid (BR) signaling components were significantly enriched ( $P = 0.016$ ); this category encompasses 11 proteins, of which 9 were detected in CLUB:GFP immunoprecipitates from light-grown inflorescences (Fig. 1, B and C; and Fig. S1 B and Table S1). Among these were the TOR kinase and a family of shaggy-like kinases (AtSKs; Fig. 1 C and Fig. S1 B; and Table S1). TOR signaling was also a significantly enriched GO term in the TRAPP11 interactome (Fig. 1 A). TOR and AtSKs are highly significant interactors in the TRAPP11-specific subunit CLUB:GFP interactome (Fig. 1, B and C; and Fig. S1 B). They show a fold change that is lower than that seen for components of the TRAPP11 complex, but similar to that seen for validated interactors such as RAB-A2a and MAP65, expected to form more transient associations (Fig. 1, B and C; Kalde et al., 2019; Steiner et al., 2016). We then used yeast two-hybrid (Y2H) to probe for binary interactions between TRAPP11 and signaling components identified in the IP-MS. Y2H was carried out with TRAPP11 subunits and truncations thereof (Fig. 2 A; Kalde et al., 2019; Steiner et al., 2016; Garcia et al., 2020). In a large-scale Y2H screen including 2,400 pairwise tests, an interaction was detected between a TRS120<sup>499-1187</sup> truncation (TRS120-T2) and the shaggy-like kinase BIN2 (AtSK21; Fig. 2 B). BIN2 interacted specifically with AtTRS120

and not with other tested TRAPP11 subunits (Fig. 2 B). Furthermore, we did not detect any other TRAPP11-kinase interactions in our pairwise Y2H assays. In conclusion, mass spectrometry and Y2H identify physical interactions between TRAPP11 and AtSKs, in planta and in a heterologous system.

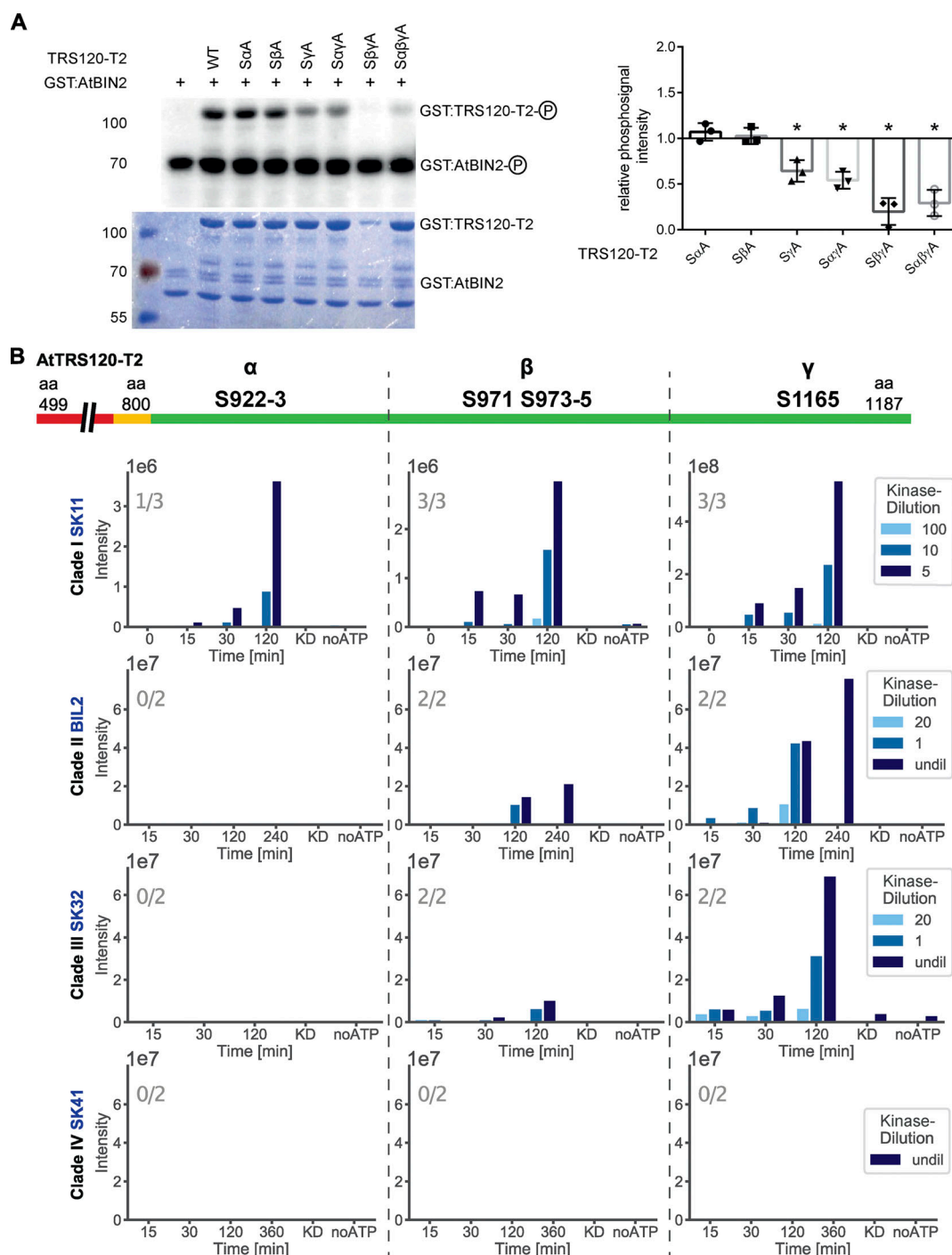
### The TRAPP11 complex is a target of shaggy-like kinases

To assess whether the TRAPP11 complex is a target of AtSK/GSK3 kinases, we first looked for the presence of phosphopeptides in AtTRS120 and CLUB/AtTRS130 coimmunoprecipitates via mass spectrometry. This provided ample in vivo evidence for TRAPP11 AtTRS120 phosphorylation at AtSK/GSK3 sites (Fig. S2). Furthermore, shaggy-like kinases were detected in IP-MS not only with the TRAPP11-specific subunit CLUB/AtTRS130 (Fig. 1, B and C; and Fig. S1 B) but also with the TRAPP11-specific subunit AtTRS120 (Fig. S3). The *Arabidopsis* genome encodes ten shaggy-like kinases (AtSKs), which are classified into four clades (Fig. S3 A). Razor peptides covering all four clades were found in the AtTRS120:GFP interactome (Fig. S3, B–D).

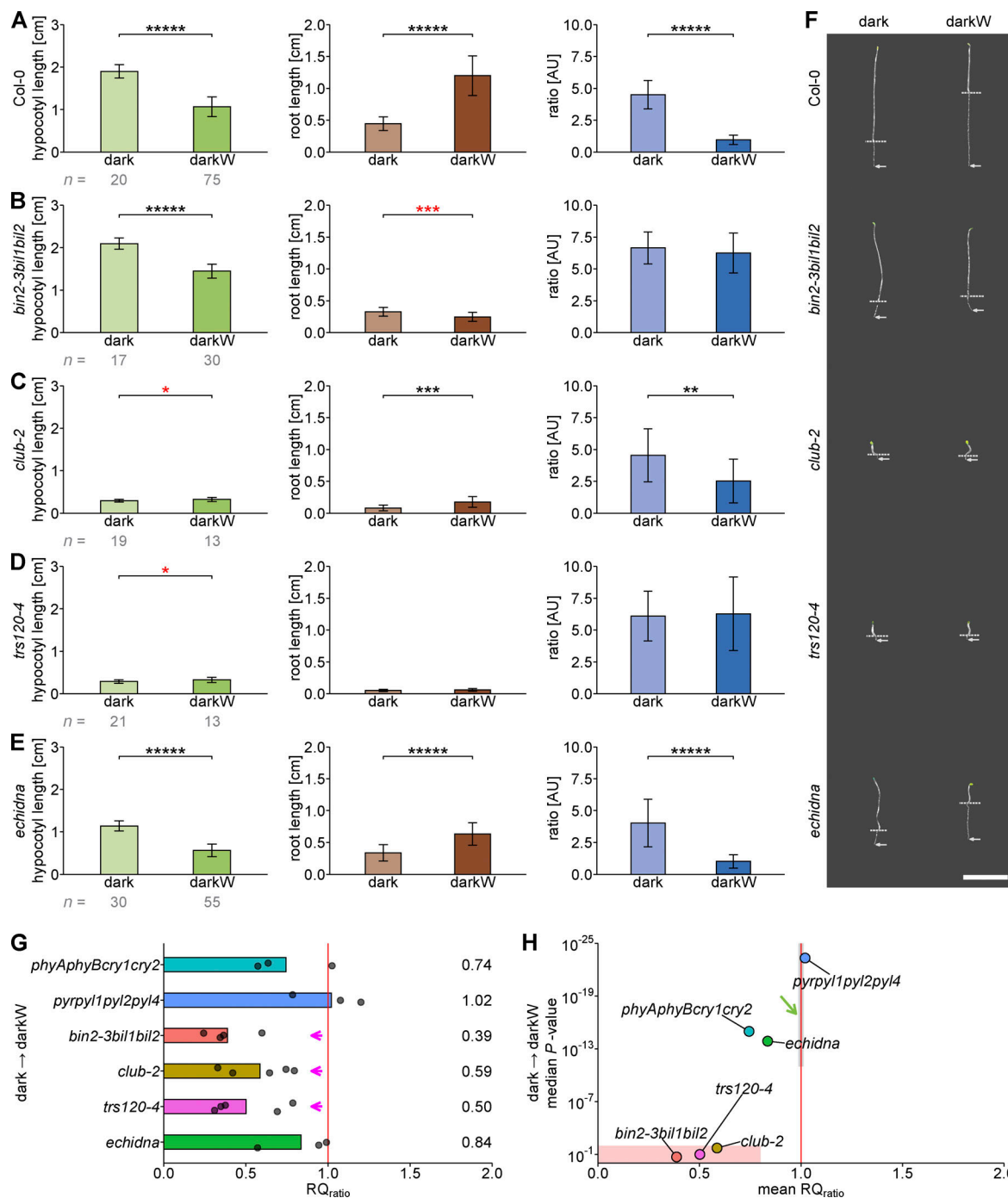
The TRS120-T2 truncation contains the GSK3 sites we had found to be phosphorylated in vivo (Fig. S2; see yellow highlights in Fig. 2 C). Our nomenclature for these sites is  $\alpha$ ,  $\beta$ , and  $\gamma$ , which is short for TRS120-S922:S923 ( $\alpha$ ), TRS120-S971:S973:S974:S975 ( $\beta$ ), and TRS120-S1165 ( $\gamma$ ; Fig. 2 C). These reside in the plant-specific moiety of AtTRS120 and are embedded in plant-specific sequences (see green shading in Fig. 2 A and Fig. 2 D) at the dimer interface (Kalde et al., 2019). AlphaFold structural predictions (Varadi et al., 2022; Jumper et al., 2021) show that the three sites reside in unstructured, flexible, and accessible regions of the AtTRS120 protein, as is observed in the majority of modified amino acid residues (Fig. 2 E and S4 A; Jiménez et al., 2007). Furthermore, a cross-kingdom structural alignment of AtTRS120 and CLUB/AtTRS130 with cryo-EM-generated structures of yeast TRAPP11 (Mi et al., 2022) showed that the  $\beta$  and  $\gamma$  phosphorylation sites face the active site chamber or Rab GTPase binding pocket predicted by Mi et al. (2022) and Bagde and Fromme (2022) (Fig. 3, Fig. S4, and Video 1). To study the three sites, we generated site-directed mutations in TRS120-T2, mutating the serine (S) and threonine (T) residues (depicted in red in Fig. 2 C) to non-phosphorylatable alanine (A) residues, or



**Figure 3. Cross-kingdom structural alignment of TRAPP II-specific subunits. (A and B)** AlphaFold predictions (Jumper et al., 2021; Varadi et al., 2022) of *Arabidopsis thaliana* (At) (A) AtTRS120 and (B) CLUB/AtTRS130 aligned with the open formation of the TRAPP II monomer structure without substrate in *Saccharomyces cerevisiae* (Sc) resolved with cryo-electron microscopy (in vitro) from Mi et al. (2022). *Arabidopsis* subunits were mapped onto the ScTRAPP II structure with the align algorithm in PyMOL. Reported root-mean-square deviations (RMSD) were 16.966 Å (3,775 atoms) for AtTRS120/TRAPPC9 and 12.953 Å (1,660 atoms) for CLUB/AtTRS130/TRAPPC10. The ScTRAPP II monomer is depicted in different shades of gray and only the respective Sc subunit where the *Arabidopsis* subunits aligned with is highlighted in blue-white (ScTRS120 in A and ScTRS130 in B). AtTRS120 and CLUB/AtTRS130 are colored based on their sequence conservation (red: conserved sequences; orange: intermediate conservation; green: plant-specific sequences—as depicted in Fig. 2, A and D). Both *Arabidopsis* protein structures aligned with their respective yeast subunit. Despite their small protein length differences ScTRS120 (1,289 aa) and AtTRS120 (1,186 aa) share conserved sequences (Cox et al., 2007) and mapped onto each other in the cross-kingdom structural alignment. Note that the  $\beta$  and  $\gamma$  phosphorylation sites of AtTRS120 (magenta sticks) face inwards, toward the active site chamber (including the RAB11/Rab-A GTPase binding pocket) proposed by Mi et al. (2022) and Bagde and Fromme (2022). Related to Fig. S4 and Video 1.



**Figure 4. In vitro AtSK kinase assays with TRS120 as bait. (A)** In vitro kinase assays using GST:AtBIN2 (69 kDa) and GST:TRS120-T2 (100 kDa). The change of phosphosignal is shown in a representative autoradiograph (upper panel) and the loaded protein amount in the corresponding CBB (Coomassie stain, lower panel). Non-phosphorylatable S to A TRS120-T2 variants were used as negative controls. The means  $\pm$  SD of phosphosignals were normalized to the protein amount and related to non-mutated TRS120-T2 wild-type control. Note that BIN2 phosphorylated AtTRS120-T2 in vitro, with a preference for wild-type (WT) sequences over non-phosphorylatable AtTRS120-S $\alpha$ A, AtTRS120-S $\alpha$ YA, AtTRS120-S $\beta$ YA and AtTRS120-S $\alpha$  $\beta$ YA substrates.  $n = 3$  independent experiments; \*:  $P < 0.05$  for significant differences to TRS120-T2 WT (set at 1.0 right panel) determined by using a one sample two-tailed  $t$  test. **(B)** Kinase assays were performed in vitro with mass-spectrometry readout. One member of each shaggy-like kinase clade (AtSKs; see Fig. S3 A) was used with a constant concentration of the TRS120-T2 truncation as substrate. The dilution series of the kinase are depicted in different shades of blue. AtTRS120-T2 has highly (red) and moderately (orange) conserved sequences, as well as plant-specific sequences (green). Three GSK3 sites (referred to as  $\alpha$ ,  $\beta$ ,  $\gamma$ ; see Fig. 2 C) can be found in the plant-specific T2 domain. AtSKs in clades I-III differentially phosphorylated the substrate at three GSK3 consensus sites (with a preference for the  $\gamma$  site) in a time-dependent and concentration-dependent manner. A clade IV AtSK did not phosphorylate at all. Samples incubated for 120 min in a kinase buffer without ATP, or samples in which the kinase was heat-inactivated (KD), served as negative controls. The numbers in grey in each plot denote the number of times the phosphorylation event was seen in the given number of independent replicates. Note the higher intensity of the TRS120-S $\gamma$  peptide, especially for Clade I/SK11 (1e8 for TRS120- $\gamma$  versus 1e6 for TRS120- $\alpha$  and TRS120- $\beta$  on the Y axis). Related to Figs. S2, S3, and S5. Source data are available for this figure: SourceData F4.



**Figure 5. Role of the TRAPP II complex versus ECHIDNA in hypocotyl/root trade-offs.** Seedlings were germinated on ½ MS in the dark (dark) or in the dark with  $-0.4$  MPa water stress (darkW). **(A)** Col-0 (wild type). **(B)** BR signaling mutant *bin2-3bil1bil2* triple knockout (from Kalbfuß et al., 2022). **(C)** *club-2*, a null *trappii* mutant. **(D)** *trs120-4*, a null *trappii* allele. **(E)** Null *echidna* allele, impaired in TGN structure and function. At least three experiments were performed for each line, and a representative one is shown here based on RQ and P values. **(F)** Representative seedling images of Col-0 (wild type) and mutants shown in A–E. *bin2-3bil1bil2* and *trs120-4* mutants failed to correctly adjust their hypocotyl and root lengths from dark to darkW conditions. Dotted lines mark the hypocotyl–root junction, whereas arrows point to the end of the root. Scale bar is 1 cm. **(G)** Normalized response quotient  $RQ_{ratio}$ . Each replicate is represented by a dot. A value of 1 (vertical red line) corresponds to an identical adaptation to darkW conditions as the wild type. Note that the triple *bin2-3bil1bil2* knock out, *trs120-4* and *club-2* had attenuated responses (magenta arrows). **(H)** Volcano plot with the mean  $RQ_{ratio}$  depicted on the X axis and the median P value of the response on the Y axis (negative log scale; a median of all replicates was used). The area shaded in gray on the red line (green arrow) is where wild-type ecotypes would theoretically map onto the plot. Mutants in the lower left quadrant (peach shading) were considered to have a “confused decision phenotype” (see text). *trs120-4* mutants mapped to the lower left quadrant and qualified as decision mutants on two counts: (i) a consistently opposite hypocotyl response (red asterisk in D), (ii) failure to adjust the hypocotyl/root ratio to darkW (the ratio for darkW is the same as for dark in D), translating into a non-significant P value for the ratio response (H). The number (n) of seedlings measured per condition is in gray below the mean  $\pm$  SD bar graphs. P values were computed with a two-tailed Student’s t test and are represented as follows: \* :  $P < 0.05$ ; \*\* :  $P < 0.01$ ; \*\*\* :  $P < 0.001$ ; \*\*\*\* :  $P < 0.0001$ ; \*\*\*\*\* :  $P < 0.00001$ . Mutant alleles and the corresponding ecotypes are described in Table S2. All data points for A–E are shown in Fig. S7. Related to Figs. S7 and S8.



to aspartate (D) to mimic constitutive phosphorylation. In the case of the TRS120-S $\beta$  site, for example, we designate these variants as TRS120-S $\beta$ A or TRS120-S $\beta$ D (Fig. 2 F and Fig. 4 A). The point mutations were introduced into cDNA sequences for expression in yeast and bacteria. In Y2H screens, the BIN2-TRS120 interaction, but not TRAPP1 complex interactions, was almost abolished when all three sites were phosphomimetic (TRS120-T2 S $\alpha$  $\beta$  $\gamma$ D; Fig. 2 F). As kinases typically have kiss-and-run interactions with their unphosphorylated substrates, and as BIN2 interacts more strongly with an unphosphorylated than a phosphorylated substrate (Pusch et al., 2012; Tang et al., 2011), this is consistent with AtTRS120/TRAPP9 being targeted by the BIN2 kinase.

The IP-MS and Y2H interactions were validated with in vitro kinase assays, performed with a phosphorus radioisotope (Fig. 4 A and Fig. S5 A). This showed that BIN2 and AtSK11 phosphorylated AtTRS120-T2 in vitro, with a preference for wild-type sequences over non-phosphorylatable substrates such as AtTRS120-S $\alpha$  $\beta$  $\gamma$ A (Fig. 4 A and Fig. S5 A). Further, the phosphorylation was confirmed with mass-spectrometry using non-radioactive assays. The mass-spectrometry results showed that the AtTRS120  $\alpha$ ,  $\beta$ , and  $\gamma$  sites phosphorylated in vivo (Fig. S2; IP-MS on seedlings using TRS120:GFP as bait) were phosphorylated by AtSKs in vitro (Fig. 4 B and Fig. S5 B). Kinase assays showed that the phosphorylation events were time- and/or concentration-dependent (Fig. 4 B and Fig. S5 B). AtTRS120 was a substrate of AtSKs in clades I-III; we did not detect phosphorylation of AtTRS120 with a clade IV AtSK in vitro (Fig. 4 B). All AtSKs that targeted AtTRS120 had a marked and consistent preference for the TRS120- $\gamma$  (S1165) site (Fig. 4 B and Fig. S5 B). In vivo, IP-MS performed on seedlings treated with the AtSK inhibitor bikinin showed a reduced extent of phosphorylation of the TRS120-S $\gamma$  peptide (Fig. S5, C and D). Conversely, seedlings treated with the BR biosynthesis inhibitor PPZ, which should relieve BR-mediated BIN2 inhibition, showed an increased extent of phosphorylation of the TRS120-S $\gamma$  peptide (Fig. S5, C and D). These in vivo observations are consistent with the in vitro kinase assays (Figs. 4 and S5). In summary, several lines of in vitro (Y2H, kinase assays) and in vivo (IP-MS, pharmacological inhibition) evidence support the conclusion that the TRAPP1 subunit AtTRS120 is a substrate of shaggy-like kinases.

### BIN2 and TRAPP1 are required for differential growth decisions under additive stress

As TRAPP1 is a BIN2 substrate, the question is whether *bin2* and *trapp1* mutants have related phenotypes. We were not able to detect cytokinesis or protein sorting defects, characteristic of *trapp1*, in semi-dominant *bin2-1* alleles (Fig. S6). We have recently shown that BIN2 is required for hypocotyl versus root trade-offs in the germinating seedling under additive stress conditions involving the simultaneous withdrawal of both light and water (Kalbfuß et al., 2022). Water stress in the dark is a “conflict-of-interest” scenario in which hypocotyl and root growth have competing interests (Kalbfuß et al., 2022). Kalbfuß et al. (2022) defined decision mutants as ones that had either insignificant hypocotyl/root-ratio responses ( $P > 0.05$ ), or

consistently wrong growth responses as compared with the wild type ( $P < 0.05$  but for an opposite growth phenotype, as depicted by red asterisks in Fig. 5, B–D; Kalbfuß et al., 2022). Under additive stress, *trapp1* null mutants failed to adjust their hypocotyl length along the same line as the wild type (red asterisks in Fig. 5, C and D; and Fig. 5 F; see Fig. S7, D and E for a direct comparison to the wild type and for the distribution of data-points). In particular, *trapp1 trs120-4* mutants had non-significant hypocotyl/root ratio responses to water withdrawal in the dark (Fig. 5 D and Fig. S7 E). In addition to comparing organ lengths, each mutant line was normalized to its corresponding wild-type ecotype on the same (PEG) plate, which helped us to take the variability between PEG plates and experiments into account and enabled us to pool biological replicates (see Materials and methods for further detail). To this end, the response to water stress in the dark was represented as a normalized response quotient (RQ). The RQ is an indication of how well each mutant responds to a given combination of stress cues and indicates how much each line deviates from the wild type. A value of 1.0 means that the mutant line behaves exactly like its corresponding wild type. This rendition shows that *bin2* higher order and *trapp1* null alleles considerably deviated from the wild type, with severely attenuated responses (Fig. 5 G and Fig. S8). We reason that decision mutants unable to integrate environmental cues might have highly variable hypocotyl versus root lengths. This high variance would, in turn, translate into an insignificant (i.e., high)  $P$  value, indicative of a low signal-to-noise ratio. We, therefore, plotted the median  $P$  values against the normalized response quotients (referred to as volcano plots; mean RQ<sub>ratio</sub> in Fig. 5 H). Wild-type ecotypes had significant  $P$  values  $< 10^{-10}$  (gray shading on the red line in Fig. 5 H, green arrow). Mutants with insignificant  $P$  values and response quotients considerably smaller than 1.0 would be considered “confused” decision mutants, and these would map in the lower left quadrant of the RQ<sub>ratio</sub> volcano plot (see peach shading in Fig. 5 H). *bin2* higher order null alleles and *trs120-4* mutants clustered together in the lower left region of the volcano plot in contrast to the near-wild-type phenotype of higher order null mutants impaired in the perception of light or water stress (*phyAphyBcry1cry2* and *pyr1pyl1pyl2pyl4* in Fig. 5, G and H; and Fig. S7, A and B; Mazzella and Casal, 2001; Park et al., 2009). We conclude that *bin2* higher order and *trapp1* null alleles are decision mutants (cf. Kalbfuß et al., 2022).

A question that arises is whether *trapp1* mutants are impaired in differential growth decisions as a secondary consequence of primary defects in morphogenesis or cytokinesis (Jaber et al., 2010; Rybak et al., 2014; Thellmann et al., 2010). The etiolation response was severely attenuated in *trapp1* mutants, but nonetheless highly significant ( $P < 0.00001$ ; Fig. S9, C, D, and F–I). Similarly, an attenuated but clear etiolation response has been shown for other cytokinesis-defective mutants including *keule* and *knolle* (Assaad et al., 2001). This shows that, despite a severe impairment in cell division and morphogenesis, cytokinesis-defective mutants are nonetheless capable of differential growth. In addition to their cytokinesis defect, *trapp1* mutants are impaired in TGN function (Ravikumar et al., 2018). We, therefore, compared *trapp1* mutants to *echidna* mutants,

which are severely impaired in TGN structure and function (Boutté et al., 2013; Gendreau et al., 2013; McFarlane et al., 2013). Both *echidna* and *trappii* mutants exhibited a severe impairment in root elongation in the light (Fig. S9, C–F and H). In contrast to *trappii*, however, *echidna* mutants had highly significant responses to additive stress that resembled the wild type in all respects (Fig. 5, E–H; and Fig. S7 F). Thus, *echidna* mutants do not qualify as decision mutants. In conclusion, a comparison to other cytokinesis-defective or TGN mutants suggests that neither cytokinesis defects nor TGN malfunction suffices to explain the *trappii trs120-4* decision phenotype.

Cellular growth parameters in *trappii* were assessed under single versus additive stress in both the hypocotyl and root tip. The width, height, and surface area of *trappii* hypocotyl cells grown in the light did not show any deviation from the wild type (Fig. 6, A and B light; Fig. S10, A–D light). In wild-type hypocotyls, both organ and cell length decreased in response to water stress in the dark (Fig. 5 A, Fig. 6 A, and Fig. S10 C). In contrast, in *trappii* mutants, organ and cell length significantly increased (red asterisks or compact letter displays in Fig. 5, C and D, Fig. 6 B, and Fig. S10, A, C, and D highlight a phenotype consistently opposite to the wild type). In root tips, we monitored meristem properties and cell length along single cortical cell files as a function of distance from the quiescent center. In the wild type, meristem size was large in the light, intermediate in the dark, and shortest under water stress in the dark (Fig. 6 C, darkW). In contrast, meristem size in *trs120-4* remained constant under the three environmental conditions tested (Fig. 6 D). We have recently shown that root growth in response to water stress in the dark is due to a combination of cell division and rapid exit from the meristem (Kalbfuß et al., 2022). An early exit from the meristem can be visualized as cell elongation in cells close to the quiescent center. This was observed under dark and darkW conditions in the wild type (green arrows in Fig. 6 C) but not in the *trappii* mutant *trs120-4* (magenta arrows in Fig. 6 D). While the curves differed under the different environmental conditions in the wild type (Fig. 6 C), these were fairly similar regardless of the environmental cue in *trs120-4* (magenta arrows in Fig. 6 D; note that the gray shading, which designates the 95% confidence interval, overlaps). We conclude that, at the cellular level, *trappii trs120-4* mutants are unable to differentially regulate their growth parameters in response to additive stress (Figs. 6 and S10). This would suffice to explain the growth defects we observed at the organ level (Fig. 5). The *trappii* cellular phenotype in the decision screen is reminiscent of that reported for *bin2* (Kalbfuß et al., 2022). In summary, *bin2* and *trappii* alleles have related phenotypes with respect to an inability to differentially regulate cell growth in both the hypocotyl and root tip in response to additive stress (Figs. 5 and 6; cf. Kalbfuß et al., 2022).

### AtTRS120 phosphovariants are functional

To assess the *in vivo* impact of the TRS120 phosphorylation status on intracellular localization, targeted point mutations (Fig. 2 C) were introduced into AtTRS120 genomic sequences fused to a C-terminal GFP tag. We refer to the ensuing site-directed mutants as TRS120 phosphovariants. The constructs

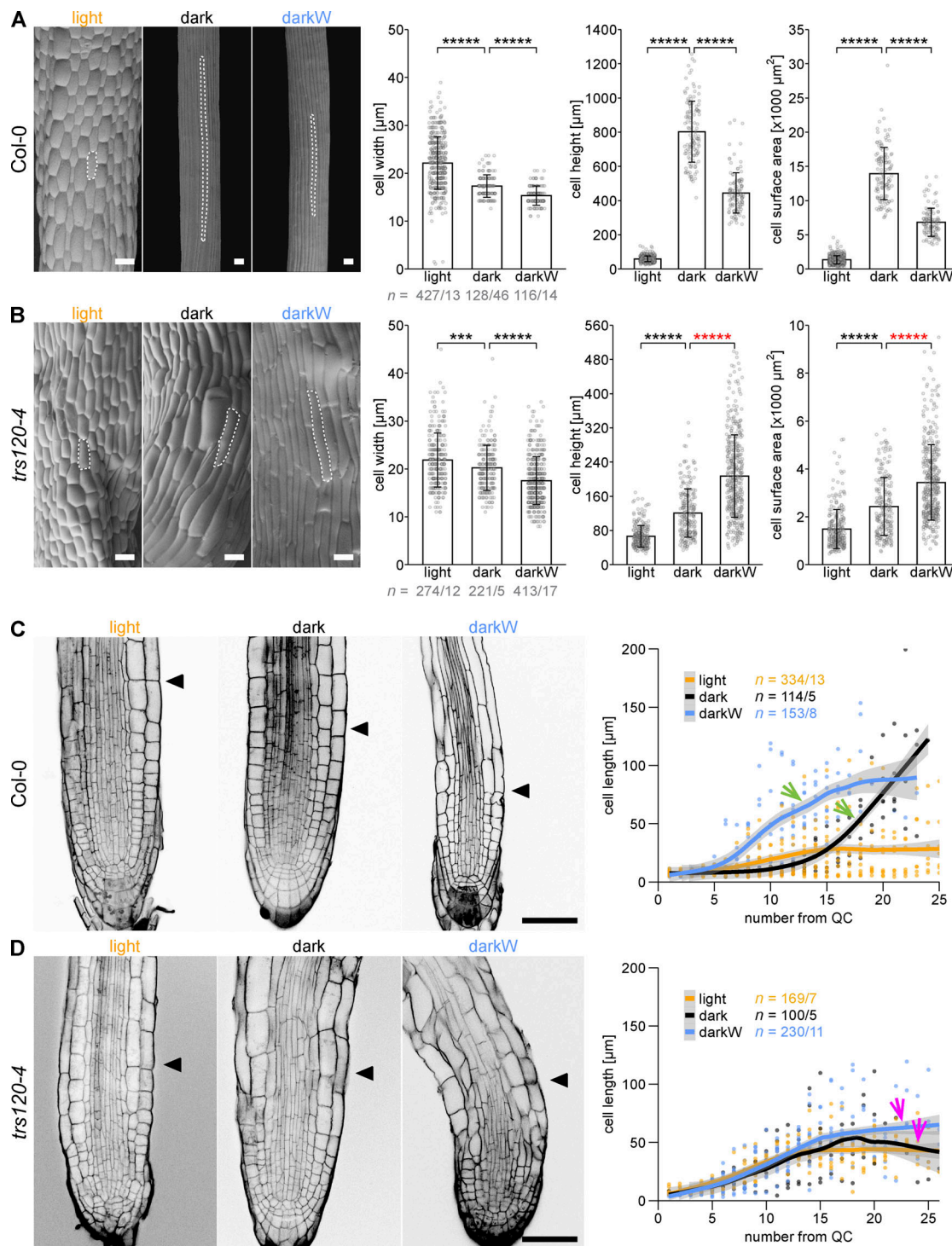
were expressed and capable of rescuing the null *trs120-4* allele in the T1 and T2 generations (Fig. S11, A and B); upon further propagation, however, signs of silencing were evident in seedlings (Fig. S11, C and D). The wild-type TRAPP11 complex resides in the cytosol, at the TGN and at the cell plate (Fig. S11 E; Naramoto et al., 2014; Qi et al., 2011; Ravikumar et al., 2018; Rybak et al., 2014). Phosphovariants had a similar appearance, but the phosphomimetic TRS120-SaβγD variant tended to be mostly membrane associated, with almost no detectable cytosolic signal (Fig. S11 E).

### TRS120-SaβγA and TRS120-SaβγD have opposite effects on seed germination under osmotic stress

We first analyzed the impact of osmotic stress on the germination frequencies of TRS120-SaβγA and TRS120-SaβγD phosphovariants (Fig. 7, A–C). As compared with the control (Col-0), the TRS120-SaβγA phosphovariant had higher seed germination rates on mannitol (Fig. 7 C). In this respect, TRS120-SaβγA was similar to the ABA-deficient mutant *aba2-1*, known to be osmotolerant with respect to seed germination (Fig. 7 C; González-Guzmán et al., 2002). In contrast, the TRS120-SaβγD phosphovariant exhibited delayed and reduced germination with lower maximal germination rates, even in the absence of mannitol (Fig. 7, A–C). With respect to its delay in germination, TRS120-SaβγD was similar to the ABA coreceptor higher order mutant *hab1-1 abi1-2 pp2ca-1*, known to be osmosensitive at germination (Fig. 7 C; Rubio et al., 2009). In summary, the non-phosphorylatable TRS120-SaβγA mutations enhanced whereas the phosphomimetic TRS120-SaβγD mutations reduced germination on mannitol.

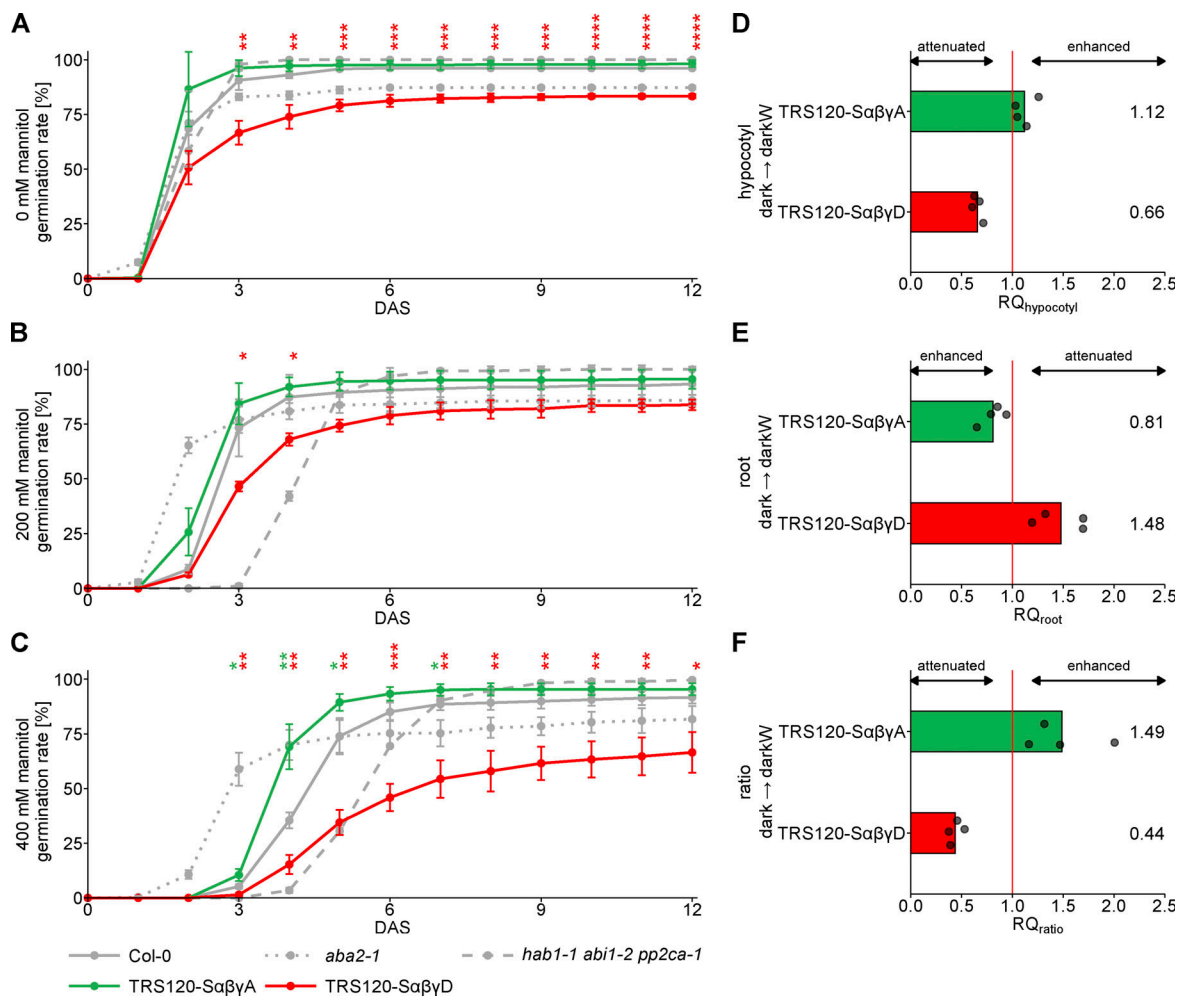
### TRS120 phosphorylation status affects hypocotyl versus root trade-offs under additive stress conditions

In light of the decision phenotypes of *bin2* and *trappii* mutants and of the observation that AtSKs such as BIN2 target TRAPP11, the question arises as to whether shaggy-like kinases regulate differential growth decisions via TRS120 phosphorylation. To test this hypothesis, AtTRS120 phosphovariants homozygous for the null *trs120-4* allele and hemizygous for the phosphovariant construct were studied under different environmental or stress conditions. The etiolation response was not impacted by the phosphorylation status of AtTRS120 (Fig. S12). In contrast, TRS120 phosphomutants had phenotypes under additive stress conditions (Fig. 7, D–F and Fig. S13, A–C). TRS120-SaβγA non-phosphorylatable variants exhibited an enhanced root response under darkW conditions (Fig. 7 E) and a strongly enhanced ratio response to water stress in the dark (mean  $RQ_{ratio} = 1.49$ ; Fig. 7 F). Conversely, the phosphomimetic TRS120-SaβγD mutants exhibited severely attenuated responses to water stress in the dark (Fig. 7, D–F; mean  $RQ_{ratio} = 0.44$ ). Thus, the non-phosphorylatable TRS120-SaβγA and the phosphomimetic TRS120-SaβγD mutations had opposite effects on hypocotyl versus root lengths under water stress in the dark, with TRS120-SaβγA exhibiting an enhanced and TRS120-SaβγD an attenuated ratio response (Fig. 7 F). Under all environmental conditions, the total seedling length of the phosphovariants did not significantly differ from that of the wild-type AtTRS120



**Figure 6. Cellular growth parameters of *trappii* mutants under single versus additive stress conditions.** Seedlings were grown in the light (orange), dark (black), or dark with  $-0.4$  MPa water stress (darkW; blue). **(A and B)** Scanning electron micrographs (SEM) of hypocotyls of (A) Col-0 wild type and (B) *trs120-4*, null *trappii* allele. The cell surface area was calculated as the product of cell width and length. *trs120-4* mutants showed the opposite hypocotyl cell height and cell surface area adaptations to dark-to-darkW conditions (red asterisks in B) than the wild-type control. Representative SEM images of seedlings grown under the specified conditions are shown (scale bar =  $40 \mu\text{m}$ ). Outlines of representative cells are highlighted by white dashed lines. Shown are means  $\pm$  SD. P values were computed with a two-tailed Student's *t* test and are represented as follows: \*\*\*:  $P < 0.001$ ; \*\*\*\*:  $P < 0.00001$ . **(C and D)** Confocal micrographs of mPS-PI stained (C) Col-0 wild type and (D) *trs120-4* null mutant root tips under single or additive stress conditions; black arrowheads mark the junction between the meristematic and elongation zones for representative root tips. 10 days after incubation, the cell lengths were measured in single cortex cell files, starting at the cortex/endodermis initials. Cell lengths of consecutive cells were mapped as a function of cell number from the quiescent center (QC). The fitted lines were generated with Local Polynomial Regression Fitting with the "loess" method in R; gray shading designates the 95% confidence interval. Col-0 seedlings grown in the dark with and without water stress show steep slopes (green arrows). In the *trappii* mutant, the curves exhibit minimal to no difference between the different screen conditions (magenta arrows). Scale bar is  $50 \mu\text{m}$ . The sample size (*n*) is given in each panel as the number of cells/number of seedlings that were analyzed (A–D). Related to Fig. S10.





**Figure 7. Responses of TRS120 phosphovariants to osmotic or additive stress.** Phosphovariants of  $P_{\text{TRS120}}::\text{TRS120}::\text{GFP}$  (Rybak et al., 2014) were in *trs120-4* homozygous backgrounds with the exception of the TRS120-SaβγD variant in A–C, which was in a hemizygous *trs120-4/+* background. (A–C) Germination of TRS120 phosphovariants under osmotic stress. Effect of (A) 0 mM, (B) 200 mM, and (C) 400 mM mannitol on seed germination of the TRS120-SaβγA, the TRS120-SaβγD mutants, and the following controls: Col-0 wild type; the ABA deficient mutant *aba2-1* and the ABA PP2C coreceptor triple knockout line *hab1-1 abi1-2 pp2ca-1*. The non-phosphorylatable TRS120-SaβγA mutation increased seed germination on higher mannitol concentrations (on day 4, we observed 70% germination in TRS120-SaβγA versus 35% germination for the control on 400 mM mannitol, C), whereas the phosphomimetic TRS120-SaβγD decreased seed germination. Shown are the means  $\pm$  SD of three technical replicates. Similar results were obtained in three independent biological replicates. Stars indicate statistical significance compared with the wild-type Col-0 calculated with a two-tailed Student's *t* test (\*:  $P < 0.05$ ; \*\*:  $P < 0.01$ ; \*\*\*:  $P < 0.001$ ; \*\*\*\*:  $P < 0.0001$ ). DAS: days after stratification. (D–F) Response quotients (RQ) of (D) the hypocotyl, (E) the root, and (F) the hypocotyl/root ratio of the non-phosphorylatable TRS120-SaβγA and the phosphomimetic TRS120-SaβγD mutants for dark-to-dark with water stress ( $-0.4$  MPa, darkW) adaptation. The divergent hypocotyl and root responses of TRS120-SaβγA and TRS120-SaβγD mutants resulted in a strong hypocotyl/root ratio phenotype under darkW conditions compared with the TRS120-WT control. TRS120-SaβγA showed an enhanced ratio adaptation, whereas TRS120-SaβγD mutants had an attenuated ratio response. RQ response quotients are normalized to the rescue mutant TRS120-WT ( $P_{\text{TRS120}}::\text{TRS120}::\text{GFP}$  in *trs120-4/trs120-4*). A value of 1 (vertical red line) corresponds to an identical adaptation to darkW conditions as the rescue mutant. Note that due to the opposite adaptations of the hypocotyl and root under the additive stress conditions (decrease in hypocotyl and increase in root length from dark-to-darkW), the respective thresholds for attenuated and enhanced responses are opposite. Dots represent biological replicates, of which there were a total of four primary transformants per line. Mean RQ values are given on the right. Related to Figs. S12 and S13.

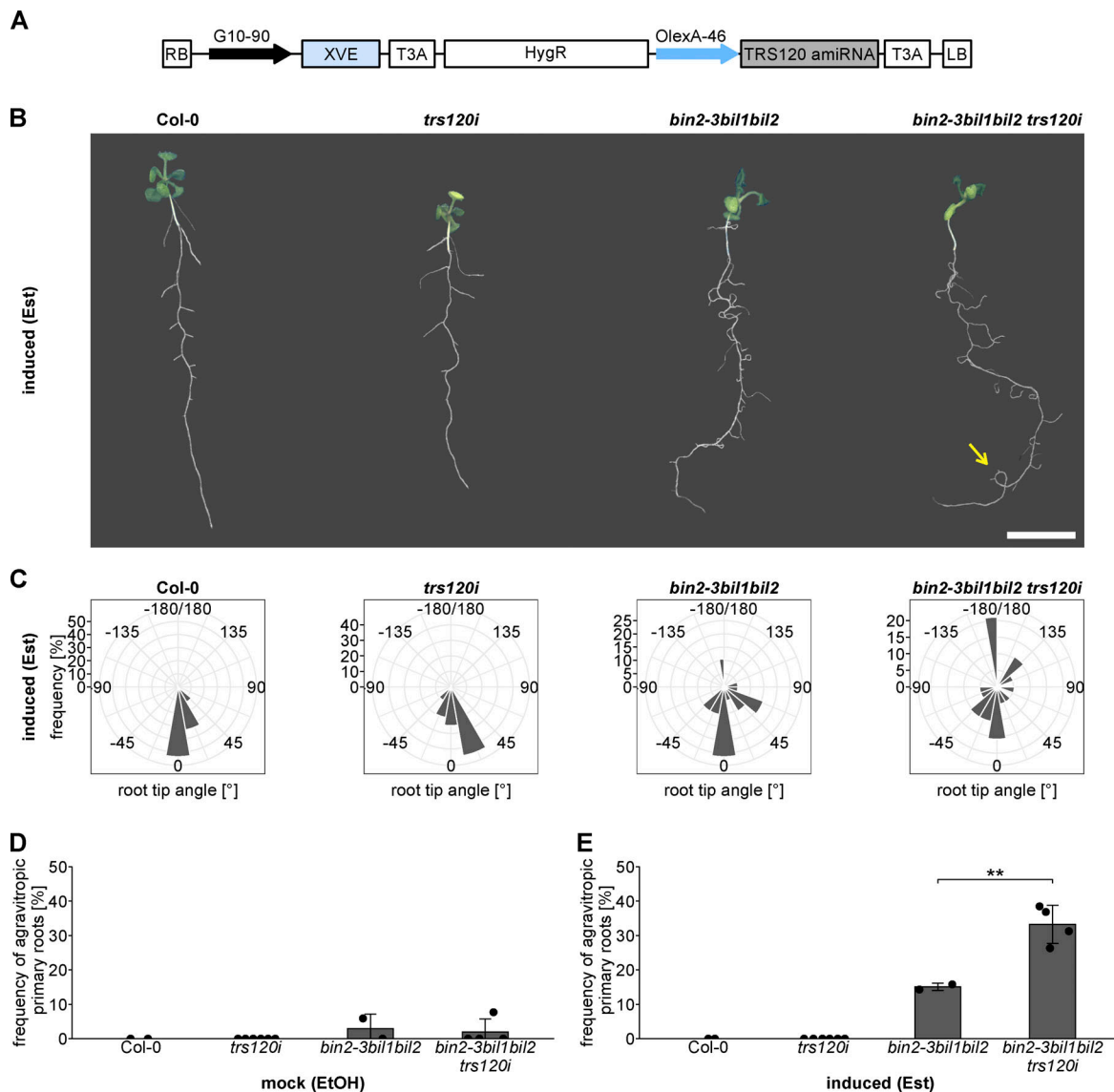
construct (Fig. S13 D), which highlights the absence of a growth defect. We conclude that the TRS120 phosphorylation status impacts the seedling's ability to differentially regulate its hypocotyl and root lengths in response to additive stress conditions. Taken together, the data show opposite impacts of non-phosphorylatable versus phosphomimetic mutations at AtTRS120 AtSK sites in terms of seed germination under osmotic stress and responses to additive stress. This suggests that TRAPP II phosphorylation by shaggy-like kinases mediates

adaptive responses to osmotic stress and to light and water availability.

#### ***bin2* higher order and *trappii* conditional mutants exhibit a synergistic genetic interaction with respect to root gravitropism**

To further address the physiological significance of the BIN2-TRAPP II interaction in vivo, we deployed higher-order mutant analysis. This approach, however, was challenged by (i) the





**Figure 8. Genetic interaction between *bin2* higher order and *trappii* conditional mutants.** Seedlings were transferred to estradiol (Est; induced) or EtOH (mock) containing media and grown vertically for 9 days. **(A)** A conditional *trs120* knock-down allele, *trs120i*. This features an artificial microRNA targeting the 5' end of the AtTRS120/TRAPPC9 coding sequence, expressed under an estradiol-inducible promoter. LB: left border; RB: right border; G10-90: synthetic constitutive promoter; XVE: encoding a chimeric transcription factor composed of the DNA-binding domain of the bacterial repressor LexA (X), the acidic transactivating domain of VP16 (V), and the regulatory region of the human estrogen receptor (E); T3A: poly(A) addition sequence; HygR: hygromycin resistance marker; OlexA-46: estradiol inducible promoter system with multiple copies of the lexA binding domain. **(B)** Representative seedling images of Col-0 (wild type), *trs120i* mutant, *bin2-3bil1bil2* and *bin2-3bil1bil2 trs120i* higher order mutants grown on estradiol. Upon induction, *trs120i* exhibited a mild phenotype, with a wavy primary root, and *bin2-3bil1bil2* a more pronounced root agravitropism. In contrast, *bin2-3bil1bil2 trs120i* mutants had an enhanced root agravitropism, growing against gravity or in loops (yellow arrow points to a 360° loop in the primary root). Scale bar is 1 cm. **(C)** Visualization of the primary root growth orientation. Primary root tip angles (excluding lateral roots) of Col-0, *trs120i*, *bin2-3bil1bil2* and *bin2-3bil1bil2 trs120i* seedlings grown on Est were measured and a frequency count with a bin width of 20° was performed. Frequency plots were generated by using a polar coordinate system. A root tip angle of 0° corresponds to vertical root tip growth in line with the gravitropic vector. Primary roots exhibiting looping (see yellow arrow in B) were scored as -180° due to their growth against gravity. A representative plot for each genotype is shown. **(D and E)** Quantification of the frequency of agravitropic primary roots upon growth on (D) mock (EtOH) or (E) induced (Est) conditions. Frequency of primary root tips growing against gravity (angles < -90° and > 90° in C) was counted per experiment. The *bin2-3bil1bil2 trs120i* higher order mutant had a more than additively enhanced agravitropic response upon induction as compared with *trs120i* or *bin2-3bil1bil2* alone (E). Note the synthetic enhancement specifically upon estradiol induction and not in the mock control (Fig. 8 D, compared with Fig. 8 E). This is indicative of a synergistic genetic interaction. Mean  $\pm$  SD bar graphs; \*\*:  $P \leq 0.01$  two-tailed Student's *t* test.  $n = 2$  independent experiments for Col-0 and *bin2-3bil1bil2*,  $n = 4$  for *bin2-3bil1bil2 trs120i*, and  $n = 6$  for *trs120i* with at least 11 seedlings per experiment.

functional redundancy between BIN2 and its homologues (Vert and Chory, 2006; Yan et al., 2009), (ii) the semi-dominant nature of *bin2-1*, (iii) the seedling lethality of *trappii* null alleles, as

well as (iv) the pleiotropic phenotypes of both *bin2-1* and *trappii* dwarfs (Li et al., 2001; Thellmann et al., 2010; Ravikumar et al., 2018; Garcia et al., 2020). To address these challenges, we

engineered a conditional *trsl20* knock-down allele, named *trsl20i*. This features an artificial microRNA that targets 5' ATRS120/TRAPPC9 sequences, expressed under an estradiol-inducible promoter (Fig. 8 A; Curtis and Grossniklaus, 2003). The *trsl20i* construct was introduced into the wild type (Col-0) and into the *bin2-3billbil2* triple knock-out mutant. Upon induction, *trsl20i* exhibited a mild and *bin2-3billbil2* a more pronounced root agravitropism (Fig. 8, B and C). The *bin2-3billbil2 trsl20i* higher order mutant had a more than additively enhanced agravitropic response upon induction as compared with *trsl20i* or *bin2-3billbil2* alone (Fig. 8, B, C, and E). This was evidenced as primary roots growing in all directions, often against gravity at 180° in *bin2-3billbil2 trsl20i* (Fig. 8, B and C). We observed synthetic enhancement specifically upon estradiol induction and not in the mock control (Fig. 8 D, compared with Fig. 8 E). This is indicative of a synergistic genetic interaction. Furthermore, it suggests that adaptive growth decisions such as gravitropism are mediated by the BIN2/AtSK-TRAPPPII interaction.

## Discussion

In this study, we explored the role of the TGN in stress responses in *Arabidopsis*. Our point of entry is the TRAPPPII complex, which has been shown to be required for TGN structure and function (Qi et al., 2011; Ravikumar et al., 2018). We performed proteomic and yeast two-hybrid screens and presented several lines of in vitro (Y2H, kinase assays) and in vivo (IP-MS, pharmacological inhibition) evidence that the TRAPPPII subunit ATRS120/TRAPPC9 is the target of AtSK kinases, including BIN2. We document differential phosphorylation of three distinct AtSK/GSK3 sites by three of the four AtSK clades. The phosphorylation status of ATRS120 impacted seed germination under osmotic stress as well as adaptive responses to additive stress in planta. We show that *bin2* and *trappii* alleles have related phenotypes with respect to an impaired adaptation to additive stress conditions, in this instance, achieved by the simultaneous withdrawal of light and water. Furthermore, *bin2* higher order and *trappii* conditional mutants exhibited a synergistic genetic interaction with respect to root gravitropism.

Like other tropisms, root gravitropism requires organ bending as a result, at least in part, of the differential sorting of PIN transporters (Friml et al., 2002; Ding et al., 2011; Konstantinova et al., 2021). PIN2 polarity has been shown to be abolished in *trappii* mutants (Qi et al., 2011; Rybak et al., 2014) and to require TGN function (Naramoto et al., 2014; Qi et al., 2011; Rybak et al., 2014; Ravikumar et al., 2018). A concern when assessing the role of the TGN in adaptive or stress responses is that TGN-related mutants typically have pleiotropic phenotypes as a consequence of their impairment in fundamental processes such as secretion, endocytosis, or sorting (Rosquete and Drakakaki, 2018; Ravikumar et al., 2018). To distinguish between primary defects in growth on the one hand and adaptive responses on the other, we monitored trade-offs between hypocotyl and root growth under additive stress conditions (Kalbfuß et al., 2022). We focus on *echidna* and *trappii* mutants as these have been shown to impact both the structure and the function of the TGN (Boutté et al., 2013; Gendreau et al., 2011, 2013;

McFarlane et al., 2013; Qi et al., 2011; Ravikumar et al., 2018). These TGN mutants had hypocotyl and root growth defects, which are characteristic of trafficking mutants (Fig. S9). In addition to their growth defects, *trappii trsl20-4* mutants had a significant hypocotyl response but in the wrong orientation as compared with the wild type (denoted by red asterisks in Figs. 5, 6, and S10) as well as an insignificant hypocotyl/root ratio response to light and water deprivation (Fig. 5). The *trappii* phenotypes described in this study are difficult to explain as mere growth defects. Rather, the inability to mediate growth trade-offs in response to additive stress provides a compelling argument for TRAPPPII as having a role in adaptive growth decisions.

Conceptually, the optimization of hypocotyl-to-root ratios can be deconstructed into four distinct stages: (i) perception, (ii) signal integration, (iii) decision making, and (iv) the implementation of resulting actions (Kalbfuß et al., 2022). To address the first stage, perception, we looked at, for example, quadruple *phyAphyBcry1cry2* photoreceptor mutants; these failed to adjust their organ lengths to light versus dark conditions but had a highly significant response to additive stress (Fig. 5, G and H, Fig. S7 A, Fig. S8, and Fig. S9, G–I; Kalbfuß et al., 2022). The opposite was true for *bin2-3billbil2* and *trappii* mutants, which were able to respond to single stress factors but not to additive stress (Figs. 5, 6, and S10; Kalbfuß et al., 2022). Shaggy-like kinases integrate a vast number of signaling pathways (Lv and Li, 2020; Youn and Kim, 2015; Li et al., 2021; Song et al., 2023; Planas-Riverola et al., 2019). Accordingly, we have postulated that the *bin2-3billbil2* “decision” phenotype under conflict-of-interest scenarios is primarily due to signal integration (Kalbfuß et al., 2022). Prime candidates for the fourth stage, execution or implementation of the action, are *echidna* mutants, which are impaired in the formation of secretory vesicles and cell elongation (Boutté et al., 2013; Gendreau et al., 2013; McFarlane et al., 2013); these had highly significant adaptive responses—in the correct orientation—despite their growth defects (Fig. 5 E). The question arises as to how to categorize *trappii* mutants in the above conceptual framework. Despite having abnormally short hypocotyls or roots, *trappii* mutants still exhibited differential length increase depending on light availability (Fig. S9). This shows that they are able to perceive and respond to light.

If TRAPPPII is primarily involved neither in perception nor in execution, this would place it at the signal integration and/or decision-making steps of adaptive growth decisions. The TRAPPPII interactome is vast and complex, with a surprising number of signaling components implicated in responses to abiotic cues (Figs. 1 and S1). This suggests a role for TRAPPPII in signal integration. Conversely, the BIN2 signaling network includes secretion, endocytosis, autophagy, TGN, endoplasmic reticulum (ER), cell wall, and cytoskeleton (Kim et al., 2023). Thus, there is a considerable compartmental overlap between the BIN2 network and the TRAPPPII interactome. Nonetheless, TRAPPPII was not reported among the 482 members of the BIN2 signaling network identified by proximity labeling (Kim et al., 2023). The discrepancy could be due to the different methods used: yeast two-hybrid and proteomics in this study versus proximity labeling and phosphoproteomics in Kim et al. (2023). However, a multiomics approach identified ATRS120-S971

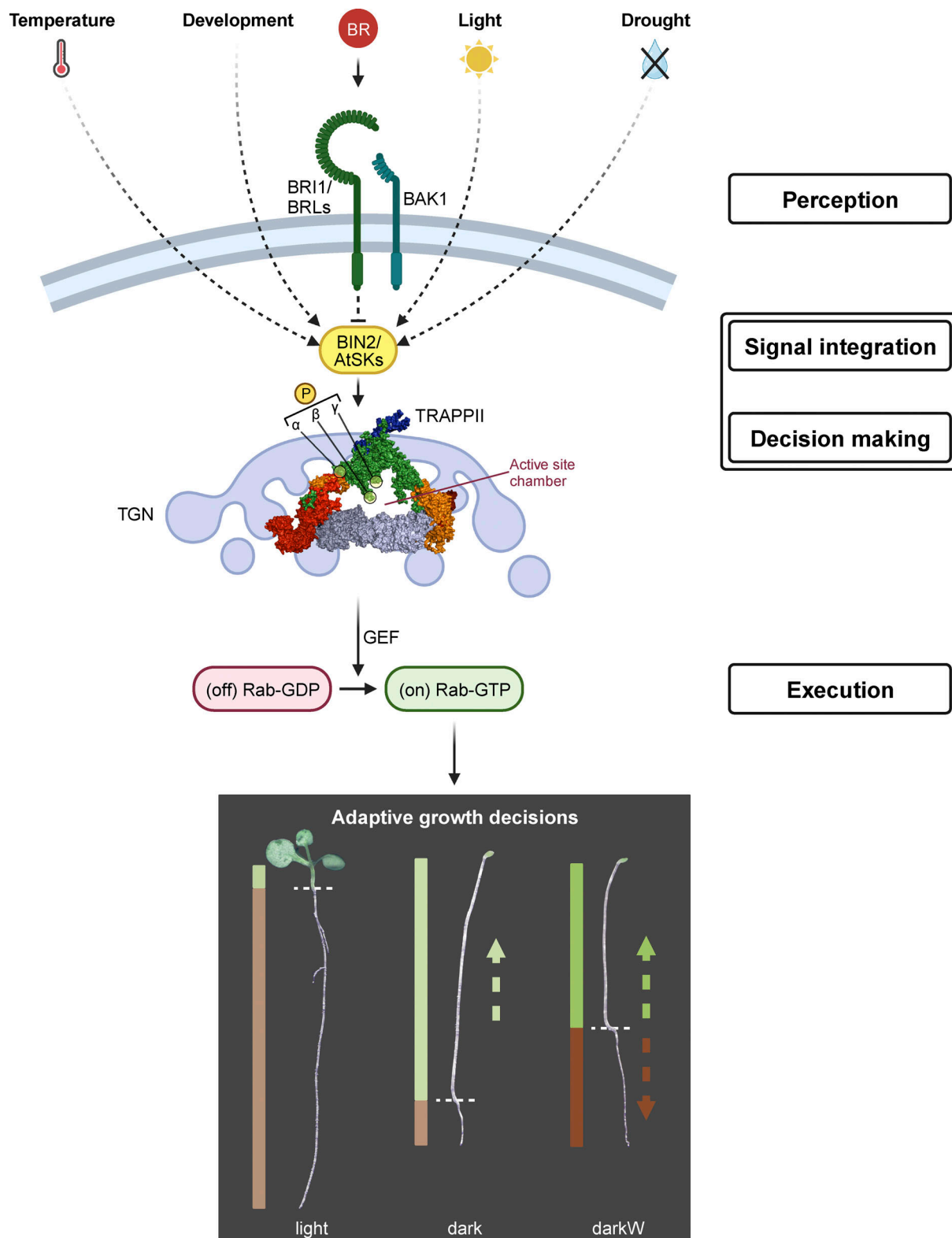


Figure 9. **Flow diagram suggesting how BIN2 might mediate plant adaptive responses by phosphorylating the TRAPP II complex.** Shaggy-like kinases such as BIN2 integrate a vast number of signaling pathways and, together with receptor complexes at the cell surface, comprise a surveillance system fine-tuned to both biotic and abiotic cues (see text for further detail). BIN2 resides in the plasma membrane (PM) and in the cytosol and TRAPP II resides at the cytosol and in the TGN (Vert and Chory, 2006; Qi et al., 2011; Naramoto et al., 2014; Rybak et al., 2014; Ravikumar et al., 2018). We propose that, in the cytosol, the BIN2-TRAPP II interaction serves in the relay of information from the PM to the TGN. We posit that signal integration and decision-making occur at the AtSK-TRAPP II interface. A surface view of the AtTRAPP II complex with AtTRS120 GSK3 phosphorylation sites facing the predicted active site chamber is depicted as AlphaFold structures of AtTRS120/TRAPPC9 and CLUB/AtTRS130/TRAPPC10 mapped onto the cryo-EM-generated structures of yeast TRAPP II (Mi

et al., 2022; see Fig. 3 for a cross-kingdom structural alignment). Downstream of TRAPP1, Rab GTPase cascades are postulated to be implicated in implementing decisions reached by the AtSK-TRAPP1 module. We speculate that the phosphorylation status of AtTRS120 modulates the specificity of the putative TRAPP1 GEF activity, thereby differentially activating distinct Rab GTPase cascades. In the lower panel, we show one example of an adaptive growth decision in 10-day-old seedlings (Col-0 wild type). Bar plots depict hypocotyl (green) versus root (beige-brown) lengths. Light: Light-grown seedling with a short hypocotyl and a long root. Dark: A seedling germinated in the dark with a long hypocotyl and a short root. DarkW: Water deprivation in the dark; the hypocotyl is shorter and the root longer than under dark conditions. The dotted green arrow (dark, darkW) represents the incentive for hypocotyl elongation in search of light and the brown arrow (darkW) the incentive for root growth in search of water. Thus, darkW is a “conflict-of-interest” scenario in which hypocotyl and root growth have competing interests (Kalbfuß et al., 2022). Figure generated with <https://BioRender.com>.

(encompassed by our identified  $\beta$  site AtTRS120-S971:S973: S974:S975; Fig. 2 C) as being differentially phosphorylated in response to brassinolide treatment (Clark et al., 2021). This provides an additional line of in vivo evidence for a BIN2-AtTRS120 interaction and, consistently with our PPZ experiment (Fig. S5 D), suggests that TRAPP1 phosphorylation is, at least in part, brassinosteroid-regulated.

To explore the biological significance of the AtSK-TRAPP1 interaction, we probed the phenotypes of TRAPP1 phospho-variants. We found that these had an impact on hypocotyl versus root growth trade-offs in response to additive stress (Fig. 7, D-F). Furthermore, the non-phosphorylatable TRS120-S $\alpha\beta\gamma$ A variant had an enhanced root adaptation whereas the phosphomimetic variant decreased root growth under additive stress (Fig. 7, D-F), which is consistent with the negative regulation of growth by BIN2 and other AtSKs. We have previously described plant-specific domains or subunits predicted to be at the dimer interface of the *Arabidopsis* TRAPP1 complex (marked in green in Fig. 2 D; Garcia et al., 2020; Kalde et al., 2019). Interestingly, BIN2 interacts with the plant-specific C-terminal domain of AtTRS120, while MAP65-3 interacts with plant-specific C-terminal domains of the TRAPP1-specific subunits CLUB/AtTRS130 and AtTRS120 (Steiner et al., 2016). This presents intriguing implications regarding the potential role of the AtSK-TRAPP1 module in meeting the unique demands of endomembrane traffic in plants. Plant and animal cells differ in numerous ways, many of which can be attributed to the presence of the plant cell wall. Novel or expanded families of vesicle-trafficking genes are implicated in cell wall assembly (Assaad, 2001). Cell wall deposition and remodeling under any growth response in plants. Growth in the face of challenging, restrictive environments is a distinctive survival strategy unique to plants (Assaad, 2001). In this study, we look at the tight regulation of differential growth that enables plants to thrive under multiple stress conditions, in the absence of a carbon or energy source.

The observation that the *trapp1* decision phenotype was not shared by *echidna* mutants raises the question as to what facet of TGN function is required for responses to additive stress. ECHIDNA and TRAPP1 have been shown to have overlapping roles in basal TGN functions such as secretion (Ravikumar et al., 2018). In addition, ECHIDNA regulates ER stress and immunity whereas TRAPP1 has roles in cytokinesis and in the establishment of cell polarity that appear to be independent of ECHIDNA (Liu et al., 2023; Ravikumar et al., 2018). In the literature, there are a few examples of null mutants that are associated with the TGN and that have a positive influence on growth. One such example is a null allele of a core TRAPP1 subunit that enhances root growth also in the absence of stress in maize (Zhao et al.,

2023). The TRAPP1 complex has two distinct possible molecular functions. First, it has been postulated to act as a multisubunit tethering complex, even though direct evidence is lacking (Ravikumar et al., 2017; Brunet and Sacher, 2014; Kim et al., 2016; Pinar et al., 2019). Second, it has been shown to act as a Rab GTPase guanine nucleotide exchange factor (Rab-GEF; Cai et al., 2005; Morozova et al., 2006; Pinar et al., 2015; Thomas and Fromme, 2016; Riedel et al., 2018). Rab-GEFs act as central cellular switches that can activate Rab GTPase cascades, which are in turn crucial for the development of polarity and directional growth in plants (Elliott et al., 2020). Indirect in vivo evidence suggests that *Arabidopsis* TRAPP1 acts as a GEF for Rab-A GTPases, orthologues of the RAB11/Ypt31 families known to be activated by fungal and metazoan TRAPP1 (Qi and Zheng, 2011; Kalde et al., 2019). In *Arabidopsis*, Rab-A GTPases are TGN-associated and comprise a highly expanded class with 26 members (Kalde et al., 2019; Elliott et al., 2020). In contrast to ECHIDNA, which is required for the biogenesis of secretory vesicles and for growth generically, as a putative, Rab-A GEF TRAPP1 has the ability to mediate all the highly diverse facets of TGN function. In a judgment-decision model for plant behavior, judgment is a composite of discrimination, assessment, recognition, and categorization (Karban and Orrock, 2018). In this context, it is noteworthy that the most expanded Rab GTPase family is TGN-associated, suggestive of a tremendous degree of discrimination, specialization, and subcompartmentalization at the TGN. Atomic structures of yeast and metazoan TRAPP1 depict a conserved triangular structure around the central active site chamber in which TRS120/TRAPPC9 and TRS130/TRAPPC10 form tongs that hold the core complex in place (Galindo et al., 2021; Mi et al., 2022; Bagde and Fromme, 2022). In a cross-kingdom structural alignment, AtTRS120 and CLUB/AtTRS130 aligned along their yeast orthologues in the same overall structure (Fig. 3). In yeast, TRS120/TRAPPC9 has been proposed to comprise a lid that encloses the active site chamber of the TRAPP1 GEF (Bagde and Fromme, 2022). Interestingly, the  $\beta$  and  $\gamma$  phosphorylation sites we have identified in AtTRS120/TRAPPC9 face the active site chamber, including the RAB11/Rab-A binding pocket, proposed by Mi et al. (2022) and Bagde and Fromme (2022) (Fig. 3 A). It is, therefore, tempting to speculate that the phosphorylation status of AtTRS120/TRAPPC9 modulates the specificity of the putative GEF activity of *Arabidopsis* TRAPP1 (Kalde et al., 2019).

Our study highlights the possible relevance of the AtSKs-TRAPP1 interaction for adaptive growth decisions (Fig. 9). Shaggy-like kinases such as BIN2 integrate a vast number of signaling pathways and, together with receptor complexes at the cell surface, comprise a surveillance system fine-tuned to both



biotic and abiotic cues (Lv and Li, 2020; Planas-Riverola et al., 2019; Youn and Kim, 2015; Li et al., 2021; Song et al., 2023). Via the cytosol, the AtSKs would then transmit this information by mediating the phosphorylation status of the TRAPPPII complex. TRAPPPII would, in turn, mediate TGN function. As an early endosome, the TGN is a central hub in the flow of information to and from the cell surface. It is also intimately connected to the late endosome (or the pre-vacuolar compartment) and to the Golgi, which provides complex polysaccharides as building blocks for the deposition of new cell walls. Thus, the AtSK-TRAPPPII interaction would integrate all levels of cellular organization. We posit that signal integration and decision-making occur at the AtSK-TRAPPPII interface and that, downstream of TRAPPPII, Rab GTPase cascades are implicated in implementing decisions reached at the AtSK-TRAPPPII module (Fig. 9). Sorting and trafficking decisions at the TGN would enable plants to respond to developmental or environmental signals via differential growth or various forms of movement.

Plants exhibit plasticity in their growth, meaning they can adjust their growth patterns in response to environmental cues such as light, temperature, and nutrient availability. It has been argued that plant phenotypic plasticity “is the result of signal integration—a process that requires cell-cell communication, and that results in adaptive forms of movement not to be interpreted as automatic and programmed” (Garzón and Keijzer, 2011). Movement in plants involving organ bending requires the polar distribution of morphogens such as auxin. This, in turn, requires the polarized localization of auxin transporters such as PINs. The *Arabidopsis* TRAPPPII complex has been shown to play a pivotal role in a variety of sorting decisions including the polar localization of PIN2 proteins (Qi et al., 2011; Rybak et al., 2014; Ravikumar et al., 2018). This study presents evidence that AtSK-TRAPPPII interactions regulate plant adaptation. Whether or not different AtSKs have distinct roles in TRAPPPII phosphorylation could not be resolved due to high sequence similarity between AtSK homologs and some experimental limitations. Validation will be required to address whether the *Arabidopsis* TRAPPPII complex shares the conserved triangular structure with yeast and metazoan TRAPPPII, as suggested by extensive pair-wise Y2H tests and by AlphaFold predicted structures of individual subunits (Kalde et al., 2019; this study). How environmental or developmental cues regulate the cargo composition and sorting of TGN vesicles via the AtSK-TRAPPPII module remains unclear. Future experiments will explore the impact of the TRAPPPII phosphorylation status on protein sorting, cell polarity, and the Rab specificity of TRAPPPII as a putative GEF. Furthermore, downstream components that govern physiological changes in response to TRAPPPII phosphorylation will need to be determined. The presence of the TOR kinase in the TRAPPPII interactome (Fig. 1) is intriguing, as TOR integrates information about nutrient and energy availability, and has recently been shown to regulate actin dynamics as a function of ATP levels (Dai et al., 2022); it is tempting to speculate that TOR could provide information on nutrient and energy levels to the AtSK-TRAPPPII decision module. In plants, the trans-Golgi network (TGN) plays a critical role in the relay of information between the cell surface and intracellular compartments. An

AtSK-TRAPPPII interaction would instruct the TGN, a central and highly discriminate cellular hub, as to how to mobilize and allocate resources to optimize survival under limiting or adverse conditions.

## Materials and methods

### Lines and growth conditions

All the mutant lines used in this study are listed in Table S2. Seedling-lethal mutants were propagated as hetero- or hemizygotes. Insertion lines were selected via the TAIR and NASC websites (Swarbreck et al., 2008). Plants were grown in the greenhouse under controlled temperature conditions and with supplemental light, or under controlled growth chamber conditions at the TUMmesa ecotron (16/8 h photoperiod at 180  $\mu\text{mol m}^{-2}\text{s}^{-1}$ ). Seeds were surface sterilized, stratified at 4°C for 2 days, and plated on ½ MS medium supplemented with B5 vitamins (G1019; Sigma-Aldrich). For confocal microscopy, the media was additionally supplemented with 1% sucrose. Plates were incubated at 22°C in constant light (80  $\mu\text{mol m}^{-2}\text{s}^{-1}$ ). The root tips of 5-day-old plate-grown seedlings were used for confocal microscopy. 7-day-old plate-grown seedlings were used for coimmunoprecipitation.

### Coimmunoprecipitation (IP)

For CLUB/AtTRS130:GFP, we used 3 g of inflorescences per IP experiment. For TRS120:GFP, 3 g of light-grown seedlings were harvested on day 7. For bikinin treatment, seedlings were treated for 30 min with 25  $\mu\text{M}$  bikinin at day 7. For PPZ treatment, 5-day-old seedlings were treated with 2  $\mu\text{M}$  PPZ for 48 h; respective mock treatments were conducted in parallel.

Coimmunoprecipitation experiments were carried out as described previously (Rybak et al., 2014). Briefly, seedling or inflorescence lysates were incubated with GFP-trap beads (gta, Chromotek). After washing away all non-binding proteins, 70  $\mu\text{l}$  2× NuPAGE LDS + 25 mM dithiothreitol (DTT) buffer (Thermo Fisher Scientific) was added and boiled at 70°C for 10 min to denature the bait and all interaction partners.

In-gel trypsin digestion was performed according to standard procedures (Shevchenko et al., 2006). Briefly, the samples were run on a NuPAGE 4–12% Bis-Tris Protein Gel (Thermo Fisher Scientific) for 3 min. Subsequently, the still not size-separated single protein band per sample was cut out of the gel, reduced (50 mM DTT), alkylated (55 mM chloroacetamide), and digested overnight with trypsin (Trypsin Gold, Promega). The resulting peptides were analyzed by mass spectrometry. Detailed information on the mass-spectrometric data acquisition and analysis is provided in the respective LC-MS/MS sections below. See data availability for access to the raw data.

### Molecular techniques and site-directed mutagenesis (SDM)

Standard molecular techniques were used for subcloning (Sambrook et al., 1989). For subcloning for expression in *Escherichia coli* (*E. coli*) or yeast, we used cDNA clones developed by the plant genome project of RIKEN Genomic Sciences Center (Seki et al., 1998, 2002).

Non-phosphorylatable and phosphomimetic TRS120 phosphosite variants (SaA, SβA, SyA, SaβA, SaγA, SβγA, SaβγA and

SαD, SβD, SγD, SαβD, and SαβγD; Table S3) were generated using a DpnI-mediated Site-Directed Mutagenesis protocol and the GATEWAY cloning system. Briefly, site-directed mutations were introduced into the template construct via polymerase chain reaction using mutagenic primers with the desired mutations (see Table S3 for substituted amino acids and used primers) and the KOD Hot Start DNA Polymerase (Novagen) for strand extension. Subsequently, the methylated non-mutated DNA template was digested with the DpnI endonuclease (Thermo Fisher Scientific). Mutated vectors were transformed in *E. coli* DH5α for nick repair and amplification of the plasmids. After subsequent purification, the constructs were sequenced to ensure correct mutagenesis. For the mutation of two or three phosphorylation sites, sequential mutagenesis was carried out using already mutated vectors as templates.

For Y2H assays, mutations of phosphorylation sites were introduced into TRS120-T2 cDNA sequences (spanning amino acids 499–1187; Rybak et al., 2014) fused to GAL4-AD (pAD-GAL4). N-terminal GST-fused TRS120-T2 phosphovariants (pDEST15) were used for in vitro kinase assays. For in planta experiments (confocal imaging, stress assays, protein expression, etc.) the genomic construct  $P_{\text{TRS120}}::\text{TRS120:GFP}$  in the pCAMBIA2300 plasmid (Rybak et al., 2014) was used as an SDM template. The final phosphovariant constructs were transformed into the *Agrobacterium tumefaciens* strain GV3101 (pMP90) and introduced into the *Arabidopsis* hemizygous null *trs120-4* background using the floral dip method (Clough and Bent, 1998). Transgenic lines were selected on ½ MS medium supplemented with 50 µg/ml kanamycin.

### Generation of inducible *trs120* knock-down lines

To generate an inducible *trs120* knock-down mutant, named *trs120i*, an artificial microRNA targeting the 5' end of AtTRS120 was designed with the Web MicroRNA Designer 3 (Schwab et al., 2006). The designed amiRNA sequence (5'-TATAACTCTTAC AAGCGGCAT-3') was introduced in the miR319a precursor and synthesized as a gene strand (Eurofins) with attached attB sites for GATEWAY compatibility (see Table S4 for full gene strand sequence). The TRS120 amiRNA precursor was first cloned into the pDONR207 entry vector and subsequently into the estradiol inducible pMDC7 vector (Curtis and Grossniklaus, 2003) using Gateway cloning. The construct was introduced into the *A. tumefaciens* strain GV3101 (pMP90) and inserted into Col-0 wild-type and *bin2-3billbil2* mutant plants using the floral dip method (Table S2; Clough and Bent, 1998). Transgenic lines were selected on ½ MS medium supplemented with 20 µg/ml hygromycin B.

### Yeast two-hybrid (Y2H)

Y2H pairwise tests were performed as described in Altmann et al. (2018). Briefly, open reading frames (ORFs) encoding CLUB/AtTRS130 truncations (C2, C3), TRS120 truncations (T1, T3), and BIN2 were transferred by Gateway cloning into the GAL4 DNA-binding domain (DB) encoding Y2H vector pDEST-pPC97, and subsequently transformed into the yeast strain Y8930. These constructs were screened by yeast mating against TRAPP1 subunits and truncations thereof (CLUB-C1, -C2, -C3

and TRS120-T1, -T2, -T3) or the TRS120-T2 truncation and its phosphomutants TRS120-T2 SαD, SβD, SγD, SαβD, and SαβγD fused to the GAL4 activation domain (AD) in the yeast strain Y8800. The interaction was assayed by growth on selective plates using the *HIS3* reporter and using 1 mM 3-Amino-1,2,4-triazole (3-AT) to suppress background growth. All candidate interactions were verified by pairwise one-on-one mating in four independent experiments. Only pairs scoring positives in all four assays were considered as bona fide interaction partners. The use of low-copy plasmids, weak promoters, the counter-selectable marker *cyh2<sup>S</sup>* on the AD-Y plasmid as well as semi-quantitative scoring of quadruplicate tests has been shown to reliably eliminate experimental artifacts and hence false-positives. With the exception of the CLUB-C1 truncation, all TRAPP1 truncations and catalytic core subunits used in pairwise tests yielded at least one positive interaction (see also Kalde et al., 2019; Garcia et al., 2020), and this was used as an internal positive control for the interpretation of negative interaction data.

### In vitro kinase assays

Glutathione S-transferase (GST):BIN2 (Li and Nam, 2002) and GST:TRS120-T2 WT or phosphovariants were expressed in *E. coli* (Rosetta-gami strain; 71351-M; Novagen) under constant shaking for 20 h at 25°C or 20 h at 18°C, respectively. The expressed proteins were affinity-purified with GST-tags. After sonication of the samples in 1× PBS, 1 mM PMSF, 1 mg/ml lysozyme, and 1% Triton X-100, the bacterial cell rests were centrifuged for 30 min at 16,000 g. Supernatants were incubated for 2 h with glutathione Sepharose 4 Fast Flow Beads (GE Healthcare) while rotating. After washing the samples five times, the GST-tagged proteins were eluted with 10 mM glutathione and concentrated by ultrafiltration.

In vitro kinase assays with radiograph readout were performed as described by Kim et al. (2012), with some adaptations. In short, ~0.1 µg GST:BIN2 and ~0.5 µg of GST:TRS120-T2 WT or phosphovariant were incubated in 20 mM Tris pH 7.5, 1 mM MgCl<sub>2</sub>, 100 mM NaCl, 1 mM DTT, 100 µM ATP, and 10 µCi ATP [ $\gamma$ -<sup>32</sup>P] for 3 h at 22°C in motion. The kinase reaction was stopped by adding 2× SDS sample buffer and by boiling the samples for 10 min. Protein phosphorylation was analyzed by SDS-PAGE followed by autoradiography acquired on a Typhoon Trio imager (GE Healthcare) or a Personal Molecular Imager (PMI) system (Bio-Rad). For quantification, mean gray values of phosphosignal bands were measured using Fiji - ImageJ, and the background signal was subtracted. Phosphosignals were normalized to the protein amount, and relative intensities to the non-mutated TRS120-T2 wild-type control were calculated.

In vitro kinase assays with mass-spectrometry readout were performed to determine specific phosphorylation sites. For each reaction, 10 µg of the substrate (TRS120-T2) and different dilutions of the kinase (undiluted, 1:1, 1:5, 1:10, 1:20, or 1:100 as indicated in the figure panels) were incubated for 0, 15, 30, 120, 240, and 360 min in a kinase buffer (20 mM Tris HCl pH 7.8, 100 mM NaCl, 1 mM MgCl<sub>2</sub>, 1 mM DTT, 1 mM ATP). For the negative controls, one sample with the highest kinase concentration and the longest incubation time was incubated in a

kinase buffer without ATP. For the kinase-dead control, the kinase was heat-inactivated prior to the incubation with its substrate. To stop the reaction, samples were heated at 95°C for 5 min. Samples were prepared for mass spectrometry by reduction with 10 mM dithiothreitol (DTT) (30 min at 30°C) and alkylation with 55 mM chloroacetamide (CAA) in the dark (30 min at 25°C). Afterward, the samples were diluted four-fold in 50 mM  $\text{NH}_4\text{HCO}_3$  and proteolytically digested with trypsin (1 h at 30°C, Trypsin Gold Mass Spectrometry Grade, Promega) in a ratio of 1:100, i.e., 10  $\mu\text{g}$  protein sample were digested with 0.1  $\mu\text{g}$  trypsin. After the 1 h trypsin incubation time, the same amount of trypsin was added a second time. After 16 h of incubation, the enzymatic reaction was stopped with 1% formic acid (FA). Afterward, stage tip purification was performed. To this end, the pH of the samples was measured ( $\text{pH} < 3$ ) with pH strips (MColorpHast; Merck). The in-house built C18 tips (three disks,  $\varnothing$  1.5 mm, C18 material, 3 M Empore) were equilibrated consecutively with 250  $\mu\text{l}$  100% ACN, 250  $\mu\text{l}$  elution solution (40% ACN, 0.1% FA) and 250  $\mu\text{l}$  washing solution (2% ACN, 0.1% FA) at 1,500 g. The sample was loaded onto the column (5 min at 500 g) and desalted with three washing steps (washing buffer: 2% ACN, 0.1% FA; 2 min at 1,500 g, 250  $\mu\text{l}$ ). Finally, the peptides were eluted with two times 40  $\mu\text{l}$  elution solution (40% ACN, 0.1% FA) for 2 min at 500 g. The solvent of all samples was completely subtracted in a centrifugal evaporator (Centrivap Cold Trap -50; Labconco), freshly suspended before MS measurement in washing solution (2% ACN, 0.1% FA), and  $\sim 0.25$   $\mu\text{g}$  of the digest was injected into the mass spectrometer per measurement.

#### LC-MS/MS data acquisition for in vitro kinase assays and coimmunoprecipitations

Generated peptides were analyzed on a Dionex Ultimate 3000 RSLCnano system coupled to a Q-Exactive HF-X mass spectrometer (Thermo Fisher Scientific). Peptides were delivered to a trap column (ReproSil-pur C18-AQ, 5  $\mu\text{m}$ , Dr. Maisch, 20 mm  $\times$  75  $\mu\text{m}$ , self-packed) at a flow rate of 5  $\mu\text{l}/\text{min}$  in HPLC grade water with 0.1% formic acid. After 10 min of loading, peptides were transferred to an analytical column (ReproSil Gold C18-AQ, 3  $\mu\text{m}$ , Dr. Maisch, 450 mm  $\times$  75  $\mu\text{m}$ , self-packed) and separated using a linear gradient (50 min for coimmunoprecipitation samples and 30 min for kinase assay samples) from 4% to 32% of solvent B (0.1% formic acid in acetonitrile and 5% (vol/vol) DMSO) at 300 nl/min flow rate. Both nanoLC solvents (solvent A: 0.1% formic acid in HPLC grade water and 5% (vol/vol) DMSO) contained 5% DMSO to boost MS intensity. The Q-Exactive HF-X mass spectrometer was operated in a data-dependent acquisition (DDA) and positive ionization mode. MS1 spectra (360–1,300 m/z) were recorded at a resolution of 60,000 using an automatic gain control (AGC) target value of  $3 \times 10^6$  and a maximum injection time (maxIT) of 45 ms. Up to 18 peptide precursors were selected for fragmentation in the case of the full proteome analyses. Only precursors with a charge state 2–6 were selected and dynamic exclusion of 25 s was enabled. Peptide fragmentation was performed using higher energy collision-induced dissociation (HCD) and a normalized collision energy (NCE) of 26%. The precursor isolation window

width was set to 1.3 m/z. MS2 resolution was 15,000 with automatic gain control (AGC) target value of  $1 \times 10^5$  and maximum injection time (maxIT) of 25 ms.

#### LC-MS/MS data analysis for coimmunoprecipitations

For AtTRS120 coimmunoprecipitations, peptide identification and quantification were performed using the software MaxQuant (version 1.6.1.0) (Cox and Mann, 2008; Tyanova et al., 2016a) with its built-in search engine Andromeda (Cox et al., 2011). MS raw data were searched against an *Arabidopsis thaliana* reference database (Araport, updated 2016-06) supplemented with common contaminants (built-in option in MaxQuant). Carbamidomethylated cysteine was used as a fixed modification; variable modifications included oxidation of methionine and N-terminal protein acetylation. Trypsin/P was specified as a proteolytic enzyme with up to two missed cleavage sites. Label-free quantification (Cox et al., 2014), match-between-runs intensity-based absolute quantification (iBAQ), and label-free quantification (LFQ) options were enabled. Precursor tolerance was set to 4.5 ppm, and fragment ion tolerance to 20 ppm. Results were adjusted to 1% false discovery rate (FDR) on peptide spectrum match (PSM) level and protein level employing a target-decoy approach using reversed protein sequences.

Perseus (Tyanova et al., 2016b) and Python with its packages matplotlib (Hunter, 2007), pandas (McKinney, 2010), and seaborn (Waskom, 2021) were used for statistical data analysis. Normalization was performed by median centering. LFQ intensities were  $\log_2$ -transformed. Protein groups identified only in a single sample were removed from the analysis. Missing values were replaced from a normal distribution (width = 0.3, down shift = 1.8). Protein fold changes and their significance were computed via a two-sample *t* test. A fold change of  $>3$  and a *P* value  $<0.05$  was regarded as significant.

For CLUB/AtTRS130, IP-MS data were analyzed following the method used in Kalde et al. (2019). In short, raw MS files were loaded into the MaxQuant software (version 1.5.7.4; Cox and Mann, 2008) and searched against an *A. thaliana* RefSeq database (Araport11\_genes.201606.pep.fasta). Trypsin was specified as a proteolytic enzyme and up to two missed cleavages were allowed. Protein identifications were filtered at a 1% protein false discovery rate on PSM and protein levels. In downstream analysis, we used the intensity-based absolute quantification (iBAQ) (Schwanhäusser et al., 2011), whose values were calculated using the implemented iBAQ algorithm in the MaxQuant software. Before statistical analysis, iBAQ intensities were normalized according to the iBAQ of the bait protein used in coimmunoprecipitation, and missing values were replaced by a constant (1,000). Then the iBAQ intensities were  $\log_2$ -transformed. The protein abundance between control and IP samples was compared using a *t* test to evaluate the statistical significance. Ratios of protein abundance between control and IP were considered high if larger than 8 in the  $\log_2$  scale, and intermediate if in the 5–8 range ( $\log_2$  scale).

#### LC-MS/MS phosphopeptide analysis

For a targeted analysis of the AtTRS120 phosphostatus in kinase assays (Fig. 4 B and Fig. S5 B) and in the bikinin and PPZ data



sets (Fig. S5 D), MS1 chromatograms from selected phosphopeptides were extracted and analyzed using the Skyline software (MacLean et al., 2010). Peak integration, interferences, and integration boundaries were reviewed manually for all precursors. For the bikinin and PPZ treatments, a two-tailed Student's *t* test was performed to determine statistical significance. For the kinase assay, raw intensities as exported from Skyline were plotted.

### Light and electron microscopy

For scanning electron microscopy, a Zeiss (LEO) VP 438 microscope was operated at 15 kV. 10-day-old seedlings from the differential growth decision assay were placed onto stubs and examined immediately in low vacuum. Confocal microscopy imaging was performed at controlled room temperature (22°C) using an Olympus (<https://www.olympus-ims.com>) Fluoview 1000 confocal laser scanning microscope (CSLM) with a 40× 0.9 NA or a 60× 1.2 NA water immersion objective and a Leica (<https://www.leica-microsystems.com>) TCS SP8 X Hyvolution CSLM with a 40× 1.1 NA or 63× 1.2 NA water immersion objective. Imaging data were acquired using LAS X software (Leica) and FV10-ASW software (Olympus). Images taken with the Leica SP8 microscope were deconvolved using the built-in Huygens Scientific deconvolution software (<https://www.leica-microsystems.com>) operated in 2D. GFP fluorescent proteins were imaged with 488 nm excitation and 500–550 nm emission. For consistency, we selected cortical root tip cells at a height of 6–22 cells above the quiescent center in the root apical meristem for localization analysis. For cellular root parameters, 10-day-old seedlings from the differential growth decision assay were stained with modified pseudo-Schiff propidium iodide staining (Truernit et al., 2008). The excitation laser was set to 488 nm. The emission was detected at 520 nm. The junction between the meristematic and elongation zones was determined by marking the first cell in a single cortex cell file that was double the length of the previous cell (González-García et al., 2011). For seedling images, a Leica S APO stereo microscope with a Leica MC170 HD camera was used.

### Differential growth decision assay

The differential growth decision experiment was performed as described by Kalbfuß et al. (2022). In brief, seeds were surface-sterilized using a brief 80% ethanol rinse followed by 15 min incubation in sterilization buffer (0.01% SDS, 3% NaOCl). After five washes in mQ water, seeds were resuspended in 0.15% agar and stratified in the dark at 4°C for 7 days to break seed dormancy. Afterward, seeds were plated on squared plates with exactly 45 ml ½ MS medium supplemented with B5 Vitamins (Sigma-Aldrich). Culture media for TRS120 phosphomutants was additionally supplemented with 50 µg/ml kanamycin to select for transgenic seedlings. For –0.4 MPa water deficit, media plates were infused with sterile-filtrated 45 ml 2× PEG-6000 (Merck group; dissolved in liquid ½ MS media) for exactly 24 h at RT, and afterward the PEG-solution was completely decanted. Seeds were plated at the interface between the culture media and sterilized plastic strips on the media such that, upon germination, only the root touched the agar. For water stress,

seeds in each biological replicate were sown onto two plates for technical replicates, which were pooled for analysis. After plating, plates were sealed with breathable tape. Plates for dark conditions were wrapped with two layers of thick aluminum foil. All plates were incubated for 10 days at 22°C with permanent light (80 µmol m<sup>-2</sup>s<sup>-1</sup>). Note that the plates were negatively inclined by 4° to promote root growth on the media surface rather than in the agar.

After 10 days of incubation, seedlings were either used for organ length determination or for assessing cellular hypocotyl and root parameters. For organ length measurements, seedlings were transferred onto cold 1.2% agar plates, scanned at 1,200 ppi, and saved as tiff files. Hypocotyl and root lengths were analyzed with Fiji - ImageJ using the free-hand tool. The hypocotyl/root ratio was calculated as hypocotyl length divided by root length.

Root and hypocotyl responses to water deficit in the dark (abbreviated as darkW) were computed as

$$\frac{\text{organ length in the dark}}{\text{organ length under darkW}}$$

Because the hypocotyl and root have opposite responses to our additive stress conditions (hypocotyl length decreases but root length increases in response to water stress in the dark, as shown in Fig. 5) the RQs move in opposite directions.

The ratio was computed as follows:

$$\text{ratio adjustment} = \frac{\left(\frac{\text{hypocotyl}}{\text{root}}\right)_{\text{dark}}}{\left(\frac{\text{hypocotyl}}{\text{root}}\right)_{\text{darkW}}}$$

Due to variability between PEG lots and PEG plates (Kalbfuß et al., 2022), we normalized each mutant to the corresponding wild-type ecotype (see Table S2) on the same plate. Thus, the normalized ratio adjustment to water stress in the dark (darkW) was computed as follows:

$$RQ_{\text{ratio}} = \frac{\text{ratio adjustment mutant}}{\text{ratio adjustment wild type}}$$

$RQ_{\text{hypocotyl}}$  and  $RQ_{\text{root}}$  as well as light versus dark responses were computed in a similar fashion (Figs. S8, S9, and S12). These normalized organ and ratio adjustments were referred to as response quotients (RQ) to light-to-dark or dark-to-darkW conditions. The mean  $RQ_{\text{ratio}}$  of at least three biological replicates (i.e., the seed stocks from different mother plants) is shown. Please see Table S5 for thresholds for attenuated, normal, versus enhanced organ or ratio responses. For volcano plots we plotted the mean  $RQ_{\text{ratio}}$  on the X axis and the median  $P_{\text{ratio}}$  value on the Y axis. Organ and ratio adjustments for light-to-dark comparisons were computed as organ length (or ratio) in the light divided by organ length (or ratio) in the dark. *P* values were computed with the two-tailed Student's *t* test. Responses were considered to be insignificant for *P* values ≥0.05 and attenuated for *P* values ≥0.00001. The median *P* value for at least three replicates is shown in the volcano plots.

### Germination assay under osmotic stress

For germination curve experiments, surface-sterilized seeds were stratified in the dark at 4°C for 2 days. Seeds were plated on



$\frac{1}{2}$  MS media supplemented with 0.05% B5 Vitamins (Sigma-Aldrich) and either 0, 200, or 400 mM mannitol (Millipore). Approximately 100 seeds were plated per condition. Plates were incubated at 22°C under constant light conditions (80  $\mu\text{mol m}^{-2}\text{s}^{-1}$ ) and rotated every day to avoid light effects. Seed germination rates were recorded every 24 h. Seeds were scored as germinated when the radicle emerged. Data were obtained for three biological replicates, each with three technical replicates.

### Root gravitropism assay

*trsl20i* lines were selected on  $\frac{1}{2}$  MS media supplemented with 20  $\mu\text{g/ml}$  hygromycin B. Control lines were grown in parallel on media without antibiotics. After 4 days, seedlings were transferred to  $\frac{1}{2}$  MS media supplemented with 20  $\mu\text{M}$   $\beta$ -estradiol (Est; 20 mM stock dissolved in EtOH; Sigma-Aldrich) or 0.1% EtOH as mock control and grown vertically for an additional 9 days. The primary root tip angles (excluding lateral roots) were analyzed with Fiji - ImageJ. Primary roots exhibiting looping (see yellow arrow in Fig. 8 B) were scored as  $-180^\circ$  due to their growth against gravity. Primary root growth orientation was visualized as frequency plots in a polar coordinate system in R. To quantify agravitropic roots, the frequency of primary root tips growing against gravity (angles  $< -90^\circ$  and  $> 90^\circ$ ) was counted per experiment.

### Western blot analysis

Standard Western blot analysis was performed according to Sambrook et al. (1989). 7.5% SDS-PAGE gels (Mini-PROTEAN TGX gels, Bio-Rad) were blotted onto PVDF Immobilon-FL membranes (Millipore). Polyclonal rabbit anti-GFP antibody (1:2,000; A11122; Invitrogen) was used as primary antibody. As secondary antibody, we used a goat anti-rabbit Horseradish peroxidase-conjugated antibody (1:6,000; 1858415, Pierce; Thermo Fisher Scientific) together with the SuperSignal West Femto Maximum Sensitivity Substrate (Thermo Fisher Scientific). Chemiluminescence images were acquired using an ImageQuant LAS 4000 mini (GE Healthcare). To check for equal loading, blots were stained with Coomassie (10% acetic acid, 50% methanol, 0.25% Coomassie Blue R-250) and subsequently destained (10% acetic acid, 50% methanol).

### Gene ontology (GO) enrichment analysis of CLUB:GFP interactome

The CLUB:GFP interactome (Kalde et al., 2019) was used for GO term enrichment analysis. To reduce the TRAPP II interactome complexity, the GO enrichment analysis of biological processes of level 0 was done separately for high-confidence interactors (intensity ratio  $> 8$ ) and for intermediate-intensity interactors (intensity ratio  $> 5$  and  $< 8$ ) (see cutoffs Fig. 1 B). The values were computed based on a comparison between observed versus random protein occurrences for each GO term. Each term is part of the hierarchical structure of GO and has defined relationships to one or more other terms in the GO enrichment. Metabolic, transcriptional, and translational processes were excluded for simplification. Terms were grouped by manually annotated super-categories. Cutoffs for enriched GO terms were set at  $\geq 4$  for fold enrichment and  $\leq 0.003$  for the FDR-adjusted P value.

### Structural and multiple sequence alignments

AlphaFold predicted structures for *A. thaliana* AtTRS120 (UniProt: Q9FY61) and CLUB/AtTRS130 (UniProt: F4KOC4) were aligned with the *Saccharomyces cerevisiae* open formation of the TRAPP II monomer structure without substrate resolved with cryo-electron microscopy (in vitro) (PDB: 7E2C; Mi et al., 2022). The alignments were carried out with the align algorithm in PyMOL, which first performs a sequence alignment, followed by a structural superposition and then iteratively refines the alignment. The tree of the AtSK clades was created by a multiple sequence alignment with the Clustal Omega program in UniProt, using full-length protein sequences.

### Statistical analysis and image processing

Statistical analyses were performed in Microsoft Excel and RStudio. All statistical information is described in the figure legends. Data distribution was assumed to be normal, but this was not formally tested. One sample two-tailed *t* test was used to determine statistical differences when data relative to the wild-type control were computed (Fig. 4 A and Fig. S5 A). To compare two independent groups, an unpaired two-tailed Student's *t* test was used. Differences between groups across conditions were compared using two-way ANOVA (genotype  $\times$  condition) with Tukey's post hoc test in Fig. S10. Local Polynomial Regression Fitting for root cell lengths in Fig. 6, C and D was carried out with the loess method in R and reported with the 95% confidence interval. Statistical information for MS analyses is given in the LC-MS/MS analysis sections. False discovery rates, determined with the standard two-tailed *t* test, were set at a cutoff of 1%. Significance is represented as follows: \*:  $P < 0.05$ ; \*\*:  $P < 0.01$ ; \*\*\*:  $P < 0.001$ ; \*\*\*\*:  $P < 0.0001$ ; \*\*\*\*\*:  $P < 0.00001$ . Images were processed with Adobe photoshop (<https://www.adobe.com>) and GIMP (<https://www.gimp.org>) and analyzed with ImageJ (<https://imagej.nih.gov>). Graphs were created with RStudio's ggplot2 package and figures assembled with Inkscape (<https://inkscape.org>).

### Online supplemental material

Fig. S1 shows the GO term enrichment of high-confidence interactors and brassinosteroid related proteins in the CLUB:GFP interactome. Fig. S2 contains ion mass spectra of AtTRS120 phosphopeptides. Fig. S3 highlights the *Arabidopsis* family of shaggy-like kinases and AtSK peptides found in AtTRS120:GFP IP-MS. Fig. S4 shows the predicted aligned error graphs of the used AlphaFold generated AtTRS120 and CLUB/AtTRS130 protein structures. Fig. S5 contains in vitro and in vivo evidence for TRAPP II phosphorylation by AtSKs. Fig. S6 emphasizes that *bin2-1* mutants show no cytokinesis or protein sorting defects, characteristic of *trappii* mutants. Violin plots of the organ lengths or the hypocotyl/root ratio under single and additive stress in Fig. S7 enable a direct comparison between mutants and their respective wild-type control. Fig. S8 validates the attenuated hypocotyl and root phenotype of *bin2-3billbil2* and *trappii* mutants under additive stress. Fig. S9 highlights the attenuated, but highly significant etiolation phenotype of *trappii* mutants. Fig. S10 shows the cellular hypocotyl parameters of *club* mutants and a direct comparison between the wild-type and

*trappii* cellular hypocotyl parameters in an ANOVA analysis. Fig. S11 validates the expression and functionality of the TRS120 phosphovariants till the T2 generation and shows the TRS120:GFP localization in phosphomutants. Fig. S12 emphasizes the normal etiolation response in TRS120 phosphovariants. Fig. S13 contains the organ lengths and the hypocotyl/root ratio of TRS120 phosphovariants under additive stress and the total seedling lengths under the tested conditions. Table S1 shows details of the brassinosteroid related proteins found in the CLUB:GFP interactome, related to Fig. 1 C and Fig. S1 B. Table S2 lists the mutant lines used in this study. Table S3 lists the mutated sites in TRS120 phosphovariants and primer sequences used for mutagenesis. Table S4 contains the gene strand sequence carrying the TRS120 amiRNA precursor. Table S5 provides the thresholds for attenuated, normal, and enhanced response quotients. Video 1 shows a 3D projection of the cross-kingdom structural alignment of the TRAPP-II-specific TRS120 subunit.

### Data availability

The CLUB:GFP IP-MS data has previously been published (Kalde et al., 2019) and deposited to the ProteomeXchange Consortium via the PRoteomics IDentification (PRIDE) partner repository (Perez-Riverol et al., 2019). The dataset can be accessed with the identifier PXD013016. All other IP-MS or MS datasets are being deposited here for the first time. New proteomics raw data (in vitro kinase assays and in vivo evidence with AtTRS120:GFP IP-MS of bikinin and PPZ treated seedlings) including Max-Quant search results and used protein sequence databases can be accessed via Panorama Public (Sharma et al., 2014, 2018) with the following link [https://panoramaweb.org/phosphoTRAPP\\_Ara.url](https://panoramaweb.org/phosphoTRAPP_Ara.url). All other data are available in the article, together with its supplemental materials.

### Acknowledgments

We thank Prof. Wilfried Schwab, Prof. Erwin Grill, and members of their departments for support. Thanks to Prof. Arne Skerra, Martin Schlapschy, and Veder Garcia for their useful suggestions. We thank Yannik Schreckenberger, Andreas Czempel, Theo Kalmbach, Hermine Kienberger, Nina Lomp, and Franziska Hackbarth for technical assistance. We thank the WZW/TUM Centre for Advanced Light Microscopy (CALM), headed by Ramon Torres-Ruiz and Klaus Michel, for access to confocal microscopes, and Prof. Kay Schneitz for access to their Leica S APO stereo microscope. Thanks to Roman Meier at the TUMmesa facility, directed by Leonardo Teixeira and Bálint Jákli, for supporting us with optimal growth conditions for our plants. Jorge José Casal, Sean Cutler, and Ueli Grossniklaus shared published resources.

This work was supported by Deutsche Forschungsgemeinschaft DFG grants AS110/5-2, AS110/8-1, and AS110/10-1 as well as BaCa-TEC Nr. 14 [2018-2] to F.F. Assaad, by the European Research Council's Horizon 2020 Research and Innovation Programme (Grant Agreement 648420) grant to P. Falter-Braun, and by National Institutes of Health (R01GM066258 to Z.-Y. Wang). M. Abele and C. Ludwig were supported by the EU Horizon 2020 grant Epic-

XS. TUMmesa was funded with the support of the Deutsche Forschungsgemeinschaft (DFG, INST 95/1184-1 FUGG).

Author contributions: C. Wiese: methodology, investigation, visualization, writing—original draft, and writing—review & editing; M. Abele, B. Al, N. Kalbfuß, A. Strohmayer, C.H. Park, B. Brunschweiler, and C. Meng: methodology, investigation, visualization, and writing—review & editing; M. Altmann: investigation and visualization; A. Steiner: methodology, investigation, and visualization; R. Ravikumar: investigation, visualization, and writing—review & editing; E. Facher: methodology, investigation, and supervision; D.W. Ehrhardt: funding acquisition, and supervision; P. Falter-Braun: methodology, funding acquisition, supervision and writing—review & editing; Z.-Y. Wang: funding acquisition, supervision, and writing—review & editing; C. Ludwig: methodology, funding acquisition, supervision, writing—review & editing; F.F. Assaad: conceptualization, methodology, investigation, funding acquisition, project administration, supervision, writing—original draft, and writing—review & editing.

Disclosures: The authors declare no competing interests exist.

Submitted: 21 November 2023

Revised: 31 January 2024

Accepted: 15 February 2024

### References

- Altmann, M., S. Altmann, C. Falter, and P. Falter-Braun. 2018. High-quality yeast-2-hybrid interaction network mapping. *Curr. Protoc. Plant Biol.* 3: e20067. <https://doi.org/10.1002/cppb.20067>
- Asaoka, R., T. Uemura, J. Ito, M. Fujimoto, E. Ito, T. Ueda, and A. Nakano. 2013. Arabidopsis RABA1 GTPases are involved in transport between the trans-Golgi network and the plasma membrane, and are required for salinity stress tolerance. *Plant J.* 73:240–249. <https://doi.org/10.1111/tbj.12023>
- Assaad, F.F. 2001. Of weeds and men: What genomes teach us about plant cell biology. *Curr. Opin. Plant Biol.* 4:478–487. [https://doi.org/10.1016/S1369-5266\(00\)00204-1](https://doi.org/10.1016/S1369-5266(00)00204-1)
- Assaad, F.F., Y. Huet, U. Mayer, and G. Jürgens. 2001. The cytokinesis gene KEULE encodes a Sec1 protein that binds the syntaxin KNOLLE. *J. Cell Biol.* 152:531–543. <https://doi.org/10.1083/jcb.152.3.531>
- Bagde, S.R., and J.C. Fromme. 2022. Structure of a TRAPP-II-Rab11 activation intermediate reveals GTPase substrate selection mechanisms. *Sci. Adv.* 8:eabn7446. <https://doi.org/10.1126/sciadv.abn7446>
- Boutté, Y., K. Jonsson, H.E. McFarlane, E. Johnson, D. Gendre, R. Swarup, J. Friml, L. Samuels, S. Robert, and R.P. Bhalerao. 2013. ECHIDNA-mediated post-Golgi trafficking of auxin carriers for differential cell elongation. *Proc. Natl. Acad. Sci. USA.* 110:16259–16264. <https://doi.org/10.1073/pnas.1309057110>
- Brunet, S., and M. Sacher. 2014. Are all multisubunit tethering complexes bona fide tethers? *Traffic.* 15:1282–1287. <https://doi.org/10.1111/tra.12200>
- Cai, H., Y. Zhang, M. Pypaert, L. Walker, and S. Ferro-Novick. 2005. Mutants in trs120 disrupt traffic from the early endosome to the late Golgi. *J. Cell Biol.* 171:823–833. <https://doi.org/10.1083/jcb.200505145>
- Clark, N.M., T.M. Nolan, P. Wang, G. Song, C. Montes, C.T. Valentine, H. Guo, R. Sozzani, Y. Yin, and J.W. Walley. 2021. Integrated omics networks reveal the temporal signaling events of brassinosteroid response in Arabidopsis. *Nat. Commun.* 12:5858. <https://doi.org/10.1038/s41467-021-26165-3>
- Clough, S.J., and A.F. Bent. 1998. Floral dip: A simplified method for agrobacterium-mediated transformation of *Arabidopsis thaliana*. *Plant J.* 16:735–743. <https://doi.org/10.1046/j.1365-3113.1998.00343.x>
- Cox, J., M.Y. Hein, C.A. Luber, I. Paron, N. Nagaraj, and M. Mann. 2014. Accurate proteome-wide label-free quantification by delayed

- normalization and maximal peptide ratio extraction, termed MaxLFQ. *Mol. Cell. Proteomics*. 13:2513–2526. <https://doi.org/10.1074/mcp.M113.031591>
- Cox, J., and M. Mann. 2008. MaxQuant enables high peptide identification rates, individualized p.p.b.-range mass accuracies and proteome-wide protein quantification. *Nat. Biotechnol.* 26:1367–1372. <https://doi.org/10.1038/nbt.1511>
- Cox, J., N. Neuhauser, A. Michalski, R.A. Scheltema, J.V. Olsen, and M. Mann. 2011. Andromeda: A peptide search engine integrated into the MaxQuant environment. *J. Proteome Res.* 10:1794–1805. <https://doi.org/10.1021/pr101065j>
- Cox, R., S.H. Chen, E. Yoo, and N. Segev. 2007. Conservation of the TRAPP-II-specific subunits of a Ypt/Rab exchanger complex. *BMC Evol. Biol.* 7:12. <https://doi.org/10.1186/1471-2148-7-12>
- Curtis, M.D., and U. Grossniklaus. 2003. A gateway cloning vector set for high-throughput functional analysis of genes in plants. *Plant Physiol.* 133:462–469. <https://doi.org/10.1104/pp.103.027979>
- Dai, L., B. Wang, T. Wang, E.H. Meyer, V. Kettel, N. Hoffmann, H.E. McFarlane, S. Li, X. Wu, K.L. Picard, et al. 2022. The TOR complex controls ATP levels to regulate actin cytoskeleton dynamics in Arabidopsis. *Proc. Natl. Acad. Sci. USA*. 119:e2122969119. <https://doi.org/10.1073/pnas.2122969119>
- Darwin, C. 1880. *The Power of Movement in Plants*. John Murray, London.
- Dettmer, J., A. Hong-Hermesdorf, Y.-D. Stierhof, and K. Schumacher. 2006. Vacuolar H<sup>+</sup>-ATPase activity is required for endocytic and secretory trafficking in Arabidopsis. *Plant Cell*. 18:715–730. <https://doi.org/10.1105/tpc.105.037978>
- Ding, Z., C.S. Galván-Ampudia, E. Demarsy, Ł. Łangowski, J. Kleine-Vehn, Y. Fan, M.T. Morita, M. Tasaka, C. Fankhauser, R. Offringa, and J. Friml. 2011. Light-mediated polarization of the PIN3 auxin transporter for the phototropic response in Arabidopsis. *Nat. Cell Biol.* 13:447–452. <https://doi.org/10.1038/ncb2208>
- Elliott, L., I. Moore, and C. Kirchhelle. 2020. Spatio-temporal control of post-Golgi exocytic trafficking in plants. *J. Cell Sci.* 133:jcs.237065. <https://doi.org/10.1242/jcs.237065>
- Fendrych, M., L. Synek, T. Pecenková, H. Toupalová, R. Cole, E. Drdová, J. Nebesářová, M. Sedinová, M. Hála, J.E. Fowler, and V. Zársky. 2010. The Arabidopsis exocyst complex is involved in cytokinesis and cell plate maturation. *Plant Cell*. 22:3053–3065. <https://doi.org/10.1105/tpc.110.074351>
- Friml, J., J. Wiśniewska, E. Benková, K. Mendgen, and K. Palme. 2002. Lateral relocation of auxin efflux regulator PIN3 mediates tropism in Arabidopsis. *Nature*. 415:806–809. <https://doi.org/10.1038/415806a>
- Galindo, A., V.J. Planelles-Herrero, G. Degliesposti, and S. Munro. 2021. Cryo-EM structure of metazoan TRAPP-III, the multi-subunit complex that activates the GTPase Rab1. *EMBO J.* 40:e107608. <https://doi.org/10.15252/embj.2020107608>
- García, V.J., S.-L. Xu, R. Ravikumar, W. Wang, L. Elliott, E. Gonzalez, M. Fesenko, M. Altmann, B. Brunschweiler, P. Falter-Braun, et al. 2020. TRIPP is a plant-specific component of the Arabidopsis TRAPP-II membrane trafficking complex with important roles in plant development. *Plant Cell*. 32:2424–2443. <https://doi.org/10.1105/tpc.20.00044>
- Garzón, P.C., and F. Keijzer. 2011. Plants: Adaptive behavior, root-brains, and minimal cognition. *Adapt. Behav.* 19:155–171. <https://doi.org/10.1177/1059712311409446>
- Gendreau, D., K. Jonsson, Y. Boutté, and R.P. Bhalerao. 2015. Journey to the cell surface—the central role of the trans-Golgi network in plants. *Protoplasma*. 252:385–398. <https://doi.org/10.1007/s00709-014-0693-1>
- Gendreau, D., H.E. McFarlane, E. Johnson, G. Mouille, A. Sjödin, J. Oh, G. Levesque-Tremblay, Y. Watanabe, L. Samuels, and R.P. Bhalerao. 2013. Trans-Golgi network localized ECHIDNA/Ypt interacting protein complex is required for the secretion of cell wall polysaccharides in Arabidopsis. *Plant Cell*. 25:2633–2646. <https://doi.org/10.1105/tpc.113.112482>
- Gendreau, D., J. Oh, Y. Boutté, J.G. Best, L. Samuels, R. Nilsson, T. Uemura, A. Marchant, M.J. Bennett, M. Grebe, and R.P. Bhalerao. 2011. Conserved Arabidopsis ECHIDNA protein mediates trans-Golgi-network trafficking and cell elongation. *Proc. Natl. Acad. Sci. USA*. 108:8048–8053. <https://doi.org/10.1073/pnas.1018371108>
- González-García, M.-P., J. Villarrasa-Blasi, M. Zhiponova, F. Divol, S. Mora-García, E. Russinova, and A.I. Caño-Delgado. 2011. Brassinosteroids control meristem size by promoting cell cycle progression in Arabidopsis roots. *Development*. 138:849–859. <https://doi.org/10.1242/dev.057331>
- González-Guzmán, M., N. Apostolova, J.M. Bellés, J.M. Barrero, P. Piqueras, M.R. Ponce, J.L. Micol, R. Serrano, and P.L. Rodríguez. 2002. The short-chain alcohol dehydrogenase ABA2 catalyzes the conversion of xanthoxin to abscisic aldehyde. *Plant Cell*. 14:1833–1846. <https://doi.org/10.1105/tpc.002477>
- Hunter, J.D. 2007. Matplotlib: A 2D graphics environment. *Comput. Sci. Eng.* 9:90–95. <https://doi.org/10.1109/MCSE.2007.55>
- Jaber, E., K. Thiele, V. Kindziński, C. Loderer, K. Rybak, G. Jürgens, U. Mayer, R. Söllner, G. Wanner, and F.F. Assaad. 2010. A putative TRAPP-II tethering factor is required for cell plate assembly during cytokinesis in Arabidopsis. *New Phytol.* 187:751–763. <https://doi.org/10.1111/j.1469-8137.2010.03331.x>
- Jiménez, J.L., B. Hegemann, J.R.A. Hutchins, J.-M. Peters, and R. Durbin. 2007. A systematic comparative and structural analysis of protein phosphorylation sites based on the mtcPTM database. *Genome Biol.* 8:R90. <https://doi.org/10.1186/gb-2007-8-5-r90>
- Jumper, J., R. Evans, A. Pritzel, T. Green, M. Figurnov, O. Ronneberger, K. Tunyasuvunakool, R. Bates, A. Židek, A. Potapenko, et al. 2021. Highly accurate protein structure prediction with AlphaFold. *Nature*. 596:583–589. <https://doi.org/10.1038/s41586-021-03819-2>
- Kalbfuß, N., A. Strohmayr, M. Kegel, L. Le, F. Grosse-Holz, B. Brunschweiler, K. Stöckl, C. Wiese, C. Franke, C. Schiestl, et al. 2022. A role for brassinosteroid signalling in decision-making processes in the Arabidopsis seedling. *PLoS Genet.* 18:e1010541. <https://doi.org/10.1371/journal.pgen.1010541>
- Kalder, M., L. Elliott, R. Ravikumar, K. Rybak, M. Altmann, S. Klaeger, C. Wiese, M. Abele, B. Al, N. Kalbfuß, et al. 2019. Interactions between transport protein Particle (TRAPP) complexes and Rab GTPases in Arabidopsis. *Plant J.* 100:279–297. <https://doi.org/10.1111/tjp.14442>
- Karban, R., and J.L. Orrock. 2018. A judgment and decision-making model for plant behavior. *Ecology*. 99:1909–1919. <https://doi.org/10.1002/ecy.2418>
- Kim, J.J., Z. Lipatova, and N. Segev. 2016. TRAPP complexes in secretion and autophagy. *Front. Cell Dev. Biol.* 4:20. <https://doi.org/10.3389/fcell.2016.00020>
- Kim, S.-J., and D.C. Bassham. 2011. TNO1 is involved in salt tolerance and vacuolar trafficking in Arabidopsis. *Plant Physiol.* 156:514–526. <https://doi.org/10.1104/pp.110.168963>
- Kim, T.-W., M. Michniewicz, D.C. Bergmann, and Z.-Y. Wang. 2012. Brassinosteroid regulates stomatal development by GSK3-mediated inhibition of a MAPK pathway. *Nature*. 482:419–422. <https://doi.org/10.1038/nature10794>
- Kim, T.-W., C.H. Park, C.-C. Hsu, Y.-W. Kim, Y.-W. Ko, Z. Zhang, J.-Y. Zhu, Y.-C. Hsiao, T. Branon, K. Kaasik, et al. 2023. Mapping the signaling network of BIN2 kinase using TurboID-mediated biotin labeling and phosphoproteomics. *Plant Cell*. 35:975–993. <https://doi.org/10.1093/plcell/koad013>
- Konstantinova, N., B. Korbei, and C. Luschnig. 2021. Auxin and root gravitropism: Addressing basic cellular processes by exploiting a defined growth response. *Int. J. Mol. Sci.* 22:2749. <https://doi.org/10.3390/ijms22052749>
- Lee, C.-F., H.-Y. Pu, L.-C. Wang, R.J. Sayler, C.-H. Yeh, and S.-J. Wu. 2006. Mutation in a homolog of yeast Vps53p accounts for the heat and osmotic hypersensitive phenotypes in Arabidopsis hit1-1 mutant. *Planta*. 224:330–338. <https://doi.org/10.1007/s00425-005-0216-6>
- Li, C., B. Zhang, and H. Yu. 2021. GSK3s: Nodes of multilayer regulation of plant development and stress responses. *Trends Plant Sci.* 26:1286–1300. <https://doi.org/10.1016/j.tplants.2021.07.017>
- Li, J., and K.H. Nam. 2002. Regulation of brassinosteroid signaling by a GSK3/SHAGGY-like kinase. *Science*. 295:1299–1301. <https://doi.org/10.1126/science.1065769>
- Li, J., K.H. Nam, D. Vafeados, and J. Chory. 2001. BIN2, a new brassinosteroid-insensitive locus in Arabidopsis. *Plant Physiol.* 127:14–22. <https://doi.org/10.1104/pp.127.1.14>
- Liu, L., L. Qin, L.B. Safdar, C. Zhao, X. Cheng, M. Xie, Y. Zhang, F. Gao, Z. Bai, J. Huang, et al. 2023. The plant trans-Golgi network component ECHIDNA regulates defense, cell death, and endoplasmic reticulum stress. *Plant Physiol.* 191:558–574. <https://doi.org/10.1093/plphys/kiac400>
- Lv, M., and J. Li. 2020. Molecular mechanisms of brassinosteroid-mediated responses to changing environments in Arabidopsis. *Int. J. Mol. Sci.* 21:2737. <https://doi.org/10.3390/ijms21082737>
- Ma, Y., I. Szostkiewicz, A. Korte, D. Moes, Y. Yang, A. Christmann, and E. Grill. 2009. Regulators of PP2C phosphatase activity function as abscisic acid sensors. *Science*. 324:1064–1068. <https://doi.org/10.1126/science.1172408>
- MacLean, B., D.M. Tomazela, N. Shulman, M. Chambers, G.L. Finney, B. Frewen, R. Kern, D.L. Tabb, D.C. Liebler, and M.J. MacCoss. 2010.

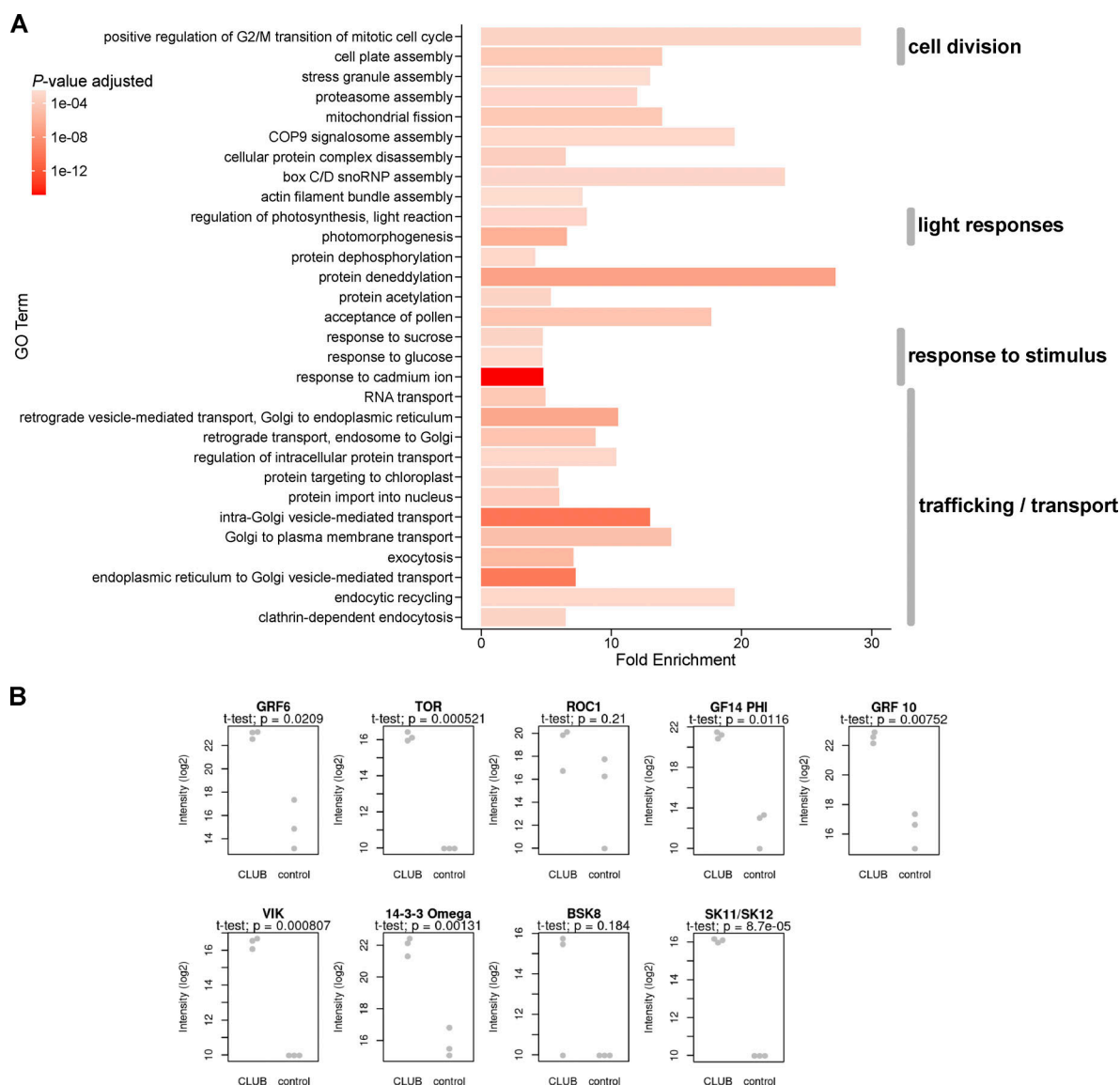


- Skyline: An open source document editor for creating and analyzing targeted proteomics experiments. *Bioinformatics*. 26:966–968. <https://doi.org/10.1093/bioinformatics/btq054>
- Mazzella, M.A., and J.J. Casal. 2001. Interactive signalling by phytochromes and cryptochromes generates de-etiolation homeostasis in *Arabidopsis thaliana*. *Plant Cell Environ.* 24:155–161. <https://doi.org/10.1111/j.1365-3040.2001.00653.x>
- McClung, C.R. 2006. Plant circadian rhythms. *Plant Cell*. 18:792–803. <https://doi.org/10.1105/tpc.106.040980>
- McFarlane, H.E., Y. Watanabe, D. Gendre, K. Carruthers, G. Levesque-Tremblay, G.W. Haughn, R.P. Bhalarao, and L. Samuels. 2013. Cell wall polysaccharides are mislocalized to the Vacuole in echidna mutants. *Plant Cell Physiol.* 54:1867–1880. <https://doi.org/10.1093/pcp/pct129>
- McKinney, W. 2010. Data structures for statistical computing in python. *Proc. 9th Python Sci. Conf.* 445:56–61. <https://doi.org/10.25080/majora-92bf1922-00a>
- Mi, C., L. Zhang, G. Huang, G. Shao, F. Yang, X. You, M.-Q. Dong, S. Sun, and S.-F. Sui. 2022. Structural basis for assembly of TRAPP II complex and specific activation of GTPase Ypt31/32. *Sci. Adv.* 8:eabi5603. <https://doi.org/10.1126/sciadv.abi5603>
- Morozova, N., Y. Liang, A.A. Tokarev, S.H. Chen, R. Cox, J. Andrejic, Z. Lipatova, V.A. Sciorra, S.D. Emr, and N. Segev. 2006. TRAPP II subunits are required for the specificity switch of a Ypt-Rab GEF. *Nat. Cell Biol.* 8:1263–1269. <https://doi.org/10.1038/ncb1489>
- Naramoto, S., T. Nodzyński, T. Dainobu, H. Takatsuka, T. Okada, J. Friml, and H. Fukuda. 2014. VAN4 encodes a putative TRS120 that is required for normal cell growth and vein development in *Arabidopsis*. *Plant Cell Physiol.* 55:750–763. <https://doi.org/10.1093/pcp/pcu012>
- Park, S.-Y., P. Fung, N. Nishimura, D.R. Jensen, H. Fujii, Y. Zhao, S. Lumba, J. Santiago, A. Rodrigues, T.F. Chow, et al. 2009. Absciscic acid inhibits type 2C protein phosphatases via the PYR/PYL family of START proteins. *Science*. 324:1068–1071. <https://doi.org/10.1126/science.1173041>
- Perez-Riverol, Y., A. Csordas, J. Bai, M. Bernal-Llinares, S. Hewapathirana, D.J. Kundu, A. Inuganti, J. Griss, G. Mayer, M. Eisenacher, et al. 2019. The PRIDE database and related tools and resources in 2019: Improving support for quantification data. *Nucleic Acids Res.* 47:D442–D450. <https://doi.org/10.1093/nar/gky1106>
- Pinar, M., E. Arias-Palomo, V. de los Ríos, H.N.J. Arst Jr., and M.A. Peñalva. 2019. Characterization of *Aspergillus nidulans* TRAPPs uncovers unprecedented similarities between fungi and metazoans and reveals the modular assembly of TRAPP II. *PLoS Genet.* 15:e1008557. <https://doi.org/10.1371/journal.pgen.1008557>
- Pinar, M., H.N. Arst Jr., A. Pantazopoulou, V.G. Tagua, V. de los Ríos, J. Rodríguez-Salichs, J.F. Díaz, and M.A. Peñalva. 2015. TRAPP II regulates exocytic Golgi exit by mediating nucleotide exchange on the Ypt31 ortholog RabERAB11. *Proc. Natl. Acad. Sci. USA*. 112:4346–4351. <https://doi.org/10.1073/pnas.1419168112>
- Pinar, M., and M.A. Peñalva. 2020. En bloc TGN recruitment of *Aspergillus* TRAPP II reveals TRAPP maturation as unlikely to drive RAB1-to-RAB11 transition. *J. Cell Sci.* 133:jcs241141. <https://doi.org/10.1242/jcs.241141>
- Planas-Riverola, A., A. Gupta, I. Betegón-Putze, N. Bosch, M. Ibañez, and A.I. Caño-Delgado. 2019. Brassinosteroid signaling in plant development and adaptation to stress. *Development*. 146:dev151894. <https://doi.org/10.1242/dev.151894>
- Pusch, S., H. Harashima, and A. Schnittger. 2012. Identification of kinase substrates by bimolecular complementation assays. *Plant J.* 70:348–356. <https://doi.org/10.1111/j.1365-313X.2011.04862.x>
- Qi, X., M. Kaneda, J. Chen, A. Geitmann, and H. Zheng. 2011. A specific role for *Arabidopsis* TRAPP II in post-Golgi trafficking that is crucial for cytokinesis and cell polarity. *Plant J.* 68:234–248. <https://doi.org/10.1111/j.1365-313X.2011.04681.x>
- Qi, X., and H. Zheng. 2011. *Arabidopsis* TRAPP II is functionally linked to Rab-A, but not Rab-D in polar protein trafficking in trans-Golgi network. *Plant Signal. Behav.* 6:1679–1683. <https://doi.org/10.4161/psb.6.11.17915>
- Ravikumar, R., N. Kalbfuß, D. Gendre, A. Steiner, M. Altmann, S. Altmann, K. Rybak, H. Edelmann, F. Stephan, M. Lampe, et al. 2018. Independent yet overlapping pathways ensure the robustness and responsiveness of trans-Golgi network functions in *Arabidopsis*. *Development*. 145:dev169201. <https://doi.org/10.1242/dev.169201>
- Ravikumar, R., A. Steiner, and F.F. Assaad. 2017. Multisubunit tethering complexes in higher plants. *Curr. Opin. Plant Biol.* 40:97–105. <https://doi.org/10.1016/j.pbi.2017.08.009>
- Riedel, F., A. Galindo, N. Muschalik, and S. Munro. 2018. The two TRAPP complexes of metazoans have distinct roles and act on different Rab GTPases. *J. Cell Biol.* 217:601–617. <https://doi.org/10.1083/jcb.201705068>
- Rosquete, M.R., and G. Drakakaki. 2018. Plant TGN in the stress response: A compartmentalized overview. *Curr. Opin. Plant Biol.* 46:122–129. <https://doi.org/10.1016/j.pbi.2018.09.003>
- Rosquete, M.R., N. Worden, G. Ren, R.M. Sinclair, S. Pfleger, M. Salemi, B.S. Phinney, D. Domozych, T. Wilkop, and G. Drakakaki. 2019. At-TRAPP11/ROG2: A role for TRAPPs in maintenance of the plant trans-Golgi network/early endosome organization and function. *Plant Cell*. 31:1879–1898. <https://doi.org/10.1105/tpc.19.00110>
- Rubio, S., A. Rodrigues, A. Saez, M.B. Dizon, A. Galle, T.-H. Kim, J. Santiago, J. Flexas, J.I. Schroeder, and P.L. Rodriguez. 2009. Triple loss of function of protein phosphatases type 2C leads to partial constitutive response to endogenous abscisic acid. *Plant Physiol.* 150:1345–1355. <https://doi.org/10.1104/pp.109.137174>
- Rybak, K., A. Steiner, L. Synek, S. Klaeger, I. Kulich, E. Facher, G. Wanner, B. Kuster, V. Zarsky, S. Persson, and F.F. Assaad. 2014. Plant cytokinesis is orchestrated by the sequential action of the TRAPP II and exocyst tethering complexes. *Dev. Cell*. 29:607–620. <https://doi.org/10.1016/j.devcel.2014.04.029>
- Sambrook, J., E.F. Fritsch, and T. Maniatis. 1989. *Molecular Cloning: A Laboratory Manual*. Cold Spring Harbor Laboratory Press, Cold Spring Harbor, NY, USA.
- Schwab, R., S. Ossowski, M. Riester, N. Warthmann, and D. Weigel. 2006. Highly specific gene silencing by artificial microRNAs in *Arabidopsis*. *Plant Cell*. 18:1121–1133. <https://doi.org/10.1105/tpc.105.039834>
- Schwanhäusser, B., D. Busse, N. Li, G. Dittmar, J. Schuchhardt, J. Wolf, W. Chen, and M. Selbach. 2011. Global quantification of mammalian gene expression control. *Nature*. 473:337–342. <https://doi.org/10.1038/nature10098>
- Seki, M., P. Carninci, Y. Nishiyama, Y. Hayashizaki, and K. Shinozaki. 1998. High-efficiency cloning of *Arabidopsis* full-length cDNA by biotinylated CAP trapper. *Plant J.* 15:707–720. <https://doi.org/10.1046/j.1365-313x.1998.00237.x>
- Seki, M., M. Narusaka, A. Kamiya, J. Ishida, M. Satou, T. Sakurai, M. Nakajima, A. Enju, K. Akiyama, Y. Oono, et al. 2002. Functional annotation of a full-length *Arabidopsis* cDNA collection. *Science*. 296:141–145. <https://doi.org/10.1126/science.1071006>
- Severino, L.S. 2021. Plants make smart decisions in complex environments. *Plant Signal. Behav.* 16:1970448. <https://doi.org/10.1080/15592324.2021.1970448>
- Sharma, V., J. Eckels, B. Schilling, C. Ludwig, J.D. Jaffe, M.J. MacCoss, and B. MacLean. 2018. Panorama public: A public repository for quantitative data sets processed in skyline. *Mol. Cell. Proteomics*. 17:1239–1244. <https://doi.org/10.1074/mcp.RA117.000543>
- Sharma, V., J. Eckels, G.K. Taylor, N.J. Shulman, A.B. Stergachis, S.A. Joyner, P. Yan, J.R. Whiteaker, G.N. Halusa, B. Schilling, et al. 2014. Panorama: A targeted proteomics knowledge base. *J. Proteome Res.* 13:4205–4210. <https://doi.org/10.1021/pr5006636>
- Shevchenko, A., H. Tomas, J. Havlis, J.V. Olsen, and M. Mann. 2006. In-gel digestion for mass spectrometric characterization of proteins and proteomes. *Nat. Protoc.* 1:2856–2860. <https://doi.org/10.1038/nprot.2006.468>
- Söllner, R., G. Glässer, G. Wanner, C.R. Somerville, G. Jürgens, and F.F. Assaad. 2002. Cytokinesis-defective mutants of *Arabidopsis*. *Plant Physiol.* 129:678–690. <https://doi.org/10.1104/pp.004184>
- Song, Y., Y. Wang, Q. Yu, Y. Sun, J. Zhang, J. Zhan, and M. Ren. 2023. Regulatory network of GSK3-like kinases and their role in plant stress response. *Front. Plant Sci.* 14:1123436. <https://doi.org/10.3389/fpls.2023.1123436>
- Steiner, A., K. Rybak, M. Altmann, H.E. McFarlane, S. Klaeger, N. Nguyen, E. Facher, A. Ivakov, G. Wanner, B. Kuster, et al. 2016. Cell cycle-regulated PLEIAD/AtMAP65-3 links membrane and microtubule dynamics during plant cytokinesis. *Plant J.* 88:531–541. <https://doi.org/10.1111/tpj.13275>
- Steiner, A., L. Müller, K. Rybak, V. Vodermaier, E. Facher, M. Thellmann, R. Ravikumar, G. Wanner, M.-T. Hauser, and F.F. Assaad. 2016b. The membrane-associated Sec1/Munc18 KEULE is required for phragmoplast microtubule reorganization during cytokinesis in *Arabidopsis*. *Mol. Plant*. 9:528–540. <https://doi.org/10.1016/j.molp.2015.12.005>
- Swarbreck, D., C. Wilks, P. Lamesch, T.Z. Berardini, M. Garcia-Hernandez, H. Foerster, D. Li, T. Meyer, R. Muller, L. Ploetz, et al. 2008. The *Arabidopsis* information resource (TAIR): Gene structure and function annotation. *Nucleic Acids Res.* 36:D1009–D1014. <https://doi.org/10.1093/nar/gkm965>
- Tang, W., M. Yuan, R. Wang, Y. Yang, C. Wang, J.A. Osés-Prieto, T.-W. Kim, H.-W. Zhou, Z. Deng, S.S. Gampala, et al. 2011. PP2A activates brassinosteroid-responsive gene expression and plant growth by dephosphorylating BZR1. *Nat. Cell Biol.* 13:124–131. <https://doi.org/10.1038/ncb2151>



- Thellmann, M., K. Rybak, K. Thiele, G. Wanner, and F.F. Assaad. 2010. Tethering factors required for cytokinesis in Arabidopsis. *Plant Physiol.* 154:720–732. <https://doi.org/10.1104/pp.110.154286>
- Thomas, L.L., and J.C. Fromme. 2016. GTPase cross talk regulates TRAPP1 activation of Rab11 homologues during vesicle biogenesis. *J. Cell Biol.* 215:499–513. <https://doi.org/10.1083/jcb.201608123>
- Truernit, E., H. Bauby, B. Dubreucq, O. Grandjean, J. Runions, J. Barthélémy, and J.-C. Palauqui. 2008. High-resolution whole-mount imaging of three-dimensional tissue organization and gene expression enables the study of Phloem development and structure in Arabidopsis. *Plant Cell.* 20:1494–1503. <https://doi.org/10.1105/tpc.107.056069>
- Tyanova, S., T. Temu, and J. Cox. 2016a. The MaxQuant computational platform for mass spectrometry-based shotgun proteomics. *Nat. Protoc.* 11:2301–2319. <https://doi.org/10.1038/nprot.2016.136>
- Tyanova, S., T. Temu, P. Sinitcyn, A. Carlson, M.Y. Hein, T. Geiger, M. Mann, and J. Cox. 2016b. The Perseus computational platform for comprehensive analysis of (prote)omics data. *Nat. Methods.* 13:731–740. <https://doi.org/10.1038/nmeth.3901>
- Uemura, T. 2016. Physiological roles of plant post-golgi transport pathways in membrane trafficking. *Plant Cell Physiol.* 57:2013–2019. <https://doi.org/10.1093/pcp/pcw149>
- Uemura, T., T. Ueda, and A. Nakano. 2012. The physiological role of SYP4 in the salinity and osmotic stress tolerances. *Plant Signal. Behav.* 7: 1118–1120. <https://doi.org/10.4161/psb.21307>
- Varadi, M., S. Anyango, M. Deshpande, S. Nair, C. Natassia, G. Yordanova, D. Yuan, O. Stroe, G. Wood, A. Laydon, et al. 2022. AlphaFold protein structure database: Massively expanding the structural coverage of protein-sequence space with high-accuracy models. *Nucleic Acids Res.* 50:D439–D444. <https://doi.org/10.1093/nar/gkab1061>
- Vert, G., and J. Chory. 2006. Downstream nuclear events in brassinosteroid signalling. *Nature.* 441:96–100. <https://doi.org/10.1038/nature04681>
- Wang, L.-C., M.-C. Tsai, K.-Y. Chang, Y.-S. Fan, C.-H. Yeh, and S.-J. Wu. 2011. Involvement of the Arabidopsis HIT1/AtVPS53 tethering protein homologue in the acclimation of the plasma membrane to heat stress. *J. Exp. Bot.* 62:3609–3620. <https://doi.org/10.1093/jxb/err060>
- Waskom, M.L. 2021. Seaborn: Statistical data visualization. *J. Open Source Softw.* 6:3021. <https://doi.org/10.21105/joss.03021>
- Yan, Z., J. Zhao, P. Peng, R.K. Chihara, and J. Li. 2009. BIN2 functions redundantly with other Arabidopsis GSK3-like kinases to regulate brassinosteroid signaling. *Plant Physiol.* 150:710–721. <https://doi.org/10.1104/pp.109.138099>
- Youn, J.-H., and T.-W. Kim. 2015. Functional insights of plant GSK3-like kinases: Multi-taskers in diverse cellular signal transduction pathways. *Mol. Plant.* 8:552–565. <https://doi.org/10.1016/j.molp.2014.12.006>
- Zhao, R., N. Li, Q. Lin, M. Li, X. Shen, Y. Peng, Y. Du, Q. Ning, Y. Li, J. Zhan, et al. 2023. ZmBET5L1 inhibits primary root growth and decreases osmotic stress tolerance by mediating vesicle aggregation and tethering in maize. *Plant Cell Environ.* 46:975–990. <https://doi.org/10.1111/pce.14517>
- Zhu, J., Z. Gong, C. Zhang, C.-P. Song, B. Damsz, G. Inan, H. Koiwa, J.-K. Zhu, P.M. Hasegawa, and R.A. Bressan. 2002. OSM1/SYP61: A syntaxin protein in Arabidopsis controls abscisic acid-mediated and non-abscisic acid-mediated responses to abiotic stress. *Plant Cell.* 14:3009–3028. <https://doi.org/10.1105/tpc.006981>

## Supplemental material



**Figure S1. GO term enrichment and selected brassinosteroid signaling components in IP-MS with the TRAPP11-specific CLUB:GFP subunit as bait.** Light-grown inflorescences were used (see Fig. 1, B and C; Kalde et al., 2019). As control, the soluble GFP empty vector was used. Three replicates were carried out for the IP-MS experiments. **(A)** Gene ontology (GO) term enrichment analysis of the TRAPP11 interactome. Depicted are highly abundant (fold enrichment  $\geq 4$ ) and significant (FDR-adjusted P value  $\leq 0.003$ ) GO term associations of biological processes of level 0. The length of each bar corresponds to the fold enrichment of GO terms associated with detected proteins, while the color intensity indicates the significance given as the P value adjusted for the false discovery rate (FDR). The GO term enrichment analysis was carried out with high-confidence interactors (intensity ratio  $> 8$  and P value  $\leq 0.02$ ; see Fig. 1 B). Note that the majority of GO terms are associated with trafficking and transport (12/30). GO terms associated with response to stimulus, light responses, and cell division were also enriched. **(B)** Individual intensity-based absolute quantification (iBAQ) values in  $\log_2$  scale of brassinosteroid-related proteins (highlighted in Fig. 1 C) found in each CLUB:GFP IP-MS replicate. Selected brassinosteroid-related proteins were differentially enriched over light- versus dark-grown seedlings in a different IP-MS experiment. Dots clustered at the bottom of the graphs represent peptides that were not detected (or detected as very low intensity) in the sample. P values were obtained using the Welch's t test. Related to Fig. 1, and Table S1.

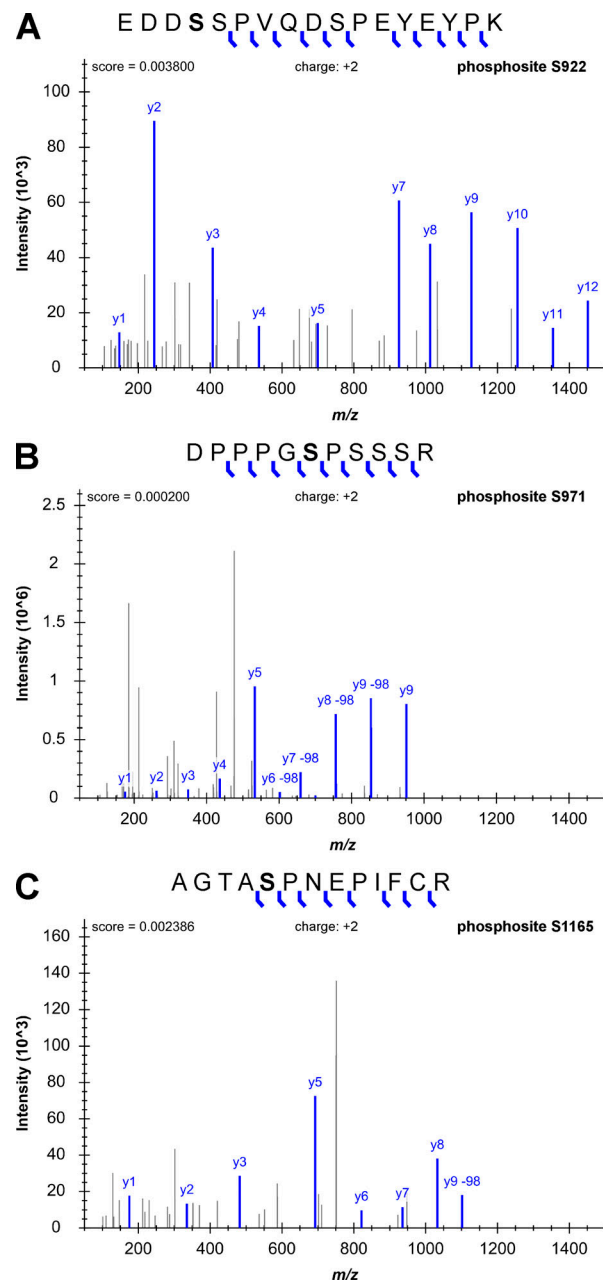


Figure S2. **Fragment ion mass spectra of AtTRS120 phosphopeptides found in AtTRS120:GFP IP-MS.** Seedlings were grown in the light. **(A)**  $\alpha$ -phosphosite of AtTRS120 at amino acid position S922. The spectrum with the phosphorylated S922 residue was identified with a 1% FDR, as can be seen in the deposited Skyline library. Note that the depicted y-ion series does not show the phosphorylation at S922. **(B)**  $\beta$ -phosphosite of AtTRS120 at amino acid position S971. **(C)**  $\gamma$ -phosphosite of AtTRS120 at amino acid position S1165. The y-ion series is highlighted in blue and non-annotated fragment ions in gray. Phosphorylated serines are written in bold letters. These sites are annotated as GSK3 sites in the PPSP (<https://www.phosphosite.org>) database. Note that not all phosphosites we detected in vivo (highlighted in yellow in Fig. 2 C) are depicted here. Spectra are taken from the deposited Skyline library, resulting from a MaxQuant search. At least three replicates were carried out for the IP-MS experiments. Related to Fig. 2.

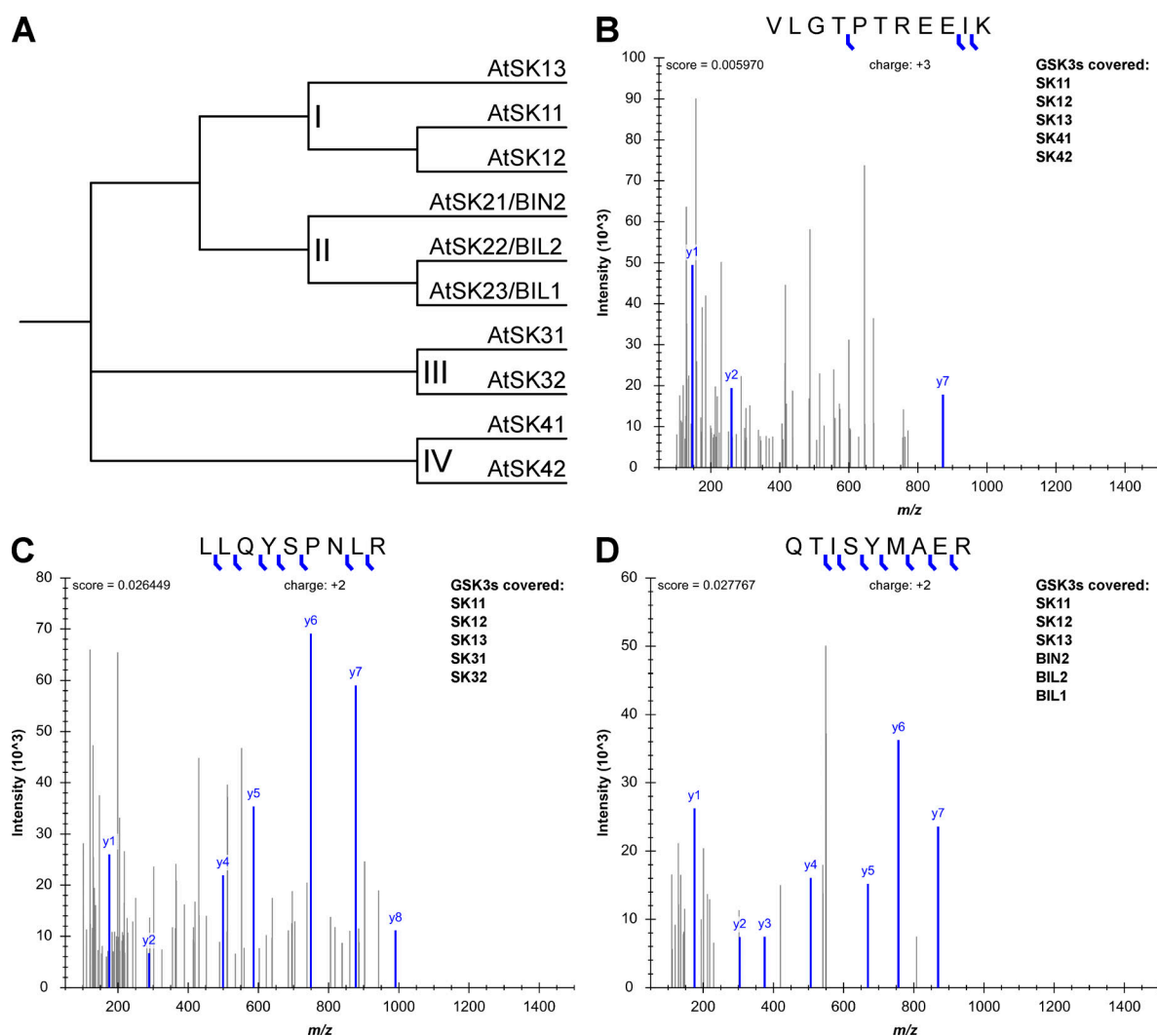


Figure S3. **Fragment ion mass spectra of AtSK/GSK3 kinases found in AtTRS120:GFP IP-MS.** The AtSK/GSK3 kinase family in *Arabidopsis* consists of 10 isoforms. Therefore, mass-spectrometric evidence of different peptides can account for the presence of different kinases in a coimmunoprecipitation with light-grown TRS120:GFP seedlings as bait. The y-ion series is highlighted in blue and non-annotated fragment ions in gray. **(A)** The *Arabidopsis* genome encodes ten shaggy-like kinases, which are classified into four clades. Multiple sequence alignment in UniProt using full-length protein sequences. **(B)** VLGTPTREEIK is shared by AtSKs in clades I and IV. **(C)** LLQYSPNLR is shared by AtSKs in clades I and III. **(D)** QTISYMAER is shared by AtSKs in clades I and II. Spectra are taken from the deposited Skyline library, resulting from a MaxQuant search. At least three replicates were carried out for the IP-MS experiments. Related to Fig. 2.



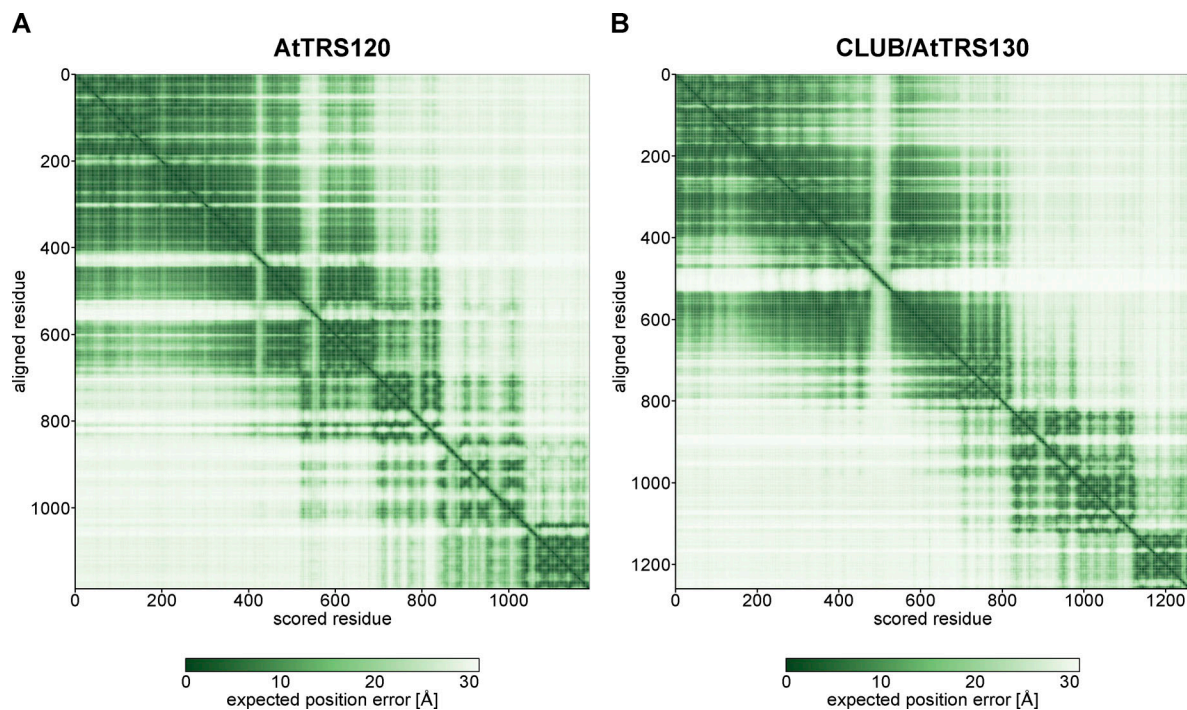
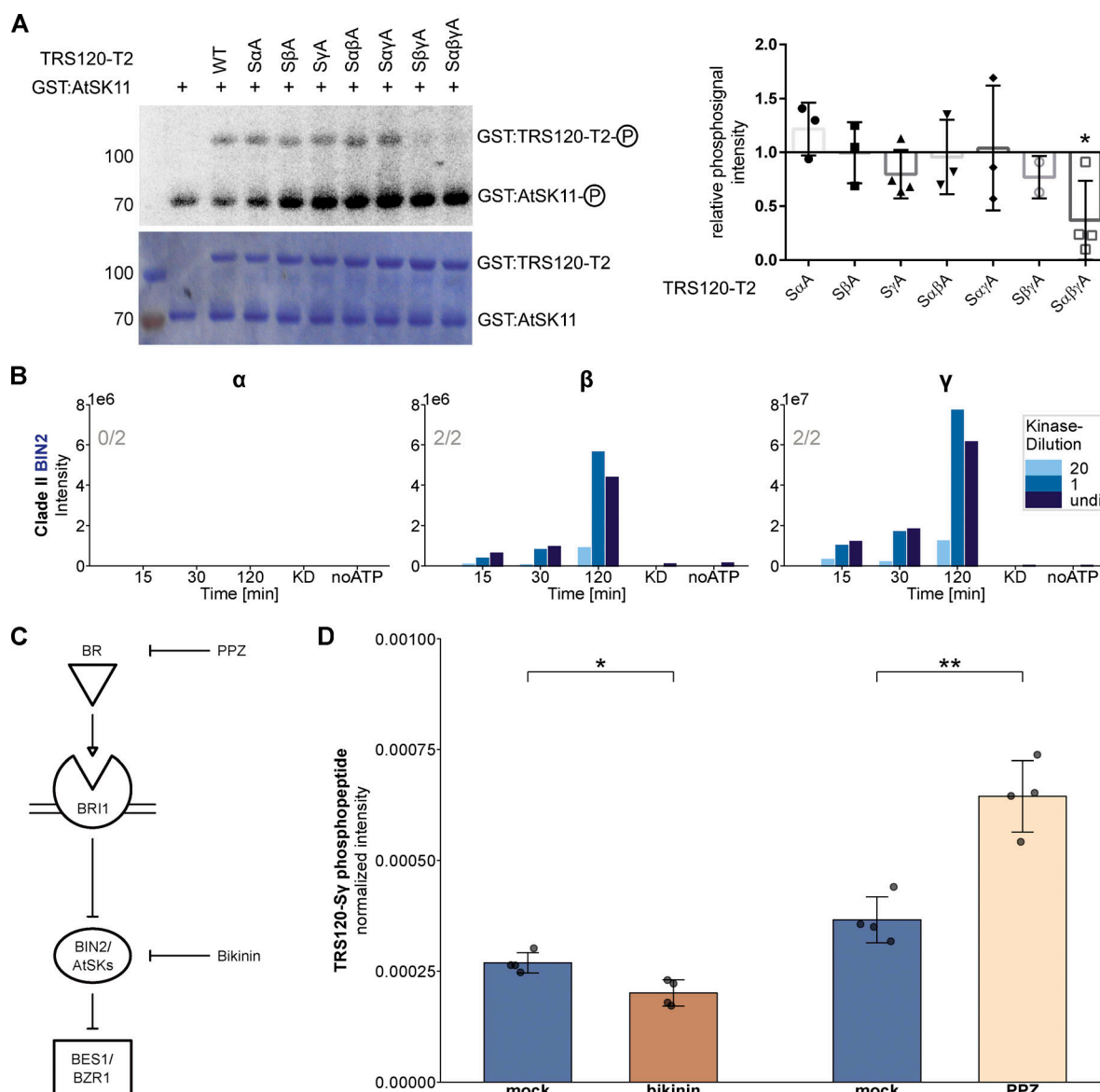


Figure S4. **Predicted aligned error graphs of the AlphaFold generated AtTRS120 and CLUB/AtTRS130 protein structures. (A and B)** Predicted aligned error (PAE) graphs of the AlphaFold predictions (Jumper et al., 2021; Varadi et al., 2022) of *A. thaliana* (At) (A) AtTRS120 and (B) CLUB/AtTRS130 are shown for assessing the domain prediction confidence. The heatmaps are colored based on the expected positional error (given in Ångström) at residue x if the predicted and true structures are aligned on residue y. Related to Figs. 2 and 3; and Video 1.



**Figure S5. In vitro and in vivo evidence for TRAPP II phosphorylation by AtSKs. (A)** In vitro kinase assays using GST:AtSK11 (72 kDa) and GST:TRS120-T2 (100 kDa). The change of phosphosignal is shown in a representative autoradiograph (upper panel) and the loaded protein amount in the corresponding CBB (Coomassie stain, lower panel). Non-phosphorylatable S to A TRS120-T2 variants were used as negative controls. The means  $\pm$  SD of phosphosignals were normalized to the protein amount and related to non-mutated TRS120-T2 wild-type control. Note that AtSK11 phosphorylated AtTRS120-T2 in vitro, with a preference for wild-type (WT) sequences over non-phosphorylatable AtTRS120-SαβγA.  $n = 2-4$  independent experiments; \*:  $P < 0.05$  for significant differences to TRS120-T2 WT (set at 1.0 right panel) determined by using a one sample two-tailed  $t$  test. **(B)** In vitro kinase assay with mass-spectrometry readout using BIN2 as kinase and TRS120-T2 truncation as substrate. Dilution series of the kinase are depicted in different shades of blue. BIN2 phosphorylated the  $\beta$  and  $\gamma$  site of TRS120 with a preference for the  $\gamma$  site ( $1e7$  for TRS120- $\gamma$  versus  $1e6$  for TRS120- $\beta$  on the Y axis). Samples incubated for 120 min in a kinase buffer without ATP, or samples in which the kinase was heat-inactivated (KD), served as negative controls. The numbers in gray in each plot denote the number of times the phosphorylation event was seen in the given number of independent replicates. **(C)** Bikinin is an inhibitor of shaggy-like kinases (AtSKs), whereas PPZ is a BR biosynthesis inhibitor that relieves BR-mediated BIN2 inhibition. **(D)** Impact of the pharmacological inhibitors bikinin and PPZ on the TRS120 phosphorylation status in vivo. IP-MS was carried out on light-grown TRS120:GFP seedlings treated with bikinin, PPZ, or the respective mock-controls. The phosphorylated peptides were further analyzed via Skyline (MacLean et al., 2010). Normalized intensities were calculated as the ratio of the TRS120-Sy phosphopeptide intensity over the sum of all TRS120 peptide intensities found in the respective experiment. The extent of phosphorylation at the TRS120- $\gamma$  site was significantly decreased by bikinin. In contrast, PPZ treatment increased the phosphorylation of the TRS120-Sy peptide in vivo. P values were computed with a two-tailed Student's  $t$  test (\*:  $P < 0.05$ ; \*\*:  $P < 0.01$ ). Mean  $\pm$  SD of four replicates are shown for the control and treatment. Related to Figs. 2, 3, and 4. Source data are available for this figure: SourceData FS5.

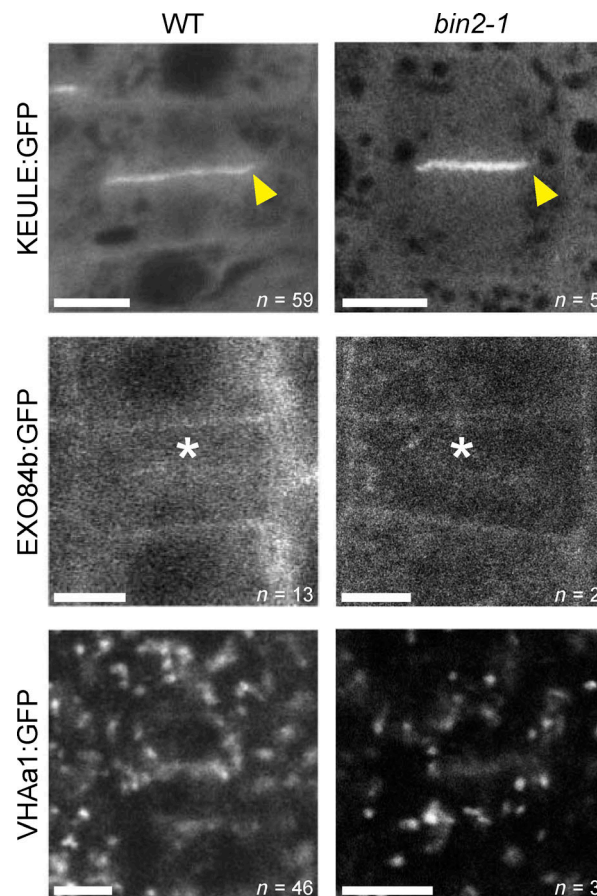


Figure S6. **Cytokinesis and protein sorting in *bin2-1*.** Localization patterns of diverse markers in root tip cells of light-grown seedlings. Confocal Scanning Laser Microscopy. A protein that resides at the cell plate during cytokinesis in the wild type,  $P_{KEU}::KEULE:GFP$  (Steiner et al., 2016b) was also seen at the cell plate in *bin2-1* mutants (yellow arrowhead). Conversely, markers that are largely excluded from the cell plate (white star) in the wild type ( $P_{EXO84b}::EXO84b:GFP$  [Fendrych et al., 2010],  $P_{VHAA1}::VHAA1:GFP$  [Dettmer et al., 2006]) are also excluded in *bin2-1* mutants. Cell plate formation and morphology in *bin2-1* also did not visibly differ from the wild type. Sample numbers  $n$  = number of imaged cells. Scale bars represent 5  $\mu m$ .

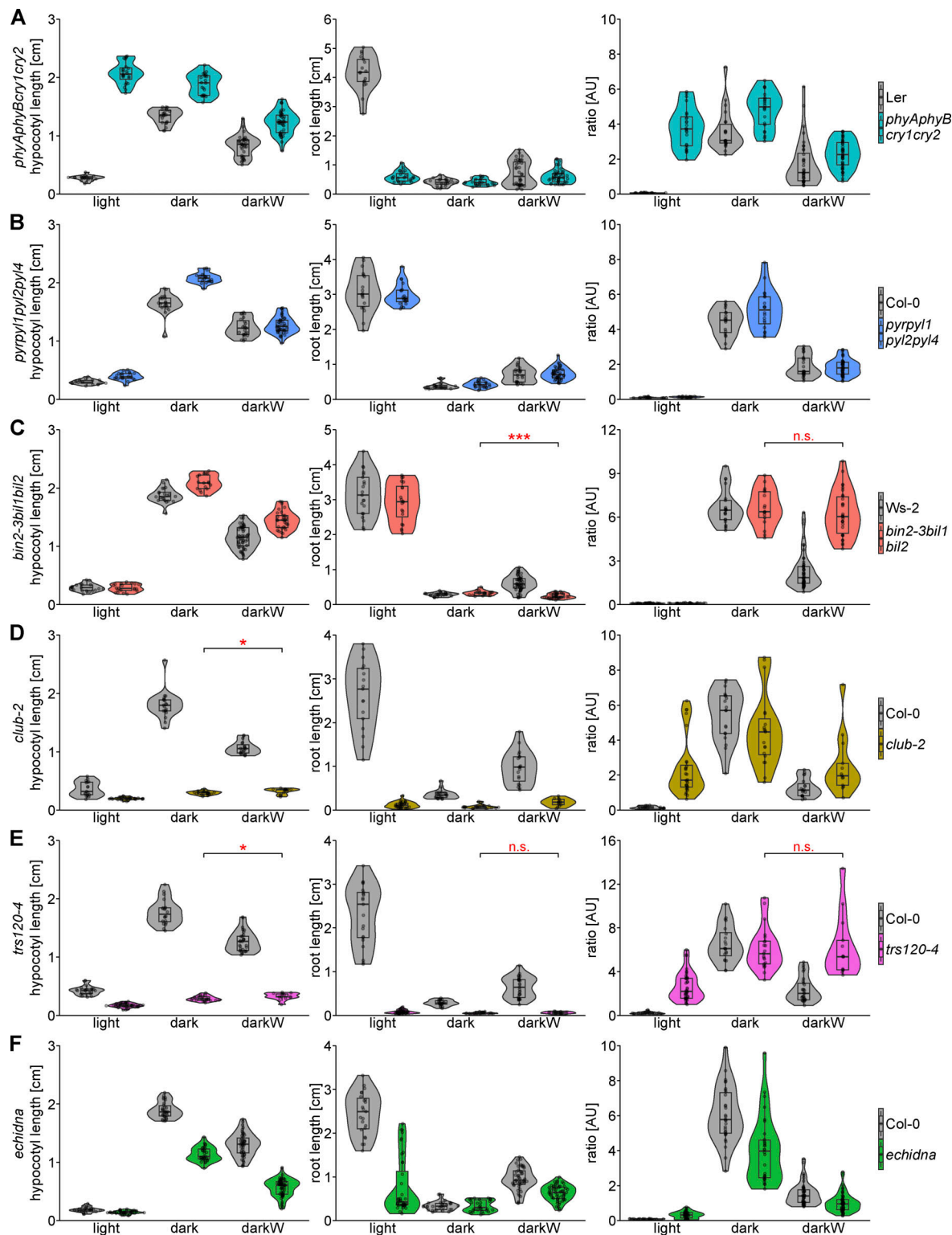
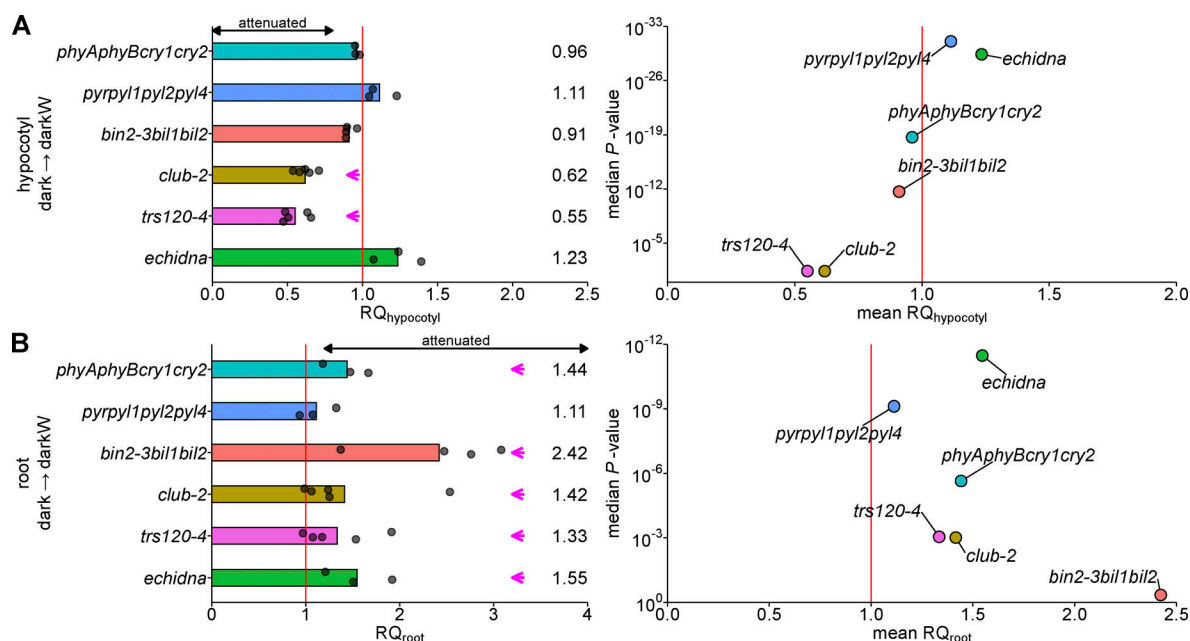
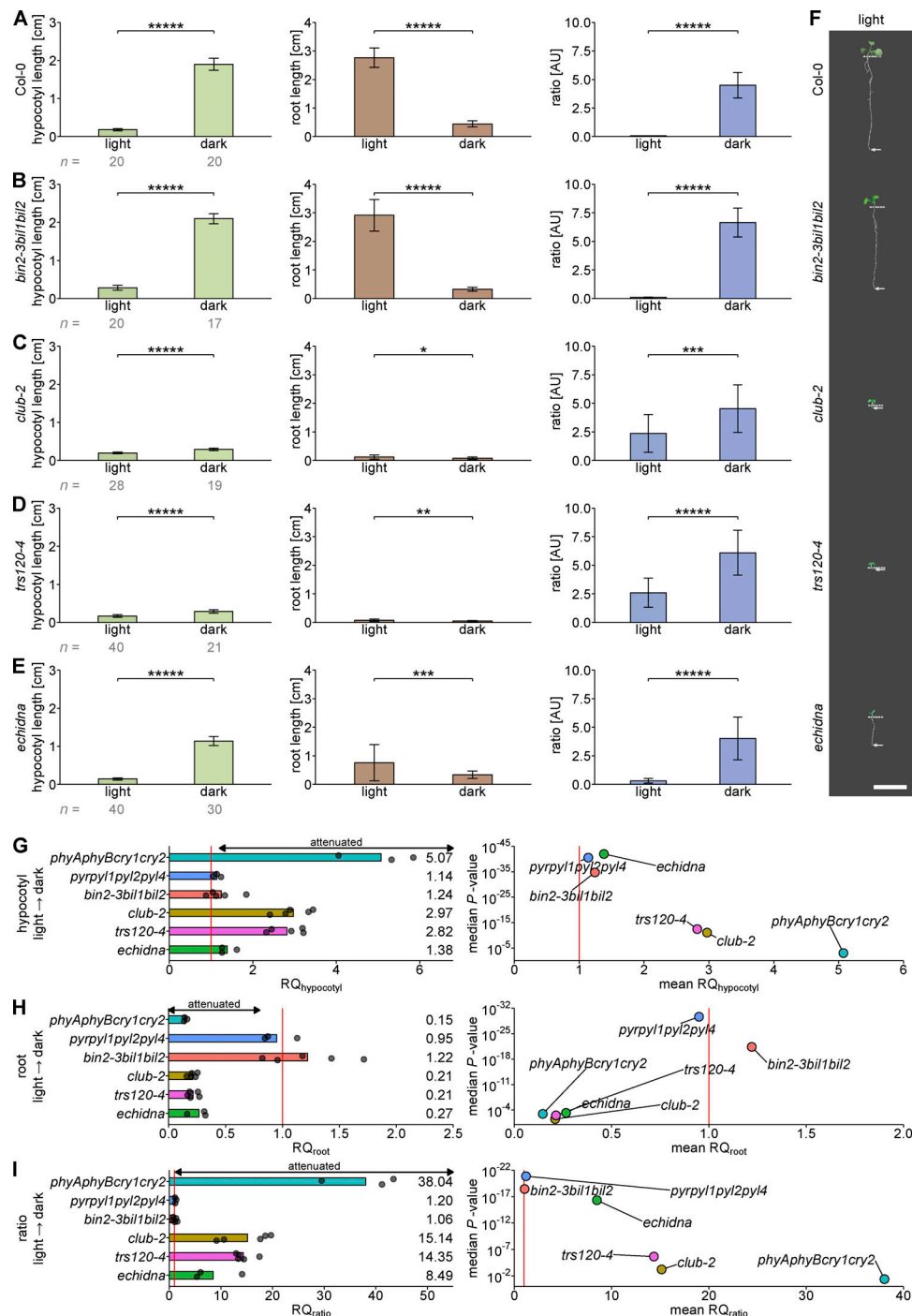


Figure S7. **Response to single versus additive stress: violin plots.** Seedlings were germinated on  $\frac{1}{2}$  MS in the light (light), in the dark (dark), or in the dark with  $-0.4$  MPa water stress (darkW). **(A–F)** Violin plots depict a direct comparison of organ lengths or the hypocotyl/root ratio between the wild type and (A) *phyAphyBcry1cry2*; (B) *pyrp1pyl2pyl4*; (C) *bin2-3bil1bil2*; (D) *club-2*; (E) *trs120-4*; (F) *echidna* in the same experiment and on the same PEG plates. The same datasets as shown in Fig. 5, B–E and Fig. S9, B–E were used. Decision phenotypes of *bin2-3bil1bil2* and *trs120-4* mutants are highlighted as follows: *bin2-3bil1bil2* showed an opposite root adaptation (red asterisks) and no hypocotyl/root adaptation (non-significant [n.s.] in red) to the multiple stress conditions of darkW. *trappii* null mutants, *club-2* and *trs120-4*, had an attenuated, but significant etiolation response but failed to correctly adjust their hypocotyl length under darkW (red asterisks). Additionally, *trs120-4* mutants showed no root and no hypocotyl/root ratio adaptation (n.s. in red) to darkW conditions. At least three experiments were performed for each line, and a representative one is shown here on the basis of RQ and P values. P values for decision phenotypes were computed with a two-tailed Student's *t* test (\*:  $P < 0.05$ ; \*\*\*:  $P < 0.001$ ) Related to Figs. 5 and S9.





**Figure S8. Response to additive stress: response quotients and volcano plots for the hypocotyl and root.** Response quotients (RQ, left) and volcano plots (right) of the hypocotyl and root adaptations to dark-to-dark with water stress ( $-0.4$  MPa, darkW). RQ response quotients are normalized to the respective wild-type response; a value of 1 (vertical red line) indicates that the response to a shift from dark to darkW is identical to that of the respective wild-type ecotype. Each replicate is represented by a dot. Mean RQ values are given on the right. Volcano plots show the mean RQ depicted on the X axis and the median P value of the response on the Y axis (negative log scale). **(A)** Hypocotyl responses to dark versus darkW conditions. Note that *club-2* and *trs120-4* had attenuated responses ( $RQ_{\text{hypocotyl}} < 0.8$ , magenta arrows). **(B)** Root responses to dark versus darkW conditions. Note that the triple *bin2-3bil1bil2* knock out (from Kalbfuß et al., 2022) had the strongest attenuated  $RQ_{\text{root}}$  phenotype (mean  $RQ_{\text{root}} = 2.42$ , magenta arrow) with an insignificant root response. *phyAphyBcry1cry2*, *club-2*, *trs120-4*, and *echidna* mutants show also an attenuated root response ( $RQ_{\text{root}} > 1.2$ , magenta arrows). Quadruple *pyrpyl* mutants did not have a phenotype, possibly because only four genes are knocked out in a family with 14 members (Ma et al., 2009; Park et al., 2009). Due to the opposite adaptations of the hypocotyl and root under the additive stress conditions (decrease in hypocotyl and increase in root length from dark-to-darkW), the respective thresholds for attenuated responses are opposite (Fig. S8 A, compared to Fig. S8 B). Related to Fig. 5.



**Figure S9. Light responses in *bin2-3bil1bil2*, *trappii*, and *echidna* mutants.** Seedlings were germinated on ½ MS in the light or dark. **(A)** Col-0 (wild type). **(B)** BR signaling mutant *bin2-3bil1bil2* triple knockout (from Kalbfuß et al., 2022). **(C)** *club-2*, a null *trappii* allele. **(D)** *trs120-4*, a null *trappii* allele. **(E)** Null *echidna* allele, impaired in TGN structure and function. At least three experiments were performed for each line, and a representative one is shown here on the basis of RQ and P values. **(F)** Representative images of light-grown seedlings of Col-0 (wild type) and mutants shown in A–E. Dotted lines mark the hypocotyl-root junction, whereas arrows point to the end of the root. For corresponding dark-grown seedlings see Fig. 5 F. Scale bar is 1 cm. **(G–I)** Response quotients (RQ, left) and volcano plots (right) of (G) the hypocotyl, (H) the root, and (I) the hypocotyl/root ratio responses to light versus dark. RQs are normalized to the wild-type quotient; a value of 1 (vertical red line) indicates that the response to a shift from light to dark is identical to that of the respective wild-type ecotype. Each replicate is represented by a dot. Volcano plots show the mean RQ depicted on the X axis and the P value of the response on the Y axis (negative log scale; a median of all replicates was used). *trappii* mutants *trs120-4* and *club-2*, the TGN mutant *echidna* and the higher order light perception null mutant *phyA-phyBcr1cry2* show a severely attenuated etiolation response (mean RQ<sub>hypocotyl</sub> and mean RQ<sub>ratio</sub> >> 1.2 as well as RQ<sub>root</sub> << 0.8). Note that due to the opposite adaptations of the hypocotyl and root from light-to-dark conditions (increase in hypocotyl, decrease in root length and therefore increased hypocotyl/root ratio), the respective thresholds for attenuated responses are opposite (Fig. S9, G and I, compared with Fig. S9 H). The number (n) of seedlings measured per condition is in gray below the mean ± SD bar graphs. P values were computed with a two-tailed Student's *t* test (\*: *P* < 0.05; \*\*: *P* < 0.01; \*\*\*: *P* < 0.001; \*\*\*\*: *P* < 0.0001; \*\*\*\*\*: *P* < 0.00001). Ecotypes are described in Table S2. All data points for A–E are shown in Fig. S7. Related to Fig. 5.

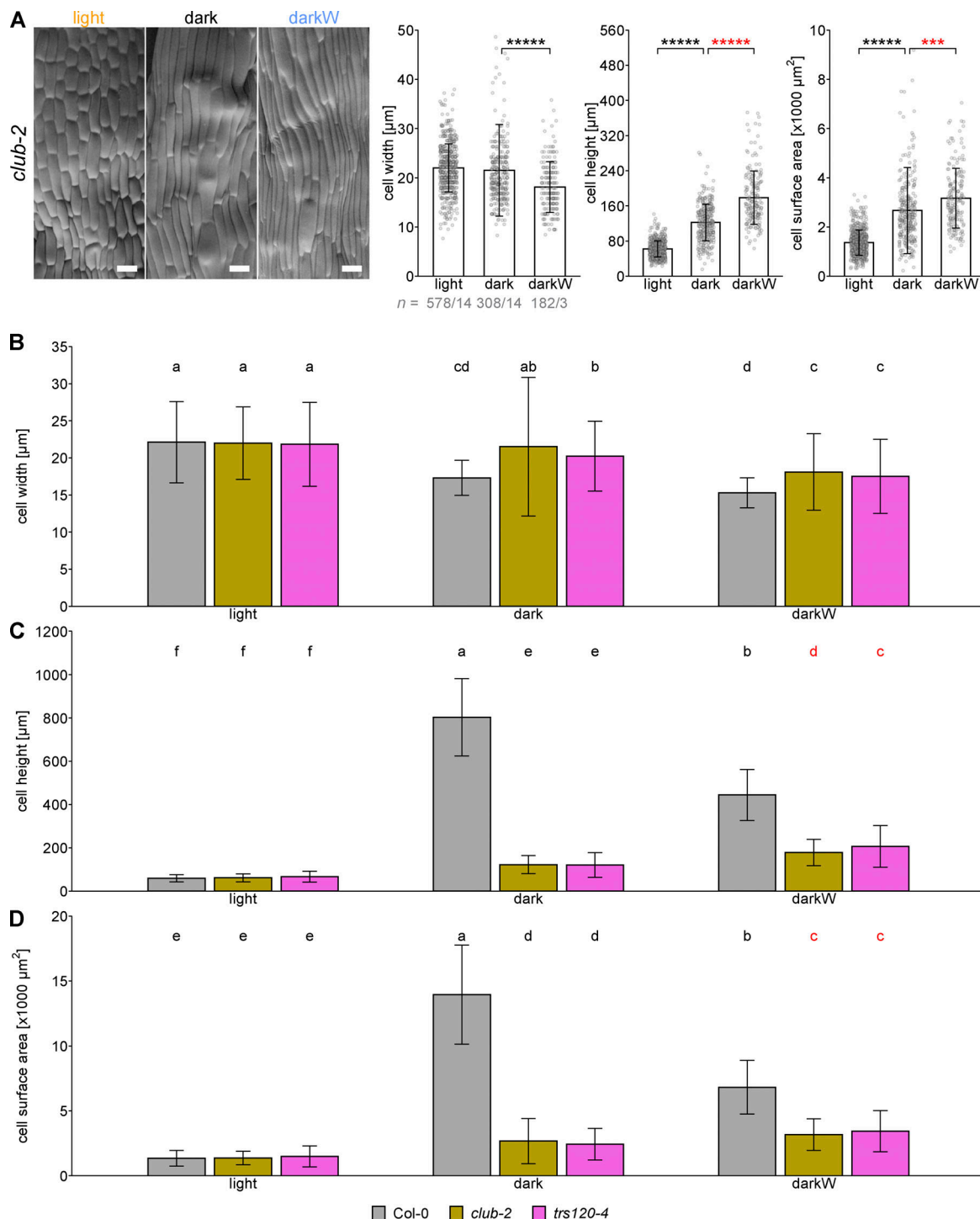


Figure S10. **Cellular hypocotyl parameters of *trappii* mutants under single and additive stress conditions.** Seedlings were grown in the light (orange), dark (black), or dark with  $-0.4$  MPa water stress (darkW; blue). **(A)** Scanning electron micrographs (SEM) of hypocotyls of *club-2* mutants. The cell surface area was calculated as the product of cell width and length. *club-2* mutants showed, identical to *trs120-4* (Fig. 6 B), the opposite hypocotyl cell height and cell surface area adaptations to dark-to-darkW conditions (red asterisks) than the wild-type control (Fig. 6 A). Representative SEM images of seedlings grown under the specified conditions are shown (scale bar =  $40 \mu\text{m}$ ). The sample size ( $n$ ) is given as the number of cells/number of seedlings that were analyzed in gray below the graph. Shown are means  $\pm$  SD. P values were computed with a two-tailed Student's  $t$  test and are represented as follows: \*\*\*:  $P < 0.001$ ; \*\*\*\*\*:  $P < 0.00001$ . **(B–D)** Bar plots for a direct comparison of the hypocotyl (B) cell width, (C) cell height, and (D) cell surface area of *trappii* mutants and the wild-type control (Col-0) shown in Fig. 6, A and B; and Fig. S10 A. The cellular hypocotyl parameters in the light did not significantly differ between *trappii* mutants and the wild type. *club-2* and *trs120-4* showed a compromised, but significant adjustment of the cellular parameters under single stress conditions (light to dark). Only under multiple stress (dark to darkW), *trappii* mutants failed to correctly adjust their cellular hypocotyl parameters with the opposite adjustment of the cell height and surface area compared with the wild type (red letters). Shown are means  $\pm$  SD. Letters indicate statistical significance in two-way ANOVA with Tukey's post hoc test. Related to Fig. 6.

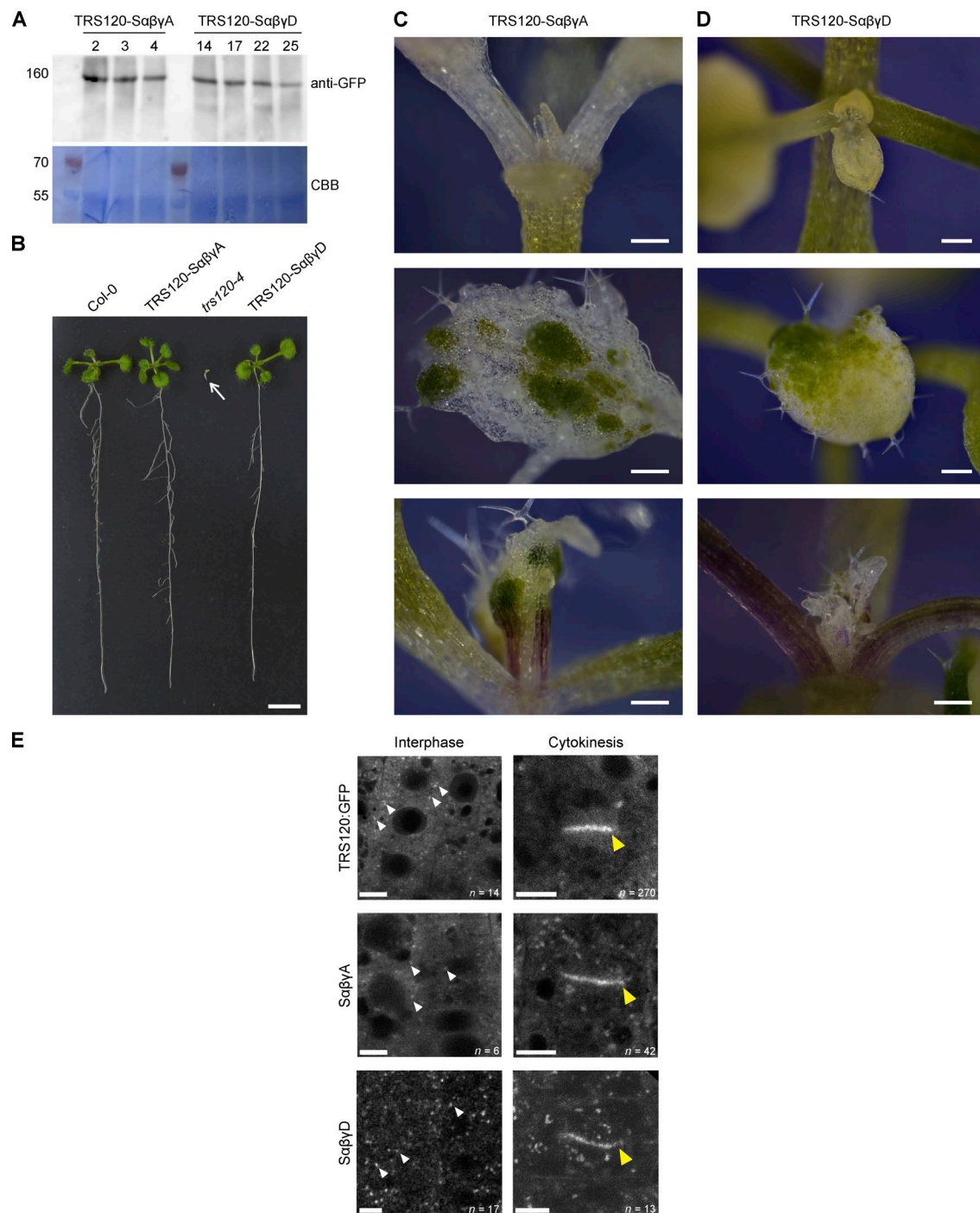


Figure S11. **Characterization and localization of TRS120:GFP phosphovariants.** (A) Western blot depicting protein expression of the phosphovariants TRS120-SaβγA and TRS120-SaβγD in *trs120-4/trs120-4*. Presence of the GFP-fused phosphovariants was detected with an anti-GFP antibody (upper panel). Shown are the expression levels in different primary transformants for each variant. Loaded protein amounts are shown by the corresponding CBB staining (Coomassie stain, lower panel). Protein sizes are given in kDa on the left. (B) Complementation analysis. The TRS120-SaβγA and TRS120-SaβγD phosphovariants in *trs120-4/trs120-4* could rescue the null *trs120-4* seedling lethal phenotype (third seedling from the left; white arrow) and did not differ from the wild-type Col-0 control in the T1 and T2 generations. Kanamycin selection was used to select for the presence of the phosphovariant construct. Images taken 13 days after stratification. Scale bar is 1 cm. (C and D) Silencing of the phosphovariant constructs upon propagation beyond the T2 generation. 2-week-old seedlings were imaged using a camera-equipped binocular microscope. (C) TRS120-SaβγA and (D) TRS120-SaβγD seedlings grown on kanamycin had some white sectors due to loss of chlorophyll in the shoot apical meristem and first true leaves; this was presumably due to gene silencing. Scale bars represent 200 μm. (E) Localization patterns of TRS120:GFP phosphovariants in root tip cells of light-grown seedlings. Confocal Scanning Laser Microscopy. P<sub>TRS120::</sub>TRS120:GFP (Rybak et al., 2014) and phosphovariants thereof. Scale bars represent 5 μm. Wild-type TRS120 resides in the cytosol and at the TGN, it labels endomembrane compartments (white arrowheads) and the cell plate (yellow arrowhead); the phosphovariants have a similar appearance. Sample numbers *n* = interphase or cytokinetic cells imaged. 44 TRS120-WT, 13 -SaβγA, and 10 -SaβγD root tips were imaged. Source data are available for this figure: SourceData FS11.



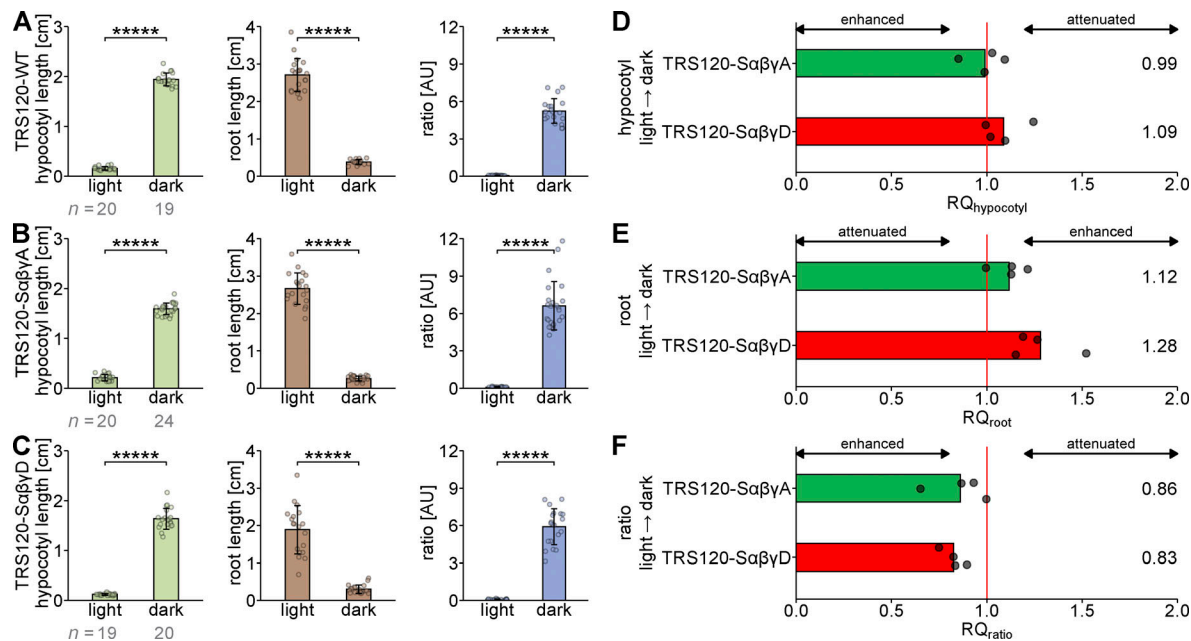


Figure S12. **The etiolation response in TRS120 phosphovariants.** (A) TRS120-WT ( $P_{\text{TRS120}}::\text{TRS120:GFP}$  in *trs120-4/trs120-4*) (Rybak et al., 2014). (B) The non-phosphorylatable TRS120 mutant TRS120-SaβγA in *trs120-4/trs120-4*. (C) The phosphomimetic TRS120 mutant TRS120-SaβγD in *trs120-4/trs120-4*. Seedlings were grown on ½ MS media under light and dark conditions. All mutants showed a significant adaptation to light versus dark conditions, i.e., increased hypocotyl growth and reduced root growth leading to a higher hypocotyl/root ratio under dark conditions. For each mutant, four biological replicates were analyzed, and the representative line based on the RQ and P values is depicted here. Values are means ± SD of measured seedlings per condition, number (n) of seedlings are given in gray below the graphs. Stars indicate statistical significance with a two-tailed Student's t test (\*\*\*\*:  $P < 0.00001$ ). (D–F) Response quotients (RQ) of (D) the hypocotyl, (E) the root, and (F) the hypocotyl/root ratio of the non-phosphorylatable TRS120-SaβγA and the phosphomimetic TRS120-SaβγD mutants for light-to-dark adaptation. RQ response quotients are normalized to the TRS120-WT control,  $P_{\text{TRS120}}::\text{TRS120:GFP}$  in *trs120-4/trs120-4*. A value of 1 (vertical red line) corresponds to an identical adaptation to dark conditions as the control. TRS120-SaβγA and TRS120-SaβγD phosphovariants did not measurably differ from the control (TRS120-WT) line, with RQ values close to 1 (TRS120-SaβγA: mean  $RQ_{\text{ratio}} = 0.86$ ; TRS120-SaβγD: mean  $RQ_{\text{ratio}} = 0.83$ ). Note that due to the opposite adaptations of the hypocotyl and root from light-to-dark conditions (increase in hypocotyl, decrease in root length and therefore increased hypocotyl/root ratio), the respective thresholds for attenuated and enhanced responses are opposite. Dots represent biological replicates, mean RQ values are given on the right. Related to Fig. 7.

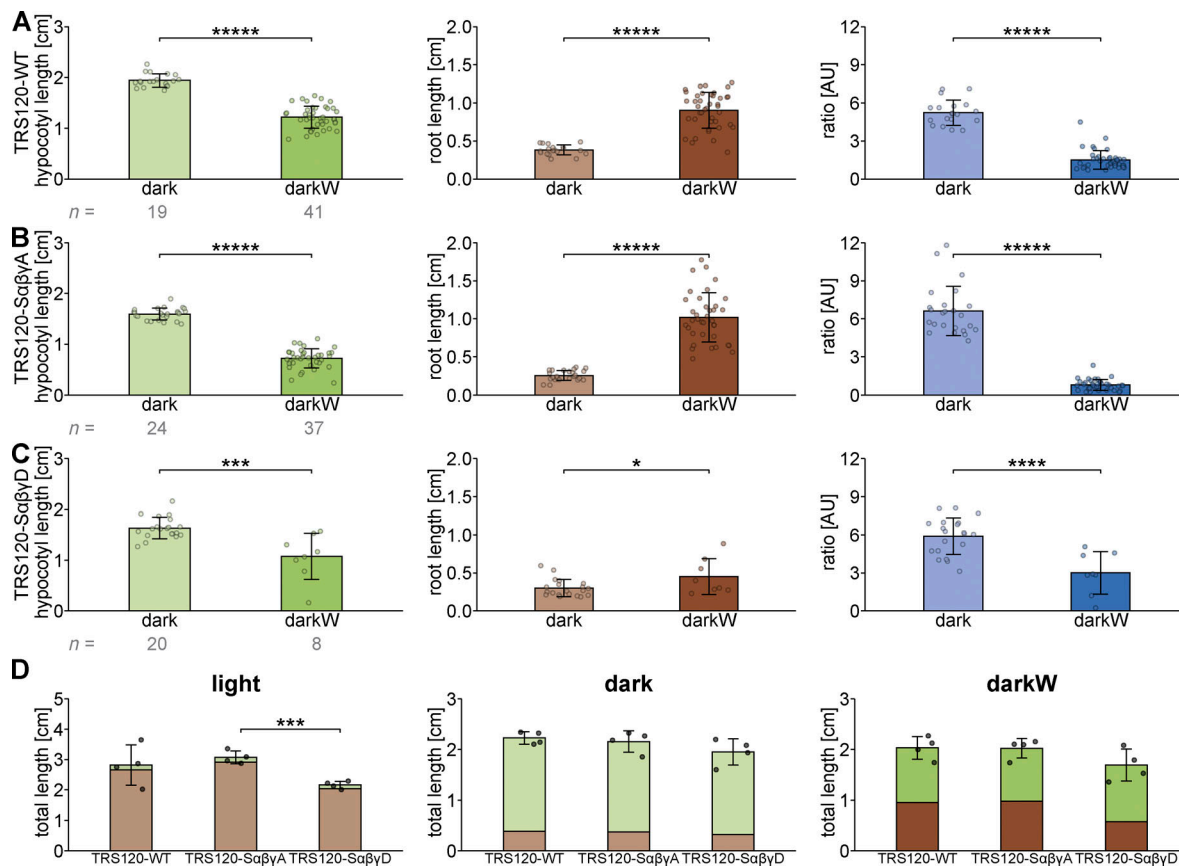


Figure S13. **Role of TRS120 phosphorylation status on adaptive growth responses under additive stress conditions.** (A) TRS120-WT ( $P_{\text{TRS120}}::\text{TRS120}::\text{GFP}$  in *trs120-4/trs120-4*) (Rybak et al., 2014). (B) The non-phosphorylatable TRS120-SaβγA in *trs120-4/trs120-4*. (C) The phosphomimetic TRS120-SaβγD in *trs120-4/trs120-4*. TRS120-SaβγD mutants had attenuated root and ratio responses under darkW, whereas TRS120-SaβγA mutants showed a slightly enhanced root response. (D) Total seedling lengths of TRS120-WT, TRS120-SaβγA, and TRS120-SaβγD. The hypocotyl length is depicted in green and the root in beige-brown shades with an increasing opacity gradient for the different conditions. The total seedling length did not vary from the TRS120-WT control, highlighting the adaptation defect of TRS120-SaβγD to darkW. Seedlings were grown on ½ MS media under light, dark and dark with -0.4 MPa water stress (darkW) conditions. For each line, four biological replicates were analyzed. Values are means ± SD of measured seedlings per condition, number (n) of seedlings are given in gray below the graphs. A representative line, based on the RQ and P values, is depicted for A–C. For total seedling lengths, means ± SD of four biological replicates are shown. Stars indicate statistical significance with a two-tailed Student's *t* test (\*: *P* < 0.05; \*\*: *P* < 0.01; \*\*\*: *P* < 0.001; \*\*\*\*: *P* < 0.0001; \*\*\*\*\*: *P* < 0.00001). Related to Fig. 7.

Video 1. **Cross-kingdom structural alignment of the TRAPP-II-specific TRS120 subunit.** AlphaFold prediction (Jumper et al., 2021; Varadi et al., 2022) of *Arabidopsis thaliana* (At) AtTRS120/TRAPPC9 aligned with the open formation of the TRAPP-II monomer structure without substrate in *Saccharomyces cerevisiae* (Sc) resolved with cryo-electron microscopy (in vitro) from Mi et al. (2022). Alignment was performed with the align algorithm in PyMOL. Reported root-mean-square deviation (RMSD) was 16.966 Å (3,775 atoms). The ScTRAPP-II monomer is depicted in different shades of gray, and only the ScTRS120 subunit on which AtTRS120 was mapped in the alignment is highlighted in blue-white. AtTRS120 is colored based on its sequence conservation (red: conserved sequences; orange: intermediate conservation; green: plant-specific sequences - as depicted in Fig. 2, A and D; and Fig. 3). Note that the β and γ phosphorylation sites of AtTRS120 (magenta sticks) face inward, toward the active site chamber (including the RAB11/Rab-A GTPase binding pocket) proposed by Mi et al. (2022) and Bagde and Fromme (2022). Image display rate: 30 frames/s. Related to Figs. 2, 3, and S4.

Provided online are Table S1, Table S2, Table S3, Table S4, and Table S5. Table S1 shows selected brassinosteroid signaling proteins in the CLUB interactome. Table S2 shows the mutant lines used in this study. Table S3 lists sites mutated in TRS120 phosphovariants and corresponding primer sequences used for mutagenesis. Table S4 shows the gene strand sequence carrying the TRS120 amiRNA precursor. Table S5 shows the thresholds for attenuated, normal, and enhanced response quotients.